

Institut für Theoretische Physik  
Fakultät Mathematik und Naturwissenschaften  
Technische Universität Dresden

# Morphogenetic signaling in growing tissues

**Dissertation**

Zur Erlangung des akademischen Grades

Doctor rerum naturalium  
(Dr. rer. nat.)

vorgelegt von

**Thomas Bittig**

geboren am 29.5.1979 in Neustadt an der Weinstraße

Max-Planck-Institut für  
Physik komplexer Systeme

Dresden, 2008



# Acknowledgements

Foremost, I would like to thank Prof. Dr. Frank Jülicher for his supervision of my work. In countless discussions, he helped me to develop the key ideas and thus the backbone for this thesis.

Furthermore, I thank Prof. Dr. Marcos González-Gaitán and his students Ani Kicheva, Veronica Dudu, Ortrud Wartlick and Periklis Pantazis for the numerous inspiring meetings during the last three years. The discussions with them and their experimental results were a constant source of motivation for my theoretical studies in this work.

I would also like to thank all the members of our group, who did not only help me with the innumerable little questions that have occurred in the course of this project, but who also made life enjoyable at our institute. In particular, I would like to thank Nadine Baldes for her efforts and successes in keeping the group's spirit high.

Finally, I would like to thank Kai Müller and Ani Kicheva for proofreading this thesis.



# Abstract

During the development of multicellular organisms, organs grow to well-defined shapes and sizes. The proper size and patterning of tissues are ensured by signaling molecules as e.g. morphogens. Secreted from a restricted source, morphogens spread into the adjacent target tissue where they form a graded concentration profile. Upon binding of the morphogens to receptors on the cell surfaces, the morphogenetic signal is transduced inside the cell via the phosphorylation of transcription factors, which subsequently regulate the expression of different target genes. Thus, cell fates are determined by the local concentration of such morphogens.

In this work, we investigate three key aspects of morphogenetic signaling processes in growing tissues. First, we study the mechanics of tissue growth via cell division and cell death. We examine the rearrangements of cells on large scales and times by developing a continuum theory which describes the growing tissue as an active complex fluid. In our description we include anisotropic stresses generated by oriented cell division, and we show that average cellular trajectories exhibit anisotropic scaling behaviors. Our description is used to study experimentally measured shape changes of the developing wing disk of the fruit fly *Drosophila melanogaster*.

Second, we focus on the spreading of morphogens in growing tissues. We show that the flow field of cell movements due to oriented cell division and cell death causes a drift term in the morphogen transport equation, which captures the stretching and dilution of the concentration profile. Comparing our theoretical results to recent experiments in the *Drosophila* wing disk, we find that the transport of the morphogen Dpp is mainly intracellular. We moreover show that the decay length of the Dpp gradient increases during development as a result of changing degradation rate and diffusion coefficient, whereas the drift of molecules due to growth is negligible. Thus growth does not affect the decay length of the gradient, but the decay length of the gradient might affect the tissue growth rate as discussed in this work.

Finally, we develop a microscopic theoretical description of the intracellular transduction machinery of morphogenetic signals within an individual cell. Our description captures the kinetics of the trafficking of proteins between different cellular compartments in response to receptor-bound signaling molecules. Analyzing experimental data at the *Drosophila* neuromuscular junction, we show that the morphogenetic signaling is modulated by synaptic signaling via neuronal action potentials.



# Contents

<b>1</b>	<b>Introduction</b>	<b>9</b>
1.1	Quantitative approaches to developmental pattern formation . . . . .	9
1.2	Growth of cellular tissues during development . . . . .	13
1.3	Overview of this work . . . . .	15
<b>2</b>	<b>Dynamics of anisotropic tissue growth</b>	<b>17</b>
2.1	Continuum description . . . . .	17
2.1.1	Balances of cell number and forces . . . . .	18
2.1.2	Constitutive relation for anisotropic tissue growth . . . . .	18
2.1.3	Growth of incompressible tissues . . . . .	19
2.2	Discrete model . . . . .	20
2.2.1	Dynamic equations . . . . .	21
2.2.2	Oriented cell division and apoptosis . . . . .	22
2.2.3	Results of numerical simulations . . . . .	23
2.3	Shape changes of growing epithelia . . . . .	26
<b>3</b>	<b>Morphogen gradients in growing tissues</b>	<b>31</b>
3.1	Dpp spreading in the Drosophila wing disk . . . . .	32
3.1.1	Concentration profile in steady state . . . . .	32
3.1.2	FRAP experiments: measuring the kinetic parameters . . . . .	33
3.1.3	Dpp transport dominated by intracellular trafficking . . . . .	36
3.2	Dpp transport in the growing wing disk . . . . .	38
3.2.1	Transport equation . . . . .	38
3.2.2	Steady-state gradient in the growing disk . . . . .	40
3.2.3	Impacts of growth on the Dpp gradient . . . . .	40
3.3	The Dpp gradient during development . . . . .	42
3.3.1	Kinetic parameters of Dpp spreading during development . . . . .	42
3.3.2	Evolution of the Dpp concentration profile . . . . .	47
3.3.3	Dpp concentration measured by moving cells . . . . .	48
3.4	Possible roles of Dpp in growth control . . . . .	50

---

<b>4</b>	<b>Kinetics of TGF-<math>\beta</math> signaling in the cell</b>	<b>59</b>
4.1	Theoretical description of Mad intracellular trafficking . . . . .	59
4.2	Kinetic parameters of Mad intracellular trafficking . . . . .	63
4.3	Discussion . . . . .	66
<b>5</b>	<b>Summary and outlook</b>	<b>69</b>
<b>A</b>	<b>Mechanics of tissue growth</b>	<b>75</b>
A.1	Growth of compressible tissues . . . . .	75
A.2	Cell division and apoptosis in the continuum limit of the discrete description	76
A.3	Numerical simulations of tissue growth . . . . .	77
A.4	Relation between cell movements and tissue shapes . . . . .	77
A.5	Shape changes of the developing <i>Drosophila</i> wing disk . . . . .	78
<b>B</b>	<b>The Dpp gradient in the growing wing disk</b>	<b>81</b>
B.1	Coordinate transformation of the Dpp transport equation . . . . .	81
B.2	Steady state of the diffusion equation with drift term . . . . .	82
B.3	The feedback between concentration and growth rate . . . . .	84
B.4	Measurements of P-Mad gradients in the wing disk . . . . .	87
<b>C</b>	<b>Kinetics of cellular signaling</b>	<b>89</b>
C.1	Fit of the microscopic description to the FRAP curves . . . . .	89
C.2	The immobile nuclear Mad pool . . . . .	90
	<b>Bibliography</b>	<b>93</b>



# Chapter 1

## Introduction

The development of multicellular organisms from a single nearly uniform fertilized egg cell is a fascinating process. By repeated rounds of cell divisions, spatial cell packings are formed, mostly in two-dimensional sheets such as epithelia, or in three-dimensional tissues. Besides cell division, cell death (apoptosis) can play an important role during development. As the tissues grow and develop, cells of different type emerge and build such complex structures as our eyes, hands, or brain [99, 88].

### 1.1 Quantitative approaches to developmental pattern formation

Since all cells are descendants of the fertilized egg cell, they all contain the same genetic information stored in their DNA [4]. The symmetry breaking that accounts for the differentiation of cells has raised the interest of theorists for more than fifty years. In the 1950s, Turing suggested that certain molecules, which he called morphogens, diffuse and self-organize into spatial patterns that subsequently structure the organism [94]. In systems of reaction-diffusion equations, he showed that patterns can emerge from initially homogeneous molecule concentrations due to instabilities triggered by statistical fluctuations. Based on Turing's ideas, biological pattern formation resulting from reaction-diffusion systems has been studied extensively [42, 72, 29, 58, 75], and may indeed underlie the pigmentation patterns of spots and stripes found e.g. in cheetah, zebra, or angelfish coats [75, 99].

However, the modern definition of morphogens was coined by Wolpert in 1969 [98]. Produced and secreted from a localized source, morphogens spread into the adjacent target tissue and form a graded concentration profile, called morphogen gradient. Thus, positional information is conveyed to target cells based on their position within the morphogen concentration gradient. Today, a number of proteins have been identified to act as morphogens [48, 91], among which are secreted ligands of the Hedgehog (Hh) [11], Wingless (Wg) [101], and TGF- $\beta$  protein families [69].

Binding to receptors on the cell surfaces, morphogens can induce the activation of

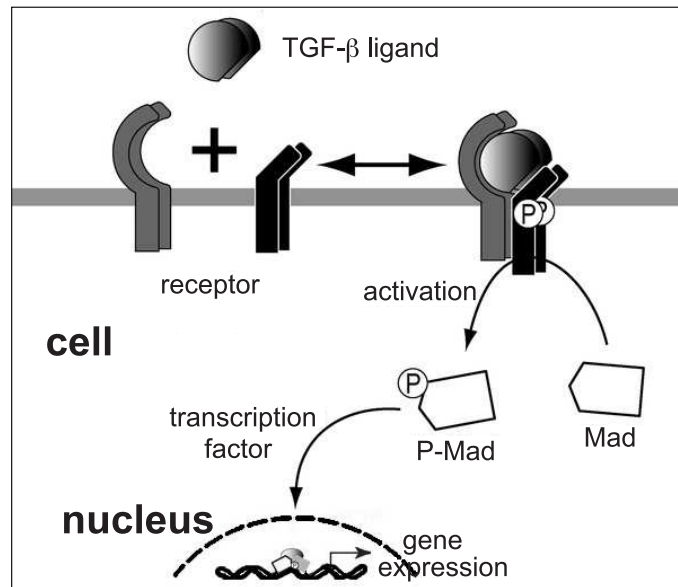


Figure 1.1: Schematic representation of TGF- $\beta$  signaling. TGF- $\beta$  ligands such as the morphogens Dpp or Activin bind to receptors on the cell surface as e.g. the protein Thickveins (Tkv). The activated ligand-receptor complexes induce the phosphorylation of cytosolic Mad, which can then enter the cell nucleus and act there as transcriptional regulators of about 300 target genes. Figure modified from [95].

transcription factors within the cells [69, 86], as e.g. the phosphorylation of the protein Mothers-against-Dpp (Mad) in response to TGF- $\beta$  ligands such as Decapentaplegic (Dpp) or Activin [83, 97, 50, 57], see Fig. 1.1. The activated transcription factors mediate the morphogenetic signal by regulating the transcription of different genes in the cell. Often, these target genes are either strongly expressed or hardly expressed at all, and cells switch between these two states of gene expression at certain threshold values of the morphogen concentration [11, 51, 85]. Hence morphogens control cell fates by regulating the cellular protein production.

The role of TGF- $\beta$  signaling molecules during development has e.g. been studied at the neuromuscular junction of the fruit fly *Drosophila melanogaster* [4, 99]. This connection between a neuron and a muscle cell forms during embryogenesis [21] and grows during larval stages to adjust itself to the growth of the muscle [82]. To match the growth of muscle and synapse during larval development, cell-to-cell communication takes place involving the TGF- $\beta$  signaling pathway [59, 1, 68, 70, 80].

In the past two decades, cellular signal transduction machineries have been broadly investigated as examples of complex networks [96, 13, 95, 5]. It has been shown that signaling systems which contain a feedback between two or more proteins can be bistable [6], which might be relevant for the switching between the different states of gene expression. Another important issue is the robustness of signaling networks [10, 51],

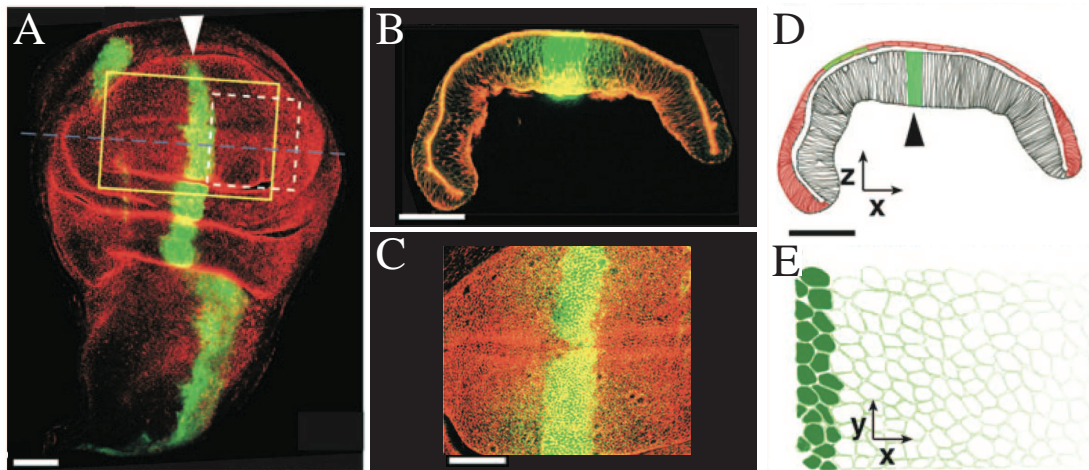


Figure 1.2: The morphogen Dpp in the developing *Drosophila* wing disk. (A) Top view on the wing disk. Cell contours are labeled in red, Dpp in green. The Dpp source is indicated by a arrowhead. (B) Profile view on the wing disk at the level of the dashed blue line in A. The cell contours are labeled in red, superimposed by Dpp (green). (C) Detail of the Dpp localization (green) corresponding to the yellow box in A. Cells labeled in red. (D,E) Schematic of the developing wing in a  $xz$ - (D) and  $xy$ -section (E). Cells filled in green represent cells of the Dpp source (arrowhead in D). Bars correspond to  $50\ \mu\text{m}$ . Anterior to the left, posterior to the right. Figure modified from [60].

because the functionality of a cell should not depend sensitively on parameters that are likely to fluctuate.

Robustness can also be achieved in the formation of the morphogen gradients [34, 35, 47, 20]. The mechanisms by which morphogens are transported in the tissue have been discussed controversially in recent years [45, 64]. One possibility is that morphogens simply diffuse in the extracellular space surrounding the cells [28], which e.g. seems to be the case for the morphogen Activin in the frog *Xenopus* [71]. Alternatively, it has been proposed that morphogens might bind to large molecules on the cell surface and are subsequently transported by passive diffusion in the cell membrane [54, 12]. Furthermore, morphogens could also be transported through cytonemes which are long thin membrane tubes that connect cells in the tissue [78].

However, recent experiments on the morphogen Dpp [90, 39, 100, 65, 74] in the wing imaginal disk of the fruit fly suggest another transport mechanism [36]. Dpp is produced in a specific source region which is a narrow stripe with a width of a few cell diameters located at the center of the wing disk, see Fig. 1.2. The wing disk is an essentially two-dimensional larval structure formed from one layer of cells from which the adult fly wing develops [27, 41]. It is divided into an anterior (A) and a posterior (P) compartment. In the P compartment, the morphogen Hh is produced and spreads into the A compartment, where it forms a short-ranged gradient and induces the production of Dpp [11]. Dpp

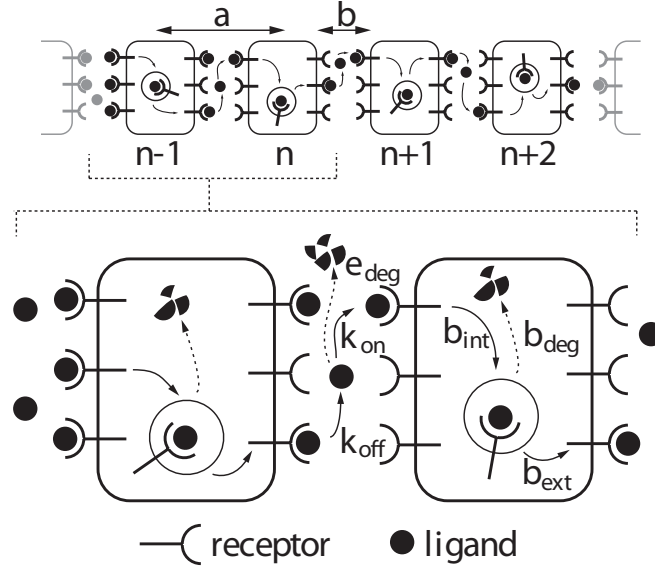


Figure 1.3: Schematic of morphogen transport by transcytosis in a chain of cells of diameter  $a$  indexed by  $n$ . The rates  $k_{\text{on}}$ ,  $k_{\text{off}}$ ,  $b_{\text{int}}$  and  $b_{\text{ext}}$  characterize ligand-receptor binding and unbinding, internalization and externalization. Degradation of ligands in the extracellular space occurs with rate  $e_{\text{deg}}$  and with rate  $b_{\text{deg}}$  inside the cell. Figure modified from [17].

spreads non-directionally into the adjacent target tissue where it is degraded on the time scale of a few hours. Thereby it forms a concentration gradient which extends to more than 30 cell diameters [36]. In experiments, in which the internalization of receptor-bound Dpp molecules into the cells (endocytosis) was blocked, Dpp was only found in the extracellular space about two cell diameters away from the source [36]. These results suggest that Dpp is transported by a process called transcytosis, in which the molecules bind to receptors on the cell surfaces, are internalized into the cells, subsequently recycled and again released from the receptors at a different position on the cell surface [37].

A theoretical description of morphogen transport by transcytosis has been developed in recent years [60, 17, 18, 19]. Due to the symmetry of the disk, a one-dimensional description of morphogen concentration profiles as a function of the distance  $x$  to the source is appropriate [63, 60], see Fig. 1.2. Fig. 1.3 illustrates schematically a simple model to describe transcytosis [17, 18, 19]. Ligands bind and unbind to receptors on the cell surface at rates  $k_{\text{on}}$  and  $k_{\text{off}}$ , respectively. The rates  $b_{\text{int}}$  and  $b_{\text{ext}}$  characterize the internalization and externalization of receptor-bound ligands, respectively. Free ligands in the extracellular space are degraded at rate  $e_{\text{deg}}$ , receptor bound ligands inside the cell are degraded at rate  $b_{\text{deg}}$ . The kinetics of the number of free ligands in the extracellular space and of receptor-bound ligands inside the cell and on the cell surface is described by a system of nonlinear rate equations [17, 18, 19]. From this discrete microscopic model,

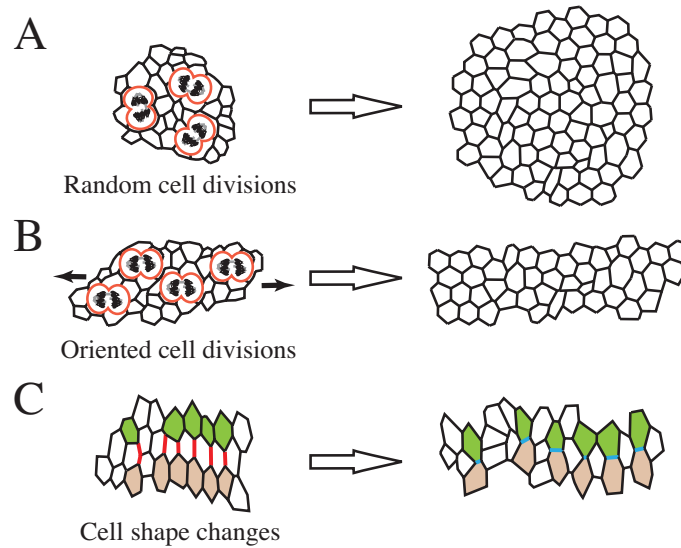


Figure 1.4: Cellular mechanisms to control tissue size and shape. (A) Cell division with random orientation of the division axis maintains the tissue shape and leads to a homogenous increase in tissue size. (B) Cell division with preferred orientation of the cell division axis (here the horizontal axis) leads to anisotropic tissue growth and thus changes in the tissue shape. (C) Cell shape changes can cause convergence and extension of the tissue. Here the red cell bonds shrink and new bonds (blue) are formed, leading to a rearrangement in cell neighbors. Figure modified from [66].

Bollenbach et al. derived an effective continuum description of morphogen transport [17, 18, 19]. Using a separation of time scales between processes on the cell and tissue level, rapid variables in the system can be adiabatically eliminated. In the continuum limit, an effective nonlinear diffusion equation for morphogen transport has been derived. The diffusion coefficient and degradation rate, which characterize morphogen transport on the macroscopic scale, are functions of the morphogen concentration and depend on the microscopic rates of the discrete model, see Fig. 1.3.

## 1.2 Growth of cellular tissues during development

Another important developmental process in addition to pattern formation is the coordination of tissue size and shape. The building blocks of this process are cell division, apoptosis, cell shape changes and cell rearrangements [66], see Fig. 1.4.

Developing tissues can be considered as soft materials with visco-elastic properties [40]. Since active processes take place in cells, such as the cytoskeleton dynamics and cell division, developing tissues can be described as active complex fluids. The generic physical properties of such active fluids have recently been discussed in the hydrodynamic

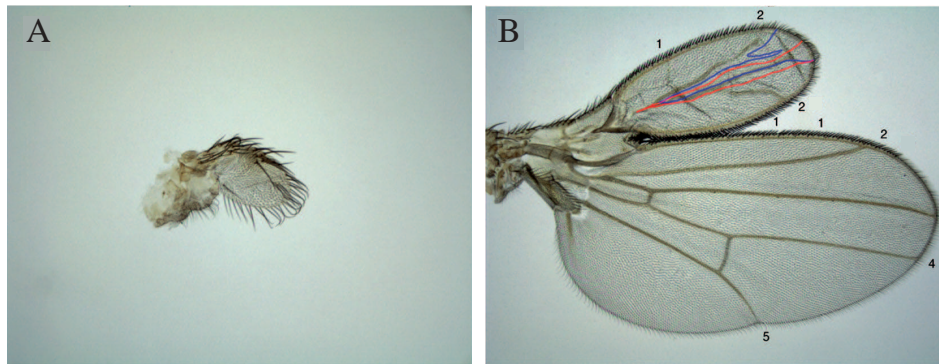


Figure 1.5: The role of the morphogen Dpp in the regulation of tissue growth in the *Drosophila* wing. (A) Wing stump as a result of loss of Dpp production. (B) Wing outgrowth induced by extra Dpp expression in a clone in the receiving tissue. The outgrowth exceeds the clone by far, which is marked by blue and red lines. A is shown at  $1.5\times$  the magnification in B. Figure modified from [100].

limit by continuum descriptions [49, 61]. The most striking feature of a developing tissue that results from active processes is growth. Cells undergo a cell cycle during which they double in size and then divide into two daughter cells. Cell division thus involves forces and mechanical work performed to move the neighboring cells in order to create space for newly produced daughter cells [23, 67, 87, 32]. In addition, apoptosis leads to the removal of cells, and the liberated space is then occupied by neighboring cells. As a consequence of cell division and apoptosis, cells move relative to each other so that cellular packings are remodeled and cells change their nearest neighbors [43].

Important model systems for the study of tissue growth and shape changes during development are the imaginal disks of the fruit fly, such as the wing disk (see Fig. 1.2). It has been observed that cell division in these essentially two-dimensional larval structures is oriented [9]. This implies that the cell division axis has a preferred orientation and can be characterized by an angular distribution [9, 93]. An important open question is the role of oriented cell division for shape changes of a growing tissue.

Another open question is how morphogen transport is modified by tissue growth, and how growth is regulated. What controls the cell division rate and, when the proper size is reached, what tells the tissue to stop growing? Experiments with the fruit fly have shown that the morphogen Dpp is involved in the regulation of growth of the wing disk. If Dpp production is suppressed in the disk, the wing does not grow but forms a little stump, see Fig. 1.5, A. If extra Dpp is produced in a clone within the receiving tissue of the wing disk, an outgrowth of an ectopic wing can be observed as shown in Fig. 1.5, B [100]. Moreover, it has been shown that the growth rate is approximately homogenous in space within the wing disk [44, 73]. It remains a demanding challenge to answer the question how the graded concentration profile of a morphogen as Dpp can account for uniform tissue growth [84, 30, 66, 3].

### 1.3 Overview of this work

This work is a mainly theoretical investigation of morphogenetic signaling processes in growing tissues. We study these developmental processes on three different levels of detail. First, we discuss cell rearrangements in a growing tissue, second we consider the spreading of morphogens through the rearranging cells of the tissue, and third we study the signaling cascade triggered by the morphogenetic signal within an individual cell.

In chapter 2, we consider the mechanics of anisotropic tissue growth that results from oriented cell division (see Fig. 1.4, B) and apoptosis. We develop a continuum theory which describes the tissue as an effective viscous material with active stresses generated by cell division. We study the effects of anisotropies of cell division on cell rearrangements and show that average cell trajectories exhibit anisotropic scaling behaviors. We discuss the resulting shape changes of a growing epithelium and compare our theoretical results to measured shape changes of the developing wing disk of the fruit fly. We show that the disk grows anisotropically, and that the strength of the anisotropy depends on the level of Dpp expression.

In chapter 3, we investigate morphogen spreading in growing tissues. Based on the theoretical description of morphogen spreading via transcytosis by Bollenbach et al. [17, 18, 19], we show that tissue growth leads to an additional drift term in the effective diffusion equation that describes morphogen transport. This drift term captures the stretching and dilution of the morphogen gradient that results from growth. Our theoretical studies are applied to experimental data on the Dpp gradient in the growing *Drosophila* wing disk. We show that Dpp transport is mainly intracellular in agreement with transcytosis whereas extracellular diffusion is inconsistent with our results. The kinetic parameters of Dpp spreading are measured during wing disk development. We show that the growth effects of dilution and stretching are negligibly small throughout development, i.e. growth does not change the decay length of the Dpp gradient. Finally, we discuss possible rules how Dpp could regulate the growth of the wing disk. We show that the relative rate of change of the cellular P-Mad concentration, which mediates Dpp signaling (see Fig. 1.1), is independent on position and shows a unique relation to the growth rate. Therefore, we can define a possible rule how P-Mad might control the uniform growth rate and trigger the stop of wing disk growth.

Eventually, chapter 4 deals with the intracellular transduction machinery of TGF- $\beta$  signaling on the single cell level. In a microscopic model, we describe the kinetics of intracellular Mad trafficking in response to the receptor-mediated TGF- $\beta$  signal with a system of coupled ordinary differential equations. We compare our theoretical description to experimental data on developmental signaling events at the *Drosophila* neuromuscular junction. We determine several rate constants of intracellular signaling and show that developmental signaling via TGF- $\beta$  ligands is modulated by neuronal signaling via synaptic activity.





## Chapter 2

# Dynamics of anisotropic tissue growth

In this chapter, we present a coarse-grained physical description of cell movements in growing tissues which takes into account the physical properties of cells in the tissue, in particular tissue viscosity [14]. As a novelty compared to existing approaches [23, 67, 87, 32], we include anisotropic stresses in our description caused by oriented cell division. We first develop a continuum theory in which the growing tissue is described as a viscous fluid medium (see section 2.1). With our description, we study the flow profiles of cell movements that result from oriented cell division and apoptosis in two-dimensional epithelia, which provide the basis for our description of morphogen gradients in growing tissues (see chapter 3).

We furthermore perform numerical simulations of a discrete model in which individual cells are described as elastic objects that can slide relative to each other subject to friction forces (see section 2.2). In our discrete fluid model, fluctuations resulting from cell division and apoptosis are taken into account. We use the numerical results for the discrete cellular system to test the applicability of our continuum description.

On the basis of our continuum theory, we finally study shape changes of epithelia that result from oriented cell division and apoptosis (see section 2.3). We compare our theoretical results with recent experiments in which the shape of the *Drosophila* wing disk was measured at different stages during development. We show that the growth of the *Drosophila* wing disk is indeed anisotropic, and we find that the strength of the anisotropy of growth depends on the level of Dpp expression.

### 2.1 Continuum description

Our continuum theory of anisotropic tissue growth is based on balances of cell number and forces and extends earlier approaches [23, 67] by taking anisotropic stresses into account. This description allows us to study the flow profiles of cell rearrangements in growing tissues in which cell division is oriented.

### 2.1.1 Balances of cell number and forces

We introduce the cell density  $\rho(\mathbf{r}, t)$  at position  $\mathbf{r}$  and time  $t$  as the number of cells per area (volume) in  $d = 2$  ( $d = 3$ ) dimensions within an area (volume) element. These elements are large compared to the size of a single cell but small compared to the size of the tissue. The velocity  $\mathbf{v}(\mathbf{r}, t)$  is defined as the averaged velocity of cells situated in the corresponding area (volume) element at  $\mathbf{r}$ . In a growing tissue, cell number balance is given by

$$\partial_t \rho + \partial_k(\rho v_k) = (k_g - k_a)\rho. \quad (2.1)$$

Here  $k_g$  and  $k_a$  are the growth and apoptosis rates which account for cell division and cell death, respectively. In general, both rates can depend on space and time.

Momentum conservation involves the rate of change of momentum density, the divergence of the momentum flux density tensor and external bulk forces representing momentum sources and sinks [62]. For our system, inertial forces are small as compared to other forces and are neglected. We decompose the momentum flux density tensor in the stress tensor  $\sigma_{ik}$  and the isotropic pressure  $P$ , which depends on cell density according to  $P(\mathbf{r}, t) = \chi(\rho(\mathbf{r}, t) - \rho_p)/\rho_p$ , where  $\chi$  is the bulk elastic modulus and  $\rho_p$  a reference cell density. Force balance in the tissue is thus given by

$$\partial_k(\sigma_{ik} - P\delta_{ik}) + f_i^{\text{ext}} = 0, \quad (2.2)$$

where  $f_i^{\text{ext}}$  is an external force density.

### 2.1.2 Constitutive relation for anisotropic tissue growth

The stress tensor is related to the flow velocity of cells by a constitutive material relation. We ignore inertial forces and focus on the long time limit when the tissue behaves as a viscous fluid. In addition, we take into account the anisotropic active stresses which are on average generated by oriented cell division. The stress tensor can be written as

$$\sigma_{ik} = \eta \left( \partial_i v_k + \partial_k v_i - \frac{2}{d} \delta_{ik} \partial_l v_l \right) + \zeta \delta_{ik} \partial_l v_l - \mu k_g \left( p_i p_k - \frac{1}{d} \delta_{ik} \right). \quad (2.3)$$

Here  $\eta$  and  $\zeta$  are the shear and bulk viscosity, respectively. The vector  $\mathbf{p}$  is a unit vector which describes the preferred axis of cell divisions, see Fig. 2.1. Hence  $\sigma_{ik}$  is invariant with respect to  $\mathbf{p} \rightarrow -\mathbf{p}$ . The anisotropic stress results from oriented cell division. Therefore, we assume this stress to be proportional to the growth rate  $k_g$ . The strength of the anisotropic stress is characterized by the coefficient  $\mu \geq 0$  which has units of viscosity. The special case  $\mu = 0$  describes isotropic cell divisions. Considering a constant external pressure  $P_{\text{ext}}$ , we furthermore impose the boundary conditions,

$$\sigma_{nn} = P - P_{\text{ext}} \quad \text{and} \quad \sigma_{nt} = 0, \quad (2.4)$$

where the indices  $n$  and  $t$  denote the components of the stress tensor normal and tangential to the tissue boundary, respectively. The Eqs. (2.1)-(2.4) describe the full dynamics of growing tissues.

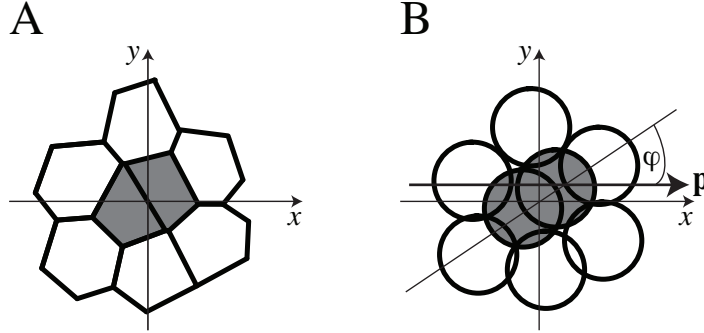


Figure 2.1: Cellular arrangement in the  $xy$ -plane presented as a Voronoi diagram [7] (A) and by circular disks (B). The vector  $\mathbf{p}$  (here  $\mathbf{p} = \mathbf{e}_x$ ) defines the preferred orientation of cell division. The angle  $\varphi$  describes the orientation of the cell division axis with respect to the preferred axis. In our simulations, we divide a cell by generating a new cell and placing both cells (gray) at a distance  $\varepsilon$  on the cell division axis in opposite directions of the original position of the mother cell.

### 2.1.3 Growth of incompressible tissues

We now focus on two-dimensional epithelia. In order to provide some general insights in the anisotropic growth, we consider the incompressible limit in which the cell density is constant,  $\rho(\mathbf{r}, t) = \rho_0$ . Furthermore, we do not consider external forces acting on the tissue, i.e.  $f_i^{\text{ext}} = 0$ , and we assume for simplicity that the growth rate  $k_g$ , the apoptosis rate  $k_a$ , the preferred orientation of cell division  $\mathbf{p}$ , the magnitude of the anisotropic stress  $\mu$  and the viscosities  $\eta$  and  $\zeta$  are independent of position but could be functions of time. We choose a coordinate system such that cell division is oriented preferentially along the  $x$ -axis, i.e.  $\mathbf{p} = \mathbf{e}_x$ . In that case, the dynamic equations (2.1) and (2.2) together with the constitutive relation (2.3) are given by

$$\nabla \cdot \mathbf{v} = k_g - k_a, \quad (2.5)$$

$$\eta \Delta \mathbf{v} = \nabla P. \quad (2.6)$$

Cell division and cell death lead to a non-vanishing divergence of the velocity field. The pressure  $P$  plays the role of a Lagrange multiplier to impose the constraint (2.5) for  $\nabla \cdot \mathbf{v}$ . Note that the anisotropic stress of Eq. (2.3) disappears in the force balance (2.6) since it is homogeneous in space so that its divergence vanishes. However, the boundary conditions for the stress given by Eq. (4) do involve the anisotropy of the stress. For arbitrary tissue shapes, the resulting flow field is given by

$$\mathbf{v} = \begin{pmatrix} (k_0 + k_1)x \\ (k_0 - k_1)y \end{pmatrix}, \quad (2.7)$$

where  $k_0 = (k_g - k_a)/2$  and  $k_1 = k_g \mu / (4\eta)$ , and the pressure  $P = P_{\text{ext}} + \zeta(k_g - k_a)$  which is independent of position. Interestingly, we find that the anisotropy of tissue growth

characterized by  $k_1$  is not only determined by the anisotropy of cell division, but does also depend on the tissue viscosity  $\eta$ .

In general, the shape of the tissue is deformed under the flow (2.7). For the simple case of an elliptical tissue boundary, the shape stays elliptical during growth. However, the lengths  $l_x$  and  $l_y$  of the two main axes change with time as  $l_x(t) = l_x^{(0)} \exp(\int_0^t dt' [k_0(t') + k_1(t')])$  and  $l_y(t) = l_y^{(0)} \exp(\int_0^t dt' [k_0(t') - k_1(t')])$ , where  $l_x^{(0)}$  and  $l_y^{(0)}$  are the initial lengths. For  $k_g$ ,  $k_a$  and  $\mu$  constant in time, the area  $A$  of the tissue grows as  $A(t) = A_0 e^{(k_g - k_a)t}$ . The rate  $k_g - k_a$  is therefore related to the effective cell doubling time  $t_2$  via  $t_2 = \ln 2 / (k_g - k_a)$ . Changes of general tissue shapes are discussed in section 2.3, where our theory is compared to recent experimental data showing the shape changes of the wing imaginal disk of the fruit fly *Drosophila melanogaster* during development.

For arbitrary tissue shapes and time independent  $k_g$ ,  $k_a$  and  $\mu$ , average cell trajectories follow flow lines that are described by the power law

$$y = y_0 \left( \frac{x}{x_0} \right)^{\frac{k_0 - k_1}{k_0 + k_1}}, \quad (2.8)$$

where  $(x_0, y_0)$  denotes a reference position on the trajectory. There are two important cases which we want to discuss: (i)  $k_a = 0$ , where no apoptosis occurs, and (ii)  $k_g = k_a$ , where cell division and cell death are balanced. In case (i), Eq. (2.8) also holds for time dependent  $k_g$ , because in this case the ratio  $(k_0 - k_1)/(k_0 + k_1)$  is independent of time. Several cases can be distinguished. For  $\mu = 0$ ,  $k_1 = 0$  so that growth is isotropic and flow lines are radial. For  $0 < \mu < 2\eta$ , the tissue grows at a higher rate along the  $x$ -axis than along the  $y$ -axis. In the special situation where  $\mu = 2\eta$ ,  $k_1 = k_0$  and thus the tissue grows only in one dimension. Finally for  $\mu > 2\eta$ , the tissue shrinks along the  $y$ -axis and grows rapidly along the  $x$ -axis. In case (ii), the velocity field is  $\mathbf{v} = (k_1 x, -k_1 y)$ , and the flow lines obey  $y = y_0(x/x_0)^{-1}$ . This result also holds for time dependent  $k_a$ . In this case, the two-dimensional tissue undergoes so-called convergence-extension rearrangements which imply a spontaneous shear deformation [53]. The growth of a compressible tissue is discussed in appendix A.1.

## 2.2 Discrete model

In order to test our continuum theory for anisotropic tissue growth and to obtain solutions to Eqs. (2.1)-(2.4) in more complex situations where parameters are position dependent, we define a discrete representation of tissue growth in two dimensions following related approaches [32]. This discrete model generates robustly the large scale features of cell rearrangements in growing tissues, but it is not intended to capture details of deformations on the cell scale as e.g. discussed in [76, 31, 38].

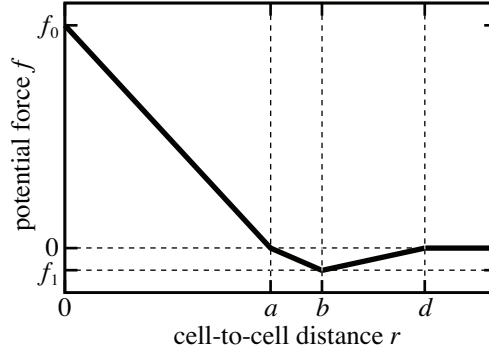


Figure 2.2: Potential force  $f = -dV/dr$  between two cells with centers at distance  $r$ . The force is chosen to be piecewise linear. For  $r \geq d$ , the force vanishes. For  $a < r < d$ , it is attractive with strongest attractive force  $f_1 < 0$  at  $r = b$ . And for  $r < a$ , it is repulsive with maximal force  $f_0 > 0$  at  $r = 0$ .

### 2.2.1 Dynamic equations

We represent cells as elastic objects with the center of the  $i$ -th cell located at position  $\mathbf{x}_i$ . Static forces between the  $N$  cells are described by the potential function

$$U(\mathbf{x}_1, \mathbf{x}_2, \dots, \mathbf{x}_N) = \sum_{\substack{i,j \\ i < j}} V(|\mathbf{x}_i - \mathbf{x}_j|), \quad (2.9)$$

where  $V(r)$  is a pair potential for two cells with centers at distance  $r = |\mathbf{x}_i - \mathbf{x}_j|$ . The pair potential describes adhesive forces as well as elastic forces which keep cell centers at a preferred distance  $a$ . The potential force  $f = -dV/dr$  is chosen to be piecewise linear as defined in Fig. 2.2. The dynamics is described by balancing potential forces with friction forces that account for tissue viscosity. Neglecting for simplicity differences between compressional and shear viscosities, we write the balance of forces acting on cell  $i$  as

$$\bar{\eta} \sum_{\{j:i\}} \left( \frac{d\mathbf{x}_i}{dt} - \frac{d\mathbf{x}_j}{dt} \right) = -\nabla_i U(\mathbf{x}_1, \mathbf{x}_2, \dots, \mathbf{x}_N). \quad (2.10)$$

Here  $\bar{\eta}$  denotes the tissue viscosity on the scale of a cell, and the sum is over the cells  $j$  which are neighbors of cell  $i$ . Neighbors of cell  $i$  are defined as the  $n$  nearest cells and in addition all cells for which  $i$  is within the  $n$  nearest neighbors.

Eq. (2.10) is a discrete form of the force balance Eq. (2.6). We can therefore relate the parameters of the discrete model to the parameters and phenomenological quantities used in Eqs. (2.2) and (2.3). In the vicinity of the preferred cell density  $\rho_p \simeq 2/(\sqrt{3}a^2)$ , the pressure can be estimated as  $P \simeq -\sqrt{3}V'/a$ . The bulk elastic modulus is thus given by  $\chi \simeq \sqrt{3}/2(V'' - V'/a)$ .

### 2.2.2 Oriented cell division and apoptosis

Cell division is implemented as a stochastic process. If cell  $i$  is dividing at time  $t$ , a new cell is created and both cells are positioned with their centers on opposite sides of a circle with radius  $\varepsilon = a/4$  and center at the original position  $\mathbf{x}_i$ , see Fig. 2.1. The axis of cell division is characterized by the angle  $\varphi \in [-\pi/2, \pi/2]$  with respect to the  $x$ -axis. The cell division angle  $\varphi$  is a random variable drawn from a distribution  $Q(\varphi)$ . In the case of isotropic cell division,  $Q(\varphi) = 1/\pi$ . Anisotropies of cell division are captured by a distribution  $Q$  with a peak at a preferred orientation  $\varphi = 0$ , given by the  $x$ -axis, see Fig. 2.1. For simplicity, we use a piecewise constant distribution function to describe anisotropies of cell division with  $Q(\varphi) = 1/(\Delta\varphi)$  for  $-\Delta\varphi/2 < \varphi < \Delta\varphi/2$  and  $Q = 0$  otherwise, i.e.  $\Delta\varphi$  describes the spread of the division angles around the  $x$ -axis. The anisotropic repositioning of the cell pair during division induces a force dipole via the potential  $U$  (see Eq. (2.9) and Fig. 2.2). On average, these force dipoles generate the anisotropic active stress in the continuum limit described by Eq. (2.3).

The division and death events occur at stochastic times. Each cell has an internal clock which measures its lifetime  $t_L$  after which the cell divides with probability  $p$  and dies with probability  $1 - p$ . If cell  $i$  undergoes apoptosis, it is simply removed from the system. In our simulations, the cellular lifetime obeys a Gaussian probability distribution  $R(t_L)$  with average  $\bar{t}_L$  and variance  $\sigma_L \ll \bar{t}_L$ . The effective cell doubling time is  $t_2 = \bar{t}_L \ln 2 / \ln(2p)$ . The growth rate  $k_g$  and the apoptosis rate  $k_a$  in the continuum limit are related to the probability  $p$  and the average cell lifetime  $\bar{t}_L$  by

$$k_g = \frac{p}{2p-1} \frac{\ln 2p}{\bar{t}_L}, \quad (2.11)$$

$$k_a = \frac{1-p}{2p-1} \frac{\ln 2p}{\bar{t}_L}. \quad (2.12)$$

Therefore the probability  $p$  for cell divisions obeys  $p = k_g / (k_g + k_a)$ . A detailed derivation of these relations is given in appendix A.2.

After the repositioning or removal of cells corresponding to division and apoptosis, the system relaxes according to the dynamic Eq. (2.10). In the absence of cell division and apoptosis, there are no fluctuations in this model. As a consequence the system relaxes in this case to a stable configuration with elastic properties. As soon as cell division and apoptosis are introduced, fluctuations appear as a consequence of stochastic events. The growing and dividing system then behaves like a fluid where cells can change their neighbors. The resulting flow field can on large scales be described by the continuum equations introduced above.

We solve the force balance Eq. (2.10) numerically for all cells  $i = 1, \dots, N$  with stochastic cell division and death events drawn randomly from the probability  $p$  and the distributions  $R(t)$  and  $Q(\varphi)$ . At the boundary of the tissue, no external forces are imposed. At each time step the velocities  $d\mathbf{x}_i/dt$  are calculated from Eq. (2.10) using a matrix inversion, and the positions  $\mathbf{x}_i$  of all cells are updated. For details and the parameter values used in our numerical simulations, see appendix A.3.

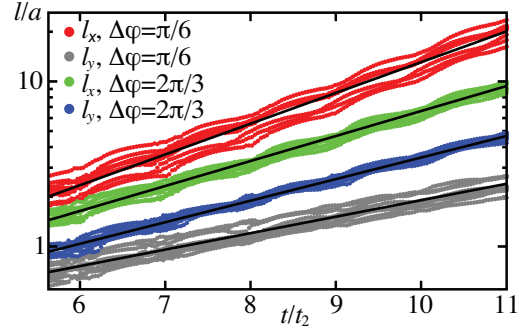


Figure 2.3: Anisotropic growth for different fluctuation amplitudes  $\Delta\varphi$  of the orientation of the cell division axis without apoptosis ( $p = 1$ ). The characteristic lengths  $l_x$  and  $l_y$  of the simulated tissue in  $x$ - and  $y$ -direction normalized by the cell diameter  $a$  are displayed as functions of time  $t$  relative to the effective cell doubling time  $t_2 = \bar{t}_L$ . Ten independent realizations are shown for each value of  $\Delta\varphi$ . The black lines represent linear fits from which the growth rates  $k_x$  and  $k_y$  are determined. Parameter values are given in appendix A.3, and  $\xi = 0.165$ .

### 2.2.3 Results of numerical simulations

We discuss shape changes and average cell trajectories obtained in our growth simulations. We first consider the case where no apoptosis occurs ( $p = 1$ ). The anisotropic shape of an epithelium can be characterized by the variances of cell distributions  $I_{ab} = (1/N) \sum_i (x_a^{(i)} - \bar{x}_a)(x_b^{(i)} - \bar{x}_b)$ , where  $x_a^{(i)}$  denotes the components  $a = x, y$  of the vector  $\mathbf{x}_i$ . Fig. 2.3 shows the increase of the linear dimensions  $l_x = \sqrt{I_{xx}}$  and  $l_y = \sqrt{I_{yy}}$  as functions of time for two different angular variations of cell division  $\Delta\varphi$ . The tissue grows exponentially with different growth rates  $k_x$  and  $k_y$  which depend on  $\Delta\varphi$ , consistent with Eq. (2.7). Indeed,  $k_x + k_y \simeq k_g$  where  $k_g = \ln 2/t_2$ , independent of  $\Delta\varphi$ , see Fig. 2.4 (inset). The dependence of  $k_1 = (k_x - k_y)/2$  as a function of  $\Delta\varphi$  is shown in Fig. 2.4 for three different values of the dimensionless parameter  $\xi = \bar{\eta}a/(\bar{t}_L f_0)$ . Since  $\chi \simeq f_0/a$ , the parameter  $\xi \simeq \bar{\eta}/(\chi t_2)$  characterizes the ratio of growth rate and cellular relaxation rate. The anisotropic component of growth is given by  $k_1/k_g \simeq \alpha(\pi - \Delta\varphi)$ , where  $\alpha$  is the slope of the curves in Fig. 2.4. The coefficient  $\alpha(\xi)$  depends weakly on  $\xi$  in a non-monotonous manner, see Fig. 2.4. Since  $k_1 \simeq k_g \mu/(4\eta)$ , we can determine  $\mu/\eta \simeq 4\alpha(\pi - \Delta\varphi)$  of the continuum limit. Fig. 2.5 represents average trajectories of cells and their descendants in the  $xy$ -plane. The double logarithmic plot reveals that the average positions exhibit a power law as described by Eq. (2.8). We find that for each set of parameters, the slope of the linear fit is indeed given by  $k_y/k_x$ .

We now consider the effects of apoptosis in tissues with anisotropic cell division. Fig. 2.6 shows the shape changes of tissues for  $p = 0.5$  and two different choices of  $\Delta\varphi$ . In this case no net growth occurs since proliferation and apoptosis are balanced. Displayed are the relative changes in length of the principal axes  $l_x/l_x^{(0)}$  and  $l_y/l_y^{(0)}$ , where  $l_{x,y}^{(0)}$  are

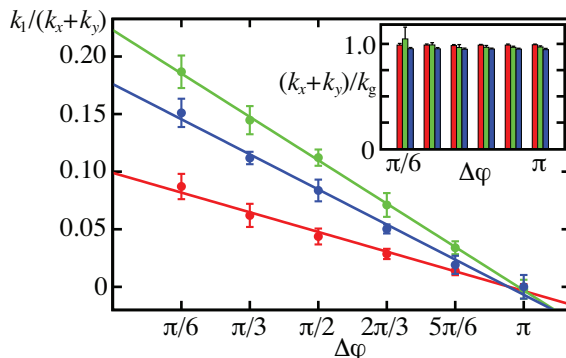


Figure 2.4: Anisotropic growth rate  $k_1 = (k_x - k_y)/2$  normalized by the total growth rate  $k_x + k_y$  as a function of  $\Delta\varphi$  for  $\xi = 0.00165$  (red),  $\xi = 0.0165$  (green), and  $\xi = 0.165$  (blue). No apoptosis occurs ( $p = 1$ ). The data points and standard deviations are obtained from ten independent simulations for each set of parameters. The inset shows the total growth rate  $k_x + k_y$  normalized by the rate  $k_g = \ln 2/t_2$  defined by the effective cell doubling time  $t_2 = \bar{t}_L$ .

the corresponding values of the initial configuration. The logarithmic plot shows that the lengths  $l_x$  and  $l_y$  grow and shrink exponentially with rates  $k_x$  and  $k_y$  as described by Eq. (2.7). The total growth rate  $k_x + k_y \simeq 0$ , consistent with equal rates for cell division and cell death. As in the case without cell death,  $k_1 = (k_x - k_y)/2$  depends linearly on the variation of the cell division angle  $\Delta\varphi$ .

In summary, we have shown that oriented cell division in a developing organ leads to anisotropic tissue growth. The anisotropy of growth rates depends on biophysical properties of cells, in particular on tissue viscosity. Our continuum theory of an incompressible tissue predicts flow fields and cell trajectories which describe well the average behaviors observed in stochastic simulations of anisotropic growth. In our simulations, small differences between the observed total growth rate  $k_x + k_y$  and the rate  $k_g$  defined by the average cell doubling time arise as a result of tissue compressibility.

The parameter values used in our growth simulations are motivated by studies of the wing imaginal disk of the fruit fly. Key parameters are the bulk elastic modulus  $\chi$  and the viscosity  $\bar{\eta}$  of the two-dimensional tissue. We estimate  $\chi \simeq \chi_{3d}h \simeq 6 \cdot 10^{-3} \text{ N/m}$ , where  $\chi_{3d} \simeq 200 \text{ Pa}$  is the shear modulus of a cell and  $h \simeq 30 \mu\text{m}$  is the height of the epithelium. The choice  $\xi = 0.0165$  thus corresponds to a local two-dimensional tissue viscosity of  $\bar{\eta} \simeq 3 \text{ Ns/m}$ . Using the tissue height  $h$ , this corresponds to a viscosity of  $\eta_{3d} \simeq 10^5 \text{ Pa s}$  which is a typical value that has been reported in experiments [40].

Our work shows that oriented cell division has interesting consequences for cell rearrangements in a growing tissue. In the special case where apoptosis balances cell division, the tissue does not grow but spontaneously undergoes a shear deformation similar to so-called convergence-extension transformations. Oriented cell division can therefore control shape changes of tissues during development.



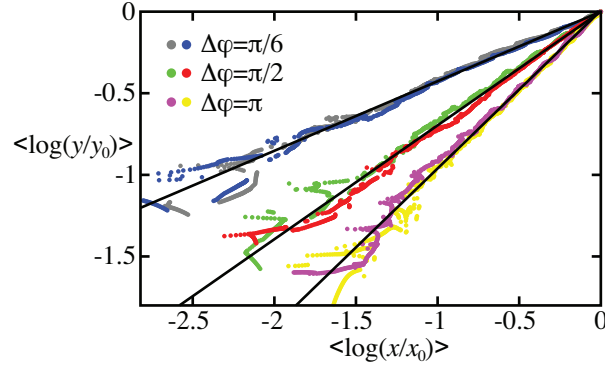


Figure 2.5: Averaged cell trajectories in growing tissues without apoptosis ( $p = 1$ ). The averages  $\langle \log(x/x_0) \rangle$  and  $\langle \log(y/y_0) \rangle$  of the positions  $(x, y)$  of all descendants of an initial cell are displayed for different times during growth. Coordinates are normalized with respect to the final positions  $(x_0, y_0)$ . For three values of  $\Delta\varphi$ , two examples are displayed each. The black lines represent linear fits which characterize the power law of Eq. (2.8). Simulations are performed for  $\xi = 0.165$  and cell trajectories are studied from the four-cell stadium on for 13 cell doubling times.

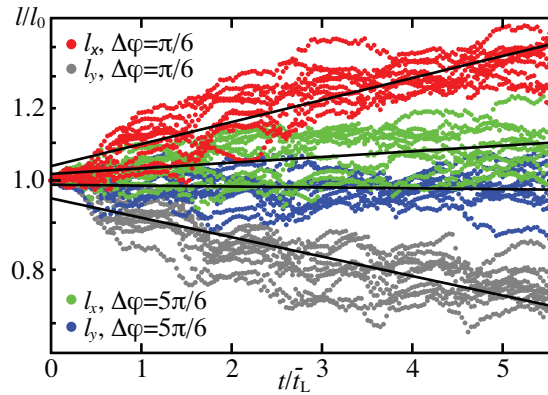


Figure 2.6: Anisotropic tissue deformation for growth with balanced apoptosis ( $p = 0.5$ ). Data for two different fluctuation amplitudes  $\Delta\varphi$  of the orientation angles of cell division are shown. The lengths  $l_x$  and  $l_y$  normalized to their corresponding initial values  $l_{x,y}^{(0)}$  are plotted as a function of time  $t$  relative to the average lifetime  $\bar{t}_L$ . For each value of  $\Delta\varphi$ , ten independent realizations are shown. The growth rates  $k_x$  and  $k_y$  are determined from linear fits (black lines), and  $\xi = 0.00165$  for all simulations.

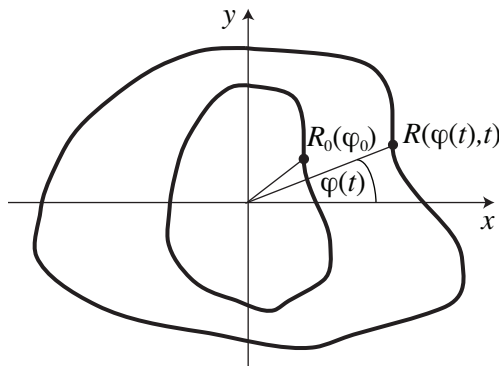


Figure 2.7: Shape change of an epithelium boundary due to anisotropic tissue growth. The tissue boundary is shown at the initial time  $t_0$  and the later time  $t$ . The preferred orientation of the cell division axis is  $\mathbf{p} = \mathbf{e}_x$ . The position of a cell which is situated at the tissue boundary is marked by a dot and described by the radial distances  $R_0(\varphi_0)$  and  $R(\varphi(t), t)$ . The polar angle describing the position of the marked cell changes from the initial angle  $\varphi_0 = \varphi(t_0)$  to the later angle  $\varphi(t)$ .

## 2.3 Shape changes of growing epithelia

We now apply our continuum description of anisotropic tissue growth to experimental data. For that, we first study how the shapes of epithelia change due to the cell rearrangements described by our theory. We then compare our theoretical results to experimentally measured shape changes of the *Drosophila* wing disk. We show that our theory of the growth of incompressible tissues describes the data very well, and we estimate the isotropic and anisotropic parts of the growth rate.

In section 2.1.3, we have discussed the flow velocity of cell rearrangements in a growing incompressible epithelium with preferred orientation of cell division along the  $x$ -axis. We now consider the effect of these cell movements on the shape of an epithelium boundary which moves with the flow velocity given in Eq. (2.7). For simplicity, we focus on the case of constant growth rates  $k_0$  and  $k_1$ .

We describe the position of the tissue boundary at time  $t$  by

$$\begin{pmatrix} x(t) \\ y(t) \end{pmatrix} = R(\varphi, t) \begin{pmatrix} \cos\varphi \\ \sin\varphi \end{pmatrix}, \quad (2.13)$$

so that the whole information about the tissue shape is captured by the radial distance  $R(\varphi, t)$  of the epithelium boundary in respect to the center of mass of the tissue at polar angle  $\varphi$ . At time  $t_0$ , we describe the tissue shape by  $R_0(\varphi) \equiv R(\varphi, t_0)$ . For anisotropically growing tissues, cell movements are non-radial. Thus the polar angle describing the position of a cell which is located at the tissue boundary changes during development, see Fig. 2.7. From the cell trajectories  $x(t) = x_0 \exp((k_0 + k_1)(t - t_0))$ ,  $y(t) = y_0 \exp((k_0 - k_1)(t - t_0))$  that result from the flow velocity (2.7) in the case of

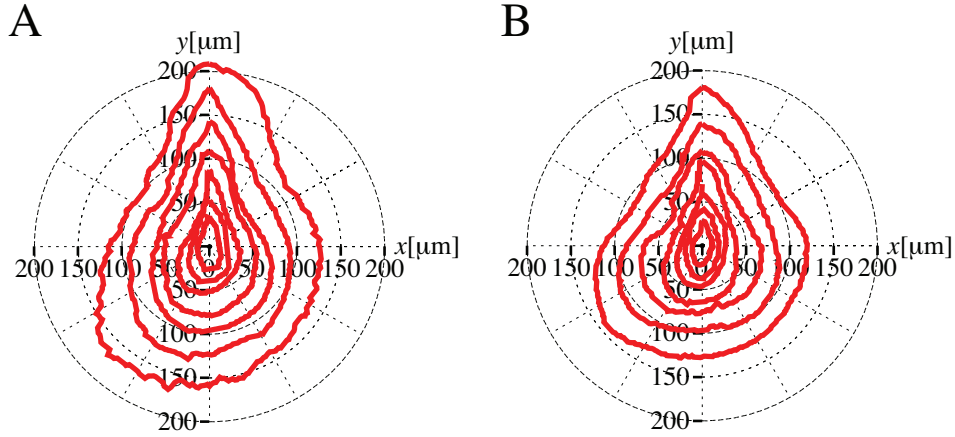


Figure 2.8: Shapes of the *Drosophila* wing disk during development. In the polar plots, 7 examples of individual WT (A) and GFP-Dpp disks (B) are illustrated. The disk ages vary between  $t_0 = 24$  h and  $t_f = 66$  h. Details of the experiments are discussed in appendix A.5.

constant growth rates, the radial distance  $R(\varphi, t)$  of the tissue boundary at time  $t$  can be calculated (see appendix A.4) as

$$R(\varphi, t) = R_0(\arctan(\tan(\varphi)e^{2k_1(t-t_0)}))e^{k_0(t-t_0)} \left( \sin^2\varphi e^{2k_1(t-t_0)} + \cos^2\varphi e^{-2k_1(t-t_0)} \right)^{-1/2}. \quad (2.14)$$

Fig. 2.8 shows experimentally measured shapes of wing imaginal disks at different stages during development. The experiments are done with two different kinds of wing disks: wildtype (WT) disks (see Fig. 2.8, A), where the morphogen Dpp is produced in normal amount, and GFP-Dpp disks (see Fig. 2.8, B), where Dpp fused to the green fluorescent protein GFP is produced in addition to the endogenous Dpp. These two different kinds of disks are used in order to study whether Dpp has an influence on the anisotropy of growth. For the exponential growth phase of the disks (see Fig. A.1), we determine the effective growth rates  $k_{\text{eff}}(\varphi)$  with which the radial distance  $R(\varphi, t)$  of the disk boundary increases on average at angle  $\varphi$ , see appendix A.5. In Fig. 2.9,  $k_{\text{eff}}$  is plotted for different polar angles. We find that the effective growth rates differ with varying polar angle. The angular distribution of the growth rates has a maximum along the  $x$ -axis and a minimum near the  $y$ -axis for both WT and GFP-Dpp disks. The average growth rate is slightly smaller for GFP-Dpp than for WT disks, whereas the difference between the maximal and minimal growth rate is significantly bigger for GFP-Dpp than for WT disks.

We now compare these results with our continuum theory of anisotropic tissue growth. For incompressible tissues which grow at the constant rates  $k_0$  and  $k_1$  with preferred orientation of cell division along the  $x$ -axis (see section 2.1.3), the change of the disk boundary is described by Eq. (2.14). The effective growth rate  $k_{\text{eff}}(\varphi) =$

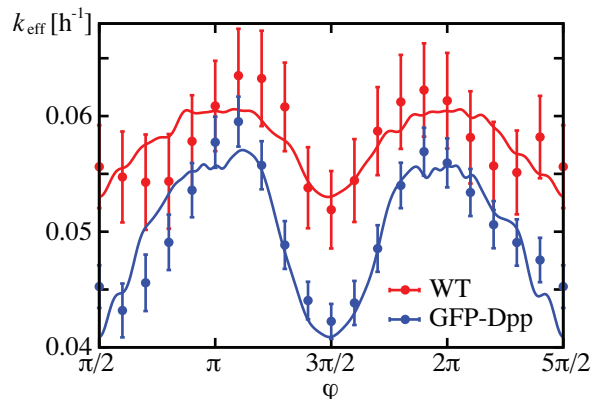


Figure 2.9: Effective growth rates for the developing *Drosophila* wing disk during its exponential growth phase as a function of the polar angle  $\varphi$  for WT and GFP-Dpp disks. The dots represent  $k_{\text{eff}}$  determined from the experimental data, see appendix A.5. The error bars indicate the standard errors for  $k_{\text{eff}}$  of the individual fits of Eq. (A.16) to the data. The solid lines represent fits of Eq. (2.15) to the experimentally determined values of  $k_{\text{eff}}$ .

$\frac{1}{t_f - t_0} \int_{t_0}^{t_f} \frac{\dot{R}(\varphi, t)}{R(\varphi, t)} dt$  is thus given by

$$k_{\text{eff}}(\varphi) = k_0 - \frac{1}{2(t_f - t_0)} \log \left( \sin^2 \varphi e^{2k_1(t_f - t_0)} + \cos^2 \varphi e^{-2k_1(t_f - t_0)} \right) + \frac{1}{t_f - t_0} \log \left( \frac{R_0 \left( \arctan \left( \tan(\varphi) e^{2k_1(t_f - t_0)} \right) \right)}{R_0(\varphi)} \right). \quad (2.15)$$

We fit this equation to the effective growth rates measured in the wing disk, using  $k_0$  and  $k_1$  as fit parameters.  $R_0$  is determined from the average initial wing disk shape, see appendix A.5. As best fit parameters, we get  $k_0 = 0.0569 \pm 0.0001 \text{ h}^{-1}$ ,  $k_1 = 0.0036 \pm 0.0002 \text{ h}^{-1}$  for WT disks, and  $k_0 = 0.0485 \pm 0.0001 \text{ h}^{-1}$ ,  $k_1 = 0.0067 \pm 0.0002 \text{ h}^{-1}$  for GFP-Dpp disks. The ratio between the isotropic part  $k_0$  of the growth rate for GFP-Dpp disks and WT disks is 0.85, i.e.  $k_0$  is in the same range for both types of disks. Note, however, that the anisotropic part  $k_1$  of the growth rate is increased by a factor of 1.9 in GFP-Dpp disks in respect to WT disks.

In summary, we have shown that our continuum theory of anisotropic tissue growth provides a good description for the shape changes of the *Drosophila* wing disk. For the exponential growth phase of the disk, we have determined the growth rates  $k_0$  and  $k_1$ , from which we can calculate the effective cell doubling time  $t_2 = \ln 2 / (2k_0)$  (see section 2.1.3) as  $t_2 = 6.09 \pm 0.01 \text{ h}$  for WT disks and  $t_2 = 7.15 \pm 0.01 \text{ h}$  for GFP-Dpp disks. The data shows that tissue growth is not homogeneous. It is faster along the  $x$ -axis (DV boundary) than along the  $y$ -axis (AP boundary). Since apoptosis is negligible during the exponential growth phase, we can estimate the strength of the anisotropic stress

---

generated by oriented cell division normalized by the tissue viscosity via  $\mu/\eta = 2k_1/k_0$ . We find  $\mu/\eta = 0.13 \pm 0.01$  for WT disks and  $\mu/\eta = 0.28 \pm 0.01$  for GFP-Dpp disks. In the case of Dpp overexpression, the anisotropic stress is thus increased by a factor of 2.2 as compared to WT disks. This suggests that the morphogen Dpp is involved in the regulation of the orientation of the cell division axis. Dpp builds a graded concentration profile along the  $x$ -axis which coincides with the preferred axis of cell division. However, the mechanism how Dpp might regulate the orientation of cell division remains unclear and is subject to future work. As a first step, we study in sections 3.2 and 3.3 how Dpp is spread in the growing wing disk, and in section 3.4 we discuss possible rules how Dpp could control the isotropic part  $k_0$  of the growth rate.



## Chapter 3

# Morphogen gradients in growing tissues

After the study of cell rearrangements in growing epithelia in the preceding chapter, we now focus on the spreading of morphogens within growing tissues. For the situation where growth effects can be neglected, it was shown that morphogen spreading via transcytosis can effectively be described by a nonlinear diffusion equation [17, 18, 19], see section 1.1. Based on the flow profiles of cell movements that result from oriented cell division and apoptosis, we show that tissue growth leads to an additional drift term in the diffusion equation which captures the stretching and dilution of the morphogen gradient (see section 3.2). We derive the steady-state profile of the resulting diffusion-advection equation and discuss its general features.

We apply our theory of morphogen transport in growing tissues to recent experiments on the spreading of the morphogen Dpp in the developing wing disk. By analyzing fluorescence recovery after photobleaching (FRAP) experiments, we determine the kinetic parameters of Dpp spreading during wing disk development (see section 3.1 and 3.3), and we show that Dpp transport is mainly intracellular [55]. Using the kinetic parameters, we numerically calculate the Dpp concentration profile as a function of larval age for the whole wing disk development (see section 3.3). We show that the Dpp concentration profile during development is well described by a succession of adiabatically changing steady-state gradients. Moreover, we find that the growth effects of dilution and stretching have no significant influence on the Dpp gradient and can be neglected throughout development. However, tissue growth strongly affects the cellular Dpp concentration, since the cells move away from the Dpp source due to growth.

Finally, we investigate the relation between the tissue growth rate and the cellular Dpp concentration in the wing disk (see section 3.4). We show that, at a late stage of disk development, the relative change of the cellular Dpp concentration in time becomes independent of position and is related linearly to the growth rate. Using numerical simulations, we study a possible rule for growth control by the relative rate of change of the cellular Dpp concentration. With this rule, we can reproduce the measured area growth of the wing disk at a late stage of development, but not at earlier times. We then

analyze measured concentration profiles of P-Mad during wing disk development, which mediates Dpp signaling inside the cells, see section 1.1. A quantitative description of how the cellular Dpp concentration might be related to the P-Mad concentration is discussed in chapter 4. Here, we show that the relative rate of change of the cellular P-Mad concentration is independent of position in the wing disk and related unambiguously to the growth rate throughout development. Thus, we can propose a rule how P-Mad could control the growth rate during the whole wing disk development.

### 3.1 Dpp spreading in the Drosophila wing disk

The morphogen Dpp is produced at the anterior-posterior (AP) compartment boundary in the Drosophila wing disk [11], see Fig. 1.2. From there Dpp molecules spread non-directionally into the receiving tissue, are degraded while spreading and form a graded concentration profile [36, 92]. In disks at a late stage of development when effects resulting from tissue growth can be neglected (see Fig. A.1 for the slowing down of growth), Dpp spreading can be described by the following 2d diffusion equation, regardless of the actual transport mechanism (see section 1.1)

$$\partial_t c(\mathbf{r}, t) = \nabla(D\nabla c(\mathbf{r}, t)) - kc(\mathbf{r}, t) + \nu\Theta(-x)\Theta(x + w). \quad (3.1)$$

Here  $c$  is the Dpp concentration,  $D$  is the diffusion coefficient,  $k$  is the degradation rate,  $\nu$  is the production rate describing the number of produced Dpp molecules per time and area, and  $w$  is the width of the Dpp source. The coordinate system is chosen such that the AP boundary is situated at  $x = 0$  and that the Dpp source is located in a stripe between  $x = -w$  and  $x = 0$ , see Fig. 1.2.

In section 1.1, we have summarized how a microscopic model of morphogen spreading via intracellular trafficking and extracellular diffusion leads to the macroscopic diffusion equation (3.1) with concentration dependent  $D$  and  $k$  [17, 18, 19]. Here we consider  $D$  and  $k$  to be homogeneous, which will be sufficient to describe the experimental data.

#### 3.1.1 Concentration profile in steady state

In order to reduce Eq. (3.1) to a one dimensional problem, we consider the symmetry of the spread of Dpp molecules in the wing disk. Since the Dpp source is a stripe of cells parallel to the  $y$ -axis, the spread of Dpp molecules in the disk is invariant under translations in the  $y$ -direction (see Eq. (3.1) if we neglect boundary effects. Although not infinite, the region where the Dpp gradient forms is considerably large and shows a homogeneous concentration in the  $y$ -direction, see Fig. 1.2. The Dpp concentration hence obeys  $c(\mathbf{r}, t) \approx c(x, t)$ . At a late stage of development when growth effects can be neglected, the Dpp concentration in steady state is thus characterized by

$$D\partial_x^2 c(x) - kc(x) + \nu\Theta(-x)\Theta(x + w) = 0. \quad (3.2)$$

Since the width of the disk is much larger than the length scale on which the Dpp gradient decays, we can consider the disk as infinitely large in  $x$ -direction. As boundary



conditions, we impose a vanishing concentration for  $x \rightarrow \pm\infty$ , and at the boundaries of the Dpp source at  $x = -w$  and  $x = 0$  the concentration and the flux  $j = -D\partial_x c + k_x x c$  are imposed to be continuous functions. Under these conditions, the Dpp concentration in steady state is given by

$$c(x) = \begin{cases} C_0 \exp\left(\frac{w+x}{\lambda}\right) & x \leq -w \\ \frac{\nu}{2k} \left(2 - \exp\left(\frac{x}{\lambda}\right) - \exp\left(\frac{-w-x}{\lambda}\right)\right) & -w \leq x \leq 0 \\ C_0 \exp\left(-\frac{x}{\lambda}\right) & x \geq 0 \end{cases} \quad (3.3)$$

Here  $\lambda = \sqrt{D/k}$  is the decay length of the Dpp gradient, and  $C_0 = \frac{\nu}{2k} (1 - \exp(-\frac{w}{\lambda}))$  is the concentration at  $x = 0$ .

In the receiving tissue, the shape of the Dpp gradient is thus determined by  $\lambda$  and  $C_0$  which depend on the kinetic parameters  $D$ ,  $k$  and  $\nu$ , as well as on the width of the Dpp source  $w$ . Interestingly,  $C_0$  saturates with an increasing width of the source for  $w \gg \lambda$ . This saturation results from the fact that Dpp molecules are also degraded within the source. If the source becomes much larger than the decay length of the Dpp gradient, there is a high probability that molecules produced at the center of the source will be degraded before they diffuse to the boundary of the source.

### 3.1.2 FRAP experiments: measuring the kinetic parameters

We measured the kinetic parameters  $D$ ,  $k$  and  $\nu$  of the Dpp gradient in the wing disk using FRAP experiments [55]. In these experiments, performed by P. Pantazis [77] and A. Kicheva [56] in disks at a late stage of development when growth slows down (disk ages between 90 h and 120 h, see Fig. A.1), Dpp molecules are labeled with the green fluorescent protein GFP and visualized under the confocal microscope, using a low-intensity 488 nm laser beam. During the bleaching process, the GFP-Dpp molecules are photobleached in a stripe of dimensions  $h = 10 \mu\text{m}$  by  $200 \mu\text{m}$  adjacent to the source by irradiation with a high-intensity laser beam. In the following hour, the recovery of the fluorescence intensity in the bleached region is recorded at two minutes intervals, see Fig. 3.1, D to K.

The average total fluorescence intensity in the bleached stripe is quantified and calibrated to GFP-Dpp concentration. Fig. 3.1, A shows the calibration of the fluorescence intensity in counts/pixel to concentration in molecules/ $\mu\text{m}^2$ . For the intensities measured in the FRAP experiments, the fluorescence intensity is related linearly to the GFP-Dpp concentration. We used our calibrations to estimate the Dpp concentration  $C_0$  at the boundary of the source. The steady-state gradient (3.3) for  $x > 0$  was fitted to the Dpp gradients before bleaching, see Fig. 3.1, B. Indeed the gradients were well described by a single exponential function. We found  $C_0 = 802 \pm 312$  molecules/ $\mu\text{m}^2$  ( $n = 8$  experiments). Moreover, the fits of the steady-state gradients before bleaching yield the decay length  $\lambda = 20.2 \pm 5.7 \mu\text{m}$  [55].

In order to determine the kinetic parameters  $D$ ,  $k$  and  $\nu$ , we then studied the recovery curves of the total fluorescence intensity after photobleaching normalized to the value before bleaching, plotted in Fig. 3.1, C. We observed that the fluorescence did not

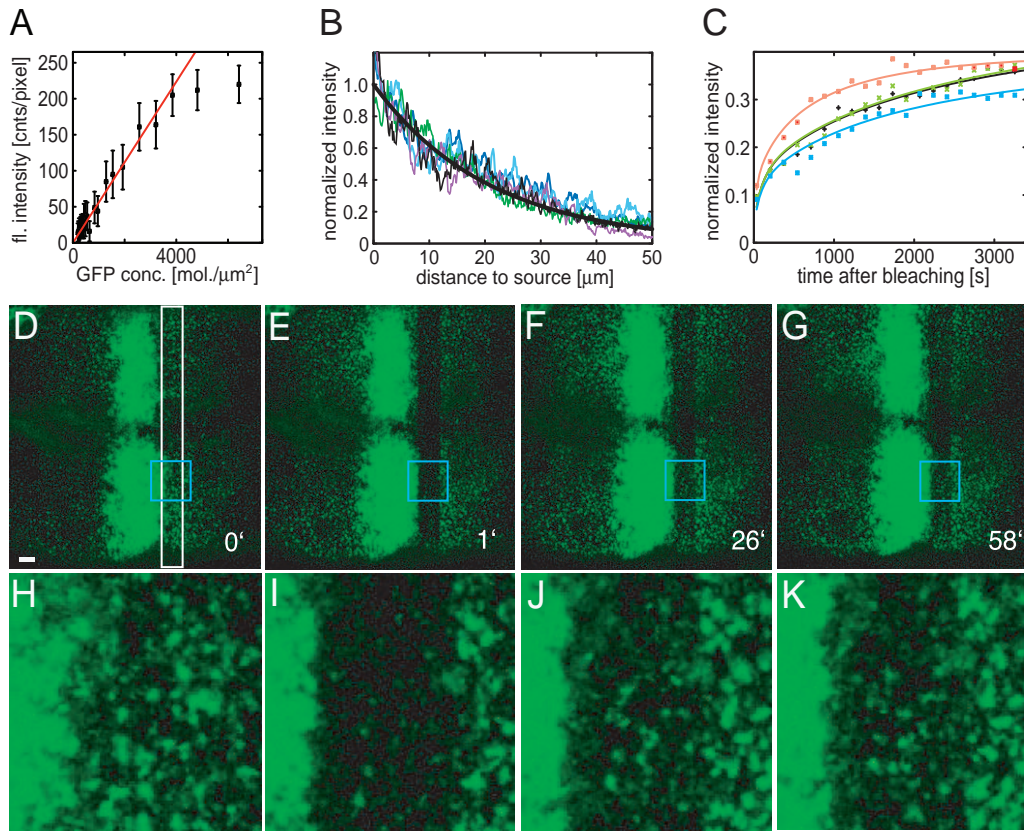


Figure 3.1: FRAP experiments in GFP-Dpp wing disks. (A) Calibration of the fluorescence intensity to GFP concentration. The error bars represent standard deviations of 3 independent measurements for each concentration, which were done under the same imaging conditions as used for the FRAP experiments. The red line represents a linear fit to the data. (B) GFP-Dpp gradients before bleaching. The fluorescence intensity normalized to its value at  $x = 0$  is plotted as a function of the distance  $x$  to the source. Different colors represent the data sets of five different GFP-Dpp disks, the black line is an exponential fit to the black trace. (C) FRAP curves for four GFP-Dpp disks. The total fluorescence intensity normalized to its value before bleaching is plotted as a function of time after bleaching. The solid lines represent fits of the function  $f(t)$  to the recovery curves. (D-G) Time-lapse images of FRAP experiments in GFP-Dpp disks. The images show the fluorescent signals recorded with the confocal microscope immediately before bleaching (D), immediately after bleaching (E), and during the recovery phase 26 and 58 minutes after the start of the experiment (F,G). The white box in D indicates the stripe which is bleached, the scaling bar corresponds to  $10 \mu\text{m}$ . The blue boxes are magnified in (H-K). All pictures are oriented such that the anterior region is on the left. Figure modified from [55].

recover completely during the experiment, i.e. there is a fraction  $\psi$  of molecules which is immobile on the time scale of the FRAP experiment.

Now to calculate the fluorescence recovery curves, we have to solve Eq. (3.1) in one dimension. As initial condition, we impose the steady-state gradient  $c(x, 0) = C_0 e^{-x/\lambda}$  outside of the bleached region at  $x < d$  and  $x > d + h$ , and  $c(x, 0) = bC_0 e^{-x/\lambda}$  inside the bleached region for  $d < x < d + h$ , where  $d$  is the distance of the bleached stripe from the source,  $h$  is its width, and  $b$  is the bleaching depth. The analytical solution of this problem is [55]

$$c(x, t) = \left[ 1 + b + (b - 1) \left( -A(-x, t) + e^{2x/\lambda} \left( -A(x, t) + A(h + x, t) \right) - 1 + A(h - x, t) \right) \right] \times \frac{(1 - \psi)C_0}{2} e^{-x/\lambda} + c_\psi(x), \quad (3.4)$$

where  $A(x, t) = \text{erf} \left( \frac{d+2Dt/\lambda+x}{2\sqrt{Dt}} \right)$  with the error function  $\text{erf}(x) = 2/\sqrt{\pi} \int_0^x \exp(-q^2) dq$  (see e.g. [2]), and  $c_\psi(x)$  represents the concentration of immobile molecules which is constant in time:  $c_\psi(x) = \psi C_0 e^{-x/\lambda}$  outside of the bleached region and  $c_\psi(x) = b\psi C_0 e^{-x/\lambda}$  inside the bleached region. From Eq. (3.4), one can now calculate the average concentration  $f(t)$  in the bleached region by  $f(t) = 1/h \int_d^{d+h} c(x', t) dx'$  (see [55] for the explicit expression of  $f(t)$ ).

The theoretical recovery curve  $f(t)$  of the concentration in the bleached stripe is fitted to the experimental data, see Fig. 3.1, C. The parameters  $C_0$  and  $\lambda$  are known from the steady-state gradient, as well as the parameters  $d = 2 \mu\text{m}$  and  $h = 10 \mu\text{m}$  characterizing the bleached stripe. The kinetic parameters  $D$  and  $\psi$  are optimized, and together with  $\lambda$  and  $C_0$ , the degradation rate  $k$  and the production rate  $\nu$  can be calculated. The diffusion coefficient for GFP-Dpp is  $D = 0.10 \pm 0.05 \mu\text{m}^2/\text{s}$ , the degradation rate is  $k = (2.52 \pm 1.29) 10^{-4} \text{s}^{-1}$ , the production rate is  $\nu = 0.64 \pm 0.38 \text{ molecules}/(\mu\text{m}^2\text{s})$  and the immobile fraction is  $\psi = 62 \pm 8\%$  ( $n=8$  experiments) [55].

Eq. (3.4) describes the concentration for a situation where the bleaching occurs instantaneously. In reality, however, the bleaching process takes about 45s and the first image after bleaching can be taken another 10-25s later. A finite bleaching time complicates the problem, which can then only be solved numerically. Therefore, we assume for our analysis that bleaching occurs instantaneously 25s before the first image. It has been verified that our results do not depend sensitively on the choice of this time between 10s and 70s [55]. Since some fluorescence already recovers during the bleaching process, we include the bleaching depth  $b$  as a fit parameter in our analysis.

In order to validate our fitting procedure and to compare it to the standard procedure of fitting a solution of the diffusion equation without degradation and production to the FRAP experiment ([8], modified in [18]), we have numerically calculated solutions of Eq. (3.1) in  $1d$  which take a finite bleaching time into account. In these simulations, we generated FRAP curves with data points at 180s intervals. We used the fitting procedure described above and compared the optimized values of the parameters with the input values. While the parameters obtained by our fitting procedure were at most 15% different from the input values, the parameters obtained by the standard procedure

deviated substantially from the ones used in the numerical calculations. Thus production and degradation are not negligible to account for the FRAP recovery curves.

### 3.1.3 Dpp transport dominated by intracellular trafficking

In order to determine the dominant transport mechanism of Dpp in the wing disk, i.e. to distinguish between extracellular diffusion and intracellular trafficking (transcytosis), we performed FRAP experiments in thermosensitive “shibire-rescue” mutant flies [55]. In these flies, endocytosis can be blocked by raising the temperature to 34°C, at which the function of the protein Dynamin is blocked which is needed for the formation of endocytic vesicles [26]. However, the GFP-Dpp producing cells in the source are rescued with a Dynamin transgene and are able to perform endocytosis and GFP-Dpp expression at a normal level. Thus endocytosis is blocked in the receiving tissue, but not in the GFP-Dpp secreting source. At 32°C, endocytosis is blocked partially, and at 25°C, it is released [36].

In shibire-rescue animals which were shifted to a temperature of 34°C a few minutes prior to the experiment, no recovery of the GFP-Dpp concentration could be detected within the bleached stripe, see Fig. 3.2, A and D to K. When the temperature was shifted down to 25°C, fluorescence recovered into the bleached stripe, which indicates that the endocytic block was reversible and that the lack of recovery was not due to tissue damage.

The lack of fluorescence recovery in shibire-rescue flies at 34°C could be either a result of a decreasing diffusion coefficient or an increasing degradation rate. The theoretically determined recovery curve  $f(t)$  could not be fitted to this data, because no recovery occurred. Thus, in order to distinguish between the two possibilities of decreased diffusion or increased degradation, we performed FRAP experiments in shibire-rescue animals at 32°C where endocytosis is partially blocked, see Fig. 3.2, B and C. For this case, the theoretical curve could be fitted to the data. The explicit values for  $D$ ,  $k$ ,  $\nu$  and  $\psi$  are given in Table 3.1, in which the kinetic parameters of all experiments are summarized. We found that at 32°C, the diffusion coefficient decreased by a factor of about 2 compared to control animals at 32°C and to shibire-rescue mutants at 25°C. The degradation rate was not increased, but decreased by a factor of about 2. Therefore, we can conclude that Dpp movement requires endocytosis, and that Dpp transport is mainly intracellular.

Now as discussed in section 1.1, intracellular trafficking leads to a concentration dependent diffusion coefficient  $D$  and degradation rate  $k$ . However, we considered a position independent diffusion coefficient and degradation rate for our data analysis. In order to test the validity of our analysis, FRAP experiments were performed in different geometries. In these experiments, the width of the bleached stripe is increased to 20  $\mu\text{m}$  or is located 20  $\mu\text{m}$  away, instead of adjacent to the source. Alternatively, a stripe perpendicular to the source is bleached instead of parallel, and recovery curves are fitted simultaneously to squares of 10  $\mu\text{m}$  width. And finally, a 30  $\mu\text{m} \times 30 \mu\text{m}$  square is bleached next to the source, and recoveries in two different regions embedded within each other are analyzed. The theoretical recovery curves and the fits to the experimental data for these different geometries are discussed in [55]. The values obtained for the kinetic parameters

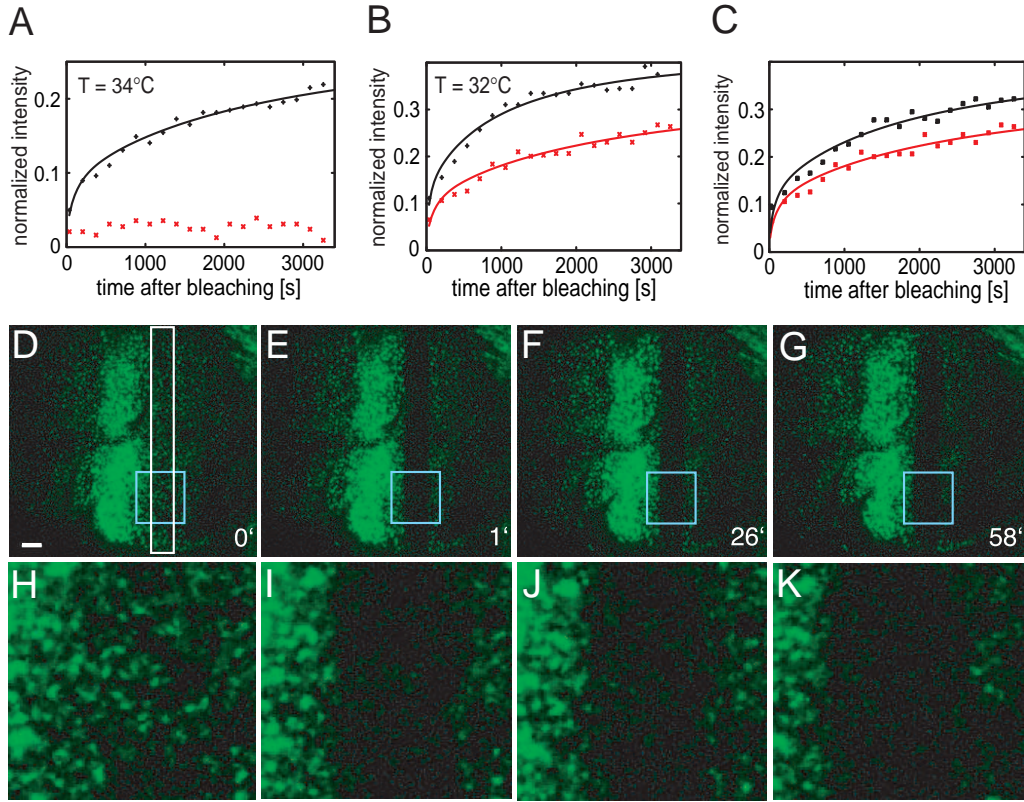


Figure 3.2: FRAP experiments in GFP-Dpp shibire-rescue mutant flies. (A,B) FRAP curves for GFP-Dpp (black) and shibire-rescue disks at 32°C (A) and 34°C (B). The fluorescence intensity normalized to its pre-bleach value is plotted as a function of time after the bleaching process. The solid lines represent fits of the theoretical recovery curves  $f(t)$  to the data. (C) FRAP curves for shibire-rescue disks at 25°C (black) and 32°C (red). (D-G) Time-lapse images of FRAP experiments in shibire-rescue mutant disks at 34°C. The images show the GFP-Dpp fluorescence measured with the confocal microscope immediately before bleaching (D), immediately after bleaching (E), and during the recovery phase 26 and 58 minutes after the start of the experiment (F,G). The white box in D indicates the stripe which is bleached, the scaling bar corresponds to 10  $\mu\text{m}$ . The blue boxes are magnified in (H-K). All pictures are oriented such that the anterior region is on the left. Figure modified from [55].

$D$ ,  $k$ ,  $\nu$  and  $\psi$  are shown in Table 3.1. We find that the results of these experiments are consistent with the independence of the four kinetic parameters on position in the tissue. In terms of the transcytosis model [17, 18, 19], it is likely that we are in a regime where  $D$  and  $k$  only depend weakly on position, and of course a weak position dependence of  $D$  and  $k$  might be hidden in the data.

experiment description		$D$ [ $\mu\text{m}^2/\text{s}$ ]	$k$ [ $\text{s}^{-1}$ ] $\times 10^{-4}$	$\psi$	$\nu$ [molec./( $\text{s cell}$ )]	$R^2$	$n$
GFP-Dpp	25°C	0.10±0.05	2.52±1.29	0.62±0.08	2.69±1.58	0.95±0.03	8
	32°C	0.14±0.07	3.54±1.77	0.68±0.09	3.32±2.48	0.95±0.01	7
	34°C	0.08±0.07	1.92±1.76	0.58±0.13	1.53±1.52	0.93±0.05	8
GFP-Dpp in shibire-rescue disks	25°C	0.12±0.09	3.05±2.32	0.60±0.17	2.58±2.04	0.91±0.05	11
	32°C	0.06±0.02	1.53±0.58	0.61±0.09	1.11±0.44	0.94±0.03	7
GFP-Dpp measured in modified geometries at 25°C	20 $\mu\text{m}$ wide	0.12±0.10	3.01±2.52	0.61±0.18	2.03±2.14	0.95±0.05	3
	20 $\mu\text{m}$ away	0.07±0.05	1.55±1.20	0.35±0.03	5.18±0.34	0.95±0.03	2
	perpendicular FRAP	0.04±0.03	1.40±1.40	0.61±0.26	4.24±3.18	0.97±0.02	3
	30 $\mu\text{m}$ square	0.11±0.05	2.86±1.32	0.62±0.16	6.30±1.57	0.95±0.01	2

Table 3.1: Summary of the kinetic parameters  $D$ ,  $k$ ,  $\nu$  and  $\psi$  determined in the FRAP experiments. The kinetic parameters are displayed for the different experimental setups which are described in the column “experiment description”. For all values the mean and the standard deviation are reported. The correlation coefficient  $R^2$  describes the quality of the fits, and  $n$  is the number of realizations of the different experiments. Table modified from [55].

In summary, our analysis of the FRAP experiments in the *Drosophila* wing disk at a late stage of development has shown that Dpp transport is dominated by intracellular trafficking. We measured the kinetic parameters which describe Dpp spreading, namely the diffusion coefficient, the degradation rate, the production rate, and the immobile fraction. And finally, we have shown that these parameters can be considered as independent of position in the disk.

## 3.2 Dpp transport in the growing wing disk

In the preceding section 3.1, we have been concerned with the kinetics of the Dpp gradient in the wing disk at a late stage of development when growth slows down (see Fig. A.1). In this section, we consider the question how the transport of Dpp molecules is modified by tissue growth.

### 3.2.1 Transport equation

Similar to descriptions of moving fluids (see e.g. [62]), we define the derivative  $dc/dt$  as the rate of change of the Dpp concentration of a cell as it moves through space with velocity  $\mathbf{v}$ . In contrast,  $\partial c/\partial t$  denotes the rate of change of the concentration at a fixed position in space. The change  $dc$  of the concentration of a moving cell during the time interval  $dt$  has two contributions, namely the change of the concentration at fixed position  $\mathbf{r}$  during  $dt$ , and the difference in the concentrations at fixed time  $t$  at two

positions  $d\mathbf{r}$  apart, which is the distance moved by the cell during the time interval  $dt$ . We can thus write  $dc(\mathbf{r}, t) = \frac{\partial c}{\partial t} dt + \frac{\partial c}{\partial x} dx + \frac{\partial c}{\partial y} dy$ . Therefore, the rate of change of the concentration of a moving cell is described by the convective derivative

$$\frac{dc}{dt} = \frac{\partial c}{\partial t} + (\mathbf{v} \cdot \nabla)c. \quad (3.5)$$

As the cells move through space, they carry Dpp molecules with themselves and exchange them by diffusion. Therefore, the rate of change  $dc/dt$  of the Dpp concentration of a moving cell is determined by diffusion, degradation and production as in the static case. But since the tissue grows in area, the concentration  $c = \delta N/\delta A$ , where  $\delta N$  is the number of Dpp molecules in a small area element  $\delta A$ , is moreover diluted. The rate of change of the concentration of moving cells is hence given by

$$\frac{dc}{dt} = \frac{\frac{d}{dt}(\delta N)}{\delta A} - \frac{\delta N}{(\delta A)^2} \frac{d}{dt}(\delta A). \quad (3.6)$$

The first term describes Dpp transport for moving cells at time  $t$  in the area element  $\delta A$ , which is given by the transport equation (3.1). The second term describes the dilution of Dpp molecules caused by tissue growth. Using  $\delta A = \delta x \delta y$ , it follows that  $\frac{d(\delta A)}{dt}/\delta A = \frac{d(\delta x)}{dt}/\delta x + \frac{d(\delta y)}{dt}/\delta y = \delta v_x/\delta x + \delta v_y/\delta y = \nabla \cdot \mathbf{v}$ , and thus  $\frac{\delta N}{(\delta A)^2} \frac{d}{dt}(\delta A) = c(\nabla \cdot \mathbf{v})$ . Hence we can finally write down the Dpp transport equation in the growing wing disk at fixed position  $\mathbf{r}$  in space,

$$\partial_t c(\mathbf{r}, t) = \nabla \cdot (D(t)\nabla c(\mathbf{r}, t) - \mathbf{v}c(\mathbf{r}, t)) - k(t)c(\mathbf{r}, t) + \nu(t)\Theta(-x)\Theta(x + w(t)). \quad (3.7)$$

Compared to the Dpp transport equation (3.1) in disks at a late stage of development, when effects due to tissue growth are negligible, Eq. (3.7) contains the additional drift term  $-\nabla \cdot (\mathbf{v}c)$ , which describes the dilution and stretching of the concentration profile. Moreover, the parameters  $D$ ,  $k$ ,  $\nu$  and  $w$  are now functions of time. In principle,  $D$  and  $k$  can also depend on position [17], but our data indicates that at least at the end of development this is not the case, see section 3.1.3. Therefore, for simplicity, we assume position independence of  $D$  and  $k$  throughout development. For a transformation of this equation into a growing coordinate system of the proliferating and moving cells see appendix B.1.

As a result of the symmetry of Dpp spreading in the wing disk discussed in section 3.1.1, the Dpp concentration obeys  $c(\mathbf{r}, t) \approx c(x, t)$ . Inserting Eq. (2.7) for the cell velocity with the time dependent growth rates  $k_x = k_0 + k_1$  and  $k_y = k_0 - k_1$  in  $x$ - and  $y$ -direction, respectively, Dpp transport in the growing disk can thus be described by the one dimensional equation

$$\partial_t c(x, t) = D(t)\partial_x^2 c(x, t) - k_x(t)x\partial_x c(x, t) - (k(t) + k_g(t))c(x, t) + \nu(t)\Theta(-x)\Theta(x + w(t)), \quad (3.8)$$

where we used  $k_x + k_y = k_g$  (see section 2.1.3), i.e. we neglect apoptosis which is small during wing disk development. The term  $-k_x(t)x\partial_x c(x, t)$  describes the stretching of the gradient, and  $-k_g(t)c(x, t)$  accounts for the dilution of the concentration due to growth.

### 3.2.2 Steady-state gradient in the growing disk

We now consider the question whether Dpp spreading in the growing wing disk can cause a stationary concentration profile. To answer this question, we have to check whether the 1d diffusion equation (3.8) with drift terms has a steady-state solution, given that the parameters  $D$ ,  $k$ ,  $\nu$ ,  $w$ ,  $k_x$  and  $k_g$  are fixed. Therefore, we consider the equation

$$D\partial_x^2 c(x) - k_x x \partial_x c(x) - (k + k_g)c(x) + \nu\Theta(-x)\Theta(x+w) = 0. \quad (3.9)$$

As boundary conditions, we impose the same conditions as for the situation without growth discussed in section 3.1.1. In appendix B.2, we show how Eq. (3.9) can be solved analytically. Hence a steady-state gradient forms in the growing wing disk, which is given by

$$c(x) = \begin{cases} C_1 Q\left(\frac{k+k_g}{2k_x}, \frac{1}{2}, \frac{k_x}{2D}|x|^2\right) & x \leq -w \\ C_2 Q\left(\frac{k+k_g}{2k_x}, \frac{1}{2}, \frac{k_x}{2D}x^2\right) + \frac{\nu}{k+k_g} \left(1 - qx F\left(\frac{k+k_g}{2k_x} + \frac{1}{2}, \frac{3}{2}, \frac{k_x}{2D}x^2\right)\right) & -w \leq x \leq 0. \\ C_3 Q\left(\frac{k+k_g}{2k_x}, \frac{1}{2}, \frac{k_x}{2D}x^2\right) & x \geq 0 \end{cases} \quad (3.10)$$

Here  $F(a, b, z) \equiv {}_1F_1(a, b, z)$  is the confluent hypergeometric function, see e.g. [2],  $Q(a, b, z) = F(a, b, z) - z^{1-b} \frac{\Gamma(1+a-b)\Gamma(b)}{\Gamma(a)\Gamma(2-b)} F(1+a-b, 2-b, z)$ , and  $q$  is defined as  $q = \sqrt{2k_x/D} \Gamma\left(\frac{k+k_g}{2k_x} + \frac{1}{2}\right) / \Gamma\left(\frac{k+k_g}{2k_x}\right)$ . The explicit expressions for the constants  $C_1$ ,  $C_2$  and  $C_3$ , which are rather involved functions of the parameters  $D$ ,  $k$ ,  $\nu$ ,  $w$ ,  $k_x$  and  $k_g$ , can be found in appendix B.2.

### 3.2.3 Impacts of growth on the Dpp gradient

We compare the stationary Dpp gradient (3.10) in the growing wing disk with the exponentially decaying concentration profile (3.3) in which growth effects are neglected. In Fig. 3.3, we have plotted Dpp gradients in steady state for the static and growing situation. For the parameters  $D$ ,  $k$ ,  $\nu$  and  $w$ , we chose typical values obtained by our FRAP analysis given in the figure caption. For the growth rates, we chose  $k_g = 2k_x$  for simplicity and  $k_x/k = 0.01, 0.1, 1.0$ . For the smallest growth rate  $k_x/k = 0.01$ , we find that dilution and stretching of the concentration profile are negligible as expected. Since  $Q(a, 1/2, z/a) \propto \exp(-2\sqrt{z})$  and  $\sqrt{z}F(a, 3/2, z/a) \propto \sinh(2\sqrt{z})$  for  $a \rightarrow \infty$ , one can show analytically that expression (3.10) approaches the exponential concentration profile (3.3) for  $k_x, k_g \rightarrow 0$ . For  $k_x/k = 0.1$ , which is an upper limit for the growth rate during wing disk development (see section 3.3.1), the difference between the gradients in the growing and non-growing situation still is rather small. However, for the large growth rate  $k_x/k = 1.0$ , the drift terms significantly change the gradient.

In Fig. 3.3, several impacts of growth become apparent. With increasing growth rate, the amplitude of the gradient decreases, which results from dilution. Moreover, the asymptotic decay of the concentration slows down since the gradient is stretched. For  $x \rightarrow \pm\infty$ ,  $Q(a, b, c|x|^2) \propto |x|^{-2a}(1+O(|x|^{-2}))$ , and thus the Dpp concentration (3.10) in a



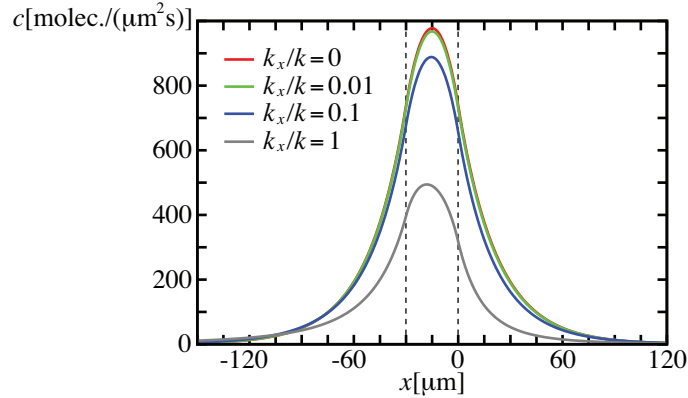


Figure 3.3: Dpp concentration profiles in steady state for four different growth rates  $k_x$ . The concentration  $c$  in units of molecules/ $(\mu\text{m}^2\text{s})$  is given by Eqs. (3.3) for  $k_x = 0$  and (3.10) otherwise. For the parameters, we chose the typical values  $D = 0.1 \mu\text{m}^2/\text{s}$ ,  $k = 2 \cdot 10^{-4} \text{s}^{-1}$ ,  $\nu = 0.4 \text{ molecules}/(\mu\text{m}^2\text{s})$ ,  $w = 30 \mu\text{m}$ , and  $k_g = 2k_x$  (see section 3.1). The dashed lines indicate the boundaries of the Dpp source located at  $x = 0$  and  $x = -w$ .

growing disk shows the power-law decay  $|x|^{-\frac{k+k_g}{k_x}}$  instead of the exponential decay of the concentration (3.3) in the non-growing situation. And finally, we observe an asymmetry of the Dpp gradient in respect to the center of the Dpp source. This asymmetry is revealed by a coordinate transformation of the transport equation (3.8) into the system  $\tilde{S}$  of fixed center of the source, defined by  $\tilde{x} = x + w(t)/2$  and  $\tilde{c}(\tilde{x}, t) = c(x, t)$ . In  $\tilde{S}$ , Dpp transport is described by

$$\partial_t \tilde{c} = D \partial_{\tilde{x}}^2 \tilde{c} - (k_x \tilde{x} - v_0) \partial_{\tilde{x}} \tilde{c} - (k + k_g) \tilde{c} + \nu \Theta\left(\frac{w(t)}{2} - \tilde{x}\right) \Theta\left(\tilde{x} + \frac{w(t)}{2}\right), \quad (3.11)$$

where  $v_0 = k_x w(t)/2 - \dot{w}(t)/2$ . If the source grew as fast as the tissue, i.e. if  $\dot{w}(t)/2 = k_x w(t)/2$ ,  $v_0$  would be zero and Eq. (3.11) would be symmetric. However, the Dpp source grows much slower during development than the disk (see section 3.3.1) so that  $v_0 > 0$ . This is also the case for our calculation of the Dpp concentration (3.10) in steady state, where we have considered fixed parameter values and thus  $\dot{w} = 0$ . Therefore the stretching term  $-(k_x \tilde{x} - v_0) \partial_{\tilde{x}} \tilde{c}$  becomes asymmetric. At a position  $a > 0$ , the increase of the Dpp concentration due to the stretching of the gradient is smaller than at  $-a$ , and thus  $\tilde{c}(a) < \tilde{c}(-a)$ .

The intrinsic reason for the symmetry breaking in the Dpp concentration profile in a growing disk is that the boundary of the Dpp source at  $x = 0$  moves in accordance with the cells at the AP boundary, whereas the boundary at  $x = -w(t)$  and the center of the source at  $x = -w(t)/2$  do not move together with the cells. At the boundary  $x = -w(t)$ , Dpp producing cells can move out of the source and stop their production

since Dpp production is regulated by the external signal of the morphogen Hedgehog [11], see section 1.1.

We can summarize that in growing tissues, where morphogen gradients are diluted and stretched due to the cell movements, the concentration profiles become stationary in space if parameters are fixed. As in the case of the cell trajectories (2.8) in the  $xy$ -plane, growth produces a power law for the decay of the Dpp concentration profile. Since the tissue grows faster than the width of the source and since the boundary at  $x = 0$  of the Dpp source moves in accordance with the cells, the symmetry of the Dpp gradient in respect to the center of the source is broken.

### 3.3 The Dpp gradient during development

So far, we have considered Dpp transport for the constant parameters  $D$ ,  $k$ ,  $\nu$ ,  $w$ ,  $k_x$  and  $k_g$ . What happens if these parameters change during development? The relaxation time for the steady state of the diffusion equation with degradation term is determined by  $\tau = k^{-1}$ . For the typical value  $k = 2 \cdot 10^{-4} \text{s}^{-1}$ , the time it takes for the Dpp gradient to relax to the steady state is thus given by  $\tau = 1.4 \text{h}$ . So if the parameters of the system vary slowly compared to the relaxation time  $\tau$ , the gradient will change adiabatically during development. In this case, the Dpp concentration profile can be described as a succession of steady-state gradients during development.

With this adiabatic approximation, we analyze in section 3.3.1 Dpp gradients which have been measured at different stages during development, and we determine the parameters  $D(t)$ ,  $k(t)$ ,  $\nu(t)$ ,  $w(t)$ ,  $k_x(t)$  and  $k_g(t)$  for the whole wing disk development. In section 3.3.2 we use these parameters to numerically calculate the full dynamics of Dpp spreading during development, including the drift of molecules due to growth and boundary effects, and compare it to the gradients which were calculated with the adiabatic approximation. We show that the system indeed changes adiabatically, which ensures the consistency of our analysis.

#### 3.3.1 Kinetic parameters of Dpp spreading during development

In order to calculate the full dynamics of Dpp spreading during development, we need to know the following parameters as functions of time: the diffusion coefficient, the degradation rate, the production rate, the width of the Dpp source, the growth rate along the  $x$ -axis, and the area growth rate.

First, the total area of GFP-Dpp disks was measured as a function of larval age, see Fig. A.1, B. We fit the function  $A_{\text{tot}}(t) = A_{\text{tot}}^{(0)} \exp(a_A t^{q_A} / (\tau_A^{q_A} + t^{q_A}))$  to the data, using  $a_A$ ,  $\tau_A$  and  $q_A$  as fit parameters. The initial disk area  $A_0$  can be estimated by  $A_{\text{tot}}^{(0)} = 250 \mu\text{m}^2$  by analyzing pictures of wing disks at this early stage [16]. The optimized values for the parameters  $a_A$ ,  $\tau_A$  and  $q_A$  are displayed in Table 3.2. For the analysis of the following experiments, we use this fit to calibrate the total area of a disk to the age of the larva. By that, we could simplify the experimental procedure since the disk area

is much easier to measure than keeping track of the larval age. From now on, we want to use the calibrated age synonymously for the larval age.

Fig. 3.4 shows measurements performed by O. Wartlick for our analysis of the GFP-Dpp gradient during development. First of all, Fig. 3.4, A shows the width  $w$  of the GFP-Dpp source as a function of larval age, which was measured by in situ hybridization. In these experiments, a synthetic digoxigenin-labeled RNA probe hybridizes to the complementary RNA of Dpp in the wing disk. The hybridized probe can be detected, thus allowing the visualization of Dpp and GFP-Dpp RNA in the source cells.

Next, Fig. 3.4, B and C show the concentration  $C_0$  next to the source and the decay length  $\lambda$  as functions of larval age, respectively. These quantities are obtained by fitting the steady-state gradient (3.3) for  $x > 0$  to GFP-Dpp gradients, using the calibration of fluorescence intensity to GFP concentration shown in Fig. 3.1. In contrast to the analysis in section 3.1.2, these fits are now done in disks of different ages. By fitting the exponentially decaying concentration profiles (3.3) to the gradients during development, we consider the Dpp gradients to be in steady state for the current values of the kinetic parameters. In addition to this adiabatic approximation, we consider the kinetic parameters  $D$ ,  $k$ ,  $\nu$ ,  $w$ ,  $k_x$  and  $k_g$  of the gradients to be in a regime where the growth effects of stretching and dilution are negligibly small as discussed in section 3.2.3. These considerations will be confirmed in section 3.3.2, showing the consistency of our data analysis. Finally, Fig. 3.4, D and E show the length  $l$  of the posterior compartment (measured at its widest point) and its area  $A_P$ , respectively, plotted logarithmically as functions of larval age.

We fit the following functions to the five sets of data in Fig 3.4:

$$\begin{aligned}
 w(t) &= w_f - a_w e^{-t/\tau_w} , \\
 \lambda(t) &= \lambda_i + (\lambda_f - \lambda_i) \frac{(t - t_i)^{q_\lambda}}{\tau_\lambda^{q_\lambda} + (t - t_i)^{q_\lambda}} , \\
 C_0(t) &= C_0^{(f)} \frac{(t - t_i)^{q_c}}{\tau_c^{q_c} + (t - t_i)^{q_c}} , \\
 l(t) &= l_0 \exp \left( a_l (1 - e^{-(t-t_i)/\tau_g}) \right) , \\
 A_P(t) &= A_P^{(0)} \exp \left( a_P (1 - e^{-(t-t_i)/\tau_g}) \right) .
 \end{aligned} \tag{3.12}$$

Here  $w_f$ ,  $a_w$ , and  $\tau_w$  are the fit parameters for the width  $w(t)$  of the source,  $t_i = \tau_w \ln(a_w/w_f)$  is the time when the source starts to grow, i.e.  $w(t_i) = 0$ ,  $\lambda_i$ ,  $\lambda_f$ ,  $\tau_\lambda$ , and  $q_\lambda$  are the fit parameters for the decay length  $\lambda(t)$ ,  $C_0^{(f)}$ ,  $\tau_c$ , and  $q_c$  are the fit parameters for the concentration  $C_0$  at  $x = 0$ ,  $l_0$ ,  $a_l$ , and  $\tau_g$  are the fit parameters for the length  $l(t)$  of the P compartment at its widest point, and  $A_P^{(0)}$ ,  $a_P$ , and  $\tau_g$  are the fit parameters for the area  $A_P$  of the P compartment. The Eqs. (3.12) define the functions  $w(t)$ ,  $\lambda(t)$ ,  $C_0(t)$ ,  $l(t)$ , and  $A(t)$  for the times  $t \geq t_i$ . Since Dpp production sets in at time  $t_i$ , we define  $w(t) = 0$  for  $t < t_i$ ,  $C_0(t) = 0$  for  $t < t_i$ , and  $\lambda(t) = \lambda_i$  for  $t < t_i$ . Moreover, we define  $l(t) = l_0$  for  $t < t_i$ , and  $A_P(t) = A_P^{(0)}$  for  $t < t_i$ . The functions  $w(t)$ ,  $\lambda(t)$ , and  $C_0(t)$  were fitted directly to the data, whereas  $l(t)$  and  $A(t)$  were fitted logarithmically

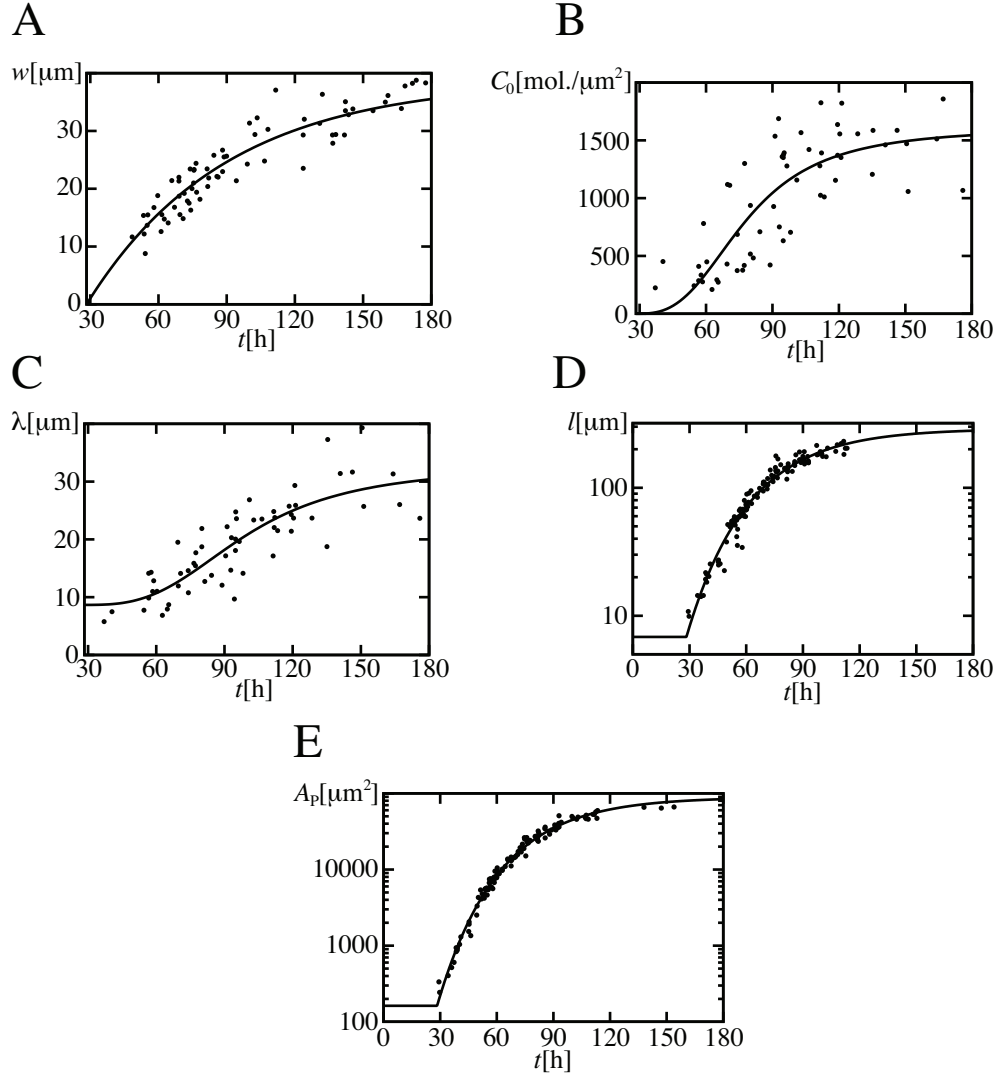


Figure 3.4: Key quantities of GFP-Dpp spreading in the *Drosophila* wing disk during development. (A) Width of the Dpp source as a function of larval age. (B) GFP-Dpp concentration next to the source as a function of larval age. (C) Decay length of the GFP-Dpp gradient as a function of larval age. (D) Length of the posterior compartment of the wing disk at its widest point as a function of larval age. (E) Area of the posterior compartment as a function of larval age. The solid lines represent fits of the Eqs. (3.12) to the data, the best fit parameters are given in Table 3.2. Experimental procedures are described in the text.

quantity	values of the optimized fit parameters
$A_{\text{tot}}(t)$	$a_A = 6.91 \pm 0.13$ , $\tau_A = 46.5 \pm 0.9$ h, $q_A = 2.67 \pm 0.13$
$w(t)$	$w_f = 38.8 \pm 2.1$ $\mu\text{m}$ , $a_w = 61.7 \pm 8.0$ , $\tau_w = 61.1 \pm 11.9$ h $\implies t_i = 28.4 \pm 10.2$ h
$\lambda(t)$	$\lambda_i = 8.7 \pm 2.2$ $\mu\text{m}$ , $\lambda_f = 32.7 \pm 3.0$ $\mu\text{m}$ , $\tau_\lambda = 71.2 \pm 7.7$ h, $q_\lambda = 2.9 \pm 0.9$
$C_0(t)$	$C_0^{(f)} = 1608 \pm 137$ molec./ $\mu\text{m}^2$ , $\tau_c = 49.6 \pm 4.4$ h, $q_c = 2.8 \pm 0.6$
$l(t)$	$l_0 = 6.8 \pm 0.5$ $\mu\text{m}$ , $a_l = 3.74 \pm 0.07$ , $\tau_g = 32.3 \pm 0.9$ h
$A_P(t)$	$A_P^{(0)} = 162 \pm 11$ $\mu\text{m}^2$ , $a_P = 6.30 \pm 0.06$

Table 3.2: Best fit parameters of the key quantities describing GFP-Dpp transport in the wing disk. The total area  $A_{\text{tot}}$  of GFP-Dpp disks as a function of larval age is shown in Fig. A.1, B, the corresponding fit function is given in the text. All other quantities are shown in Fig. 3.4, and the functions fitted to these data are given in Eqs. (3.12). For all quantities, the best fit parameters and standard errors obtained by least square fits to the measured data are displayed.

and simultaneously to the data since the fit parameter  $\tau_g$  appears in both functions. The values of the optimized fit parameters are displayed in Table 3.2. Note that the values of the parameters  $l_0$  and  $A_P^{(0)}$  are consistent with the constraints  $a < l_0 < (A_{\text{tot}}^{(0)}/\pi)^{1/2}$  and  $A_{\text{tot}}^{(0)}/4 < A_P^{(0)} < A_{\text{tot}}^{(0)}$ , respectively, where  $a = 2.6$   $\mu\text{m}$  is the average cell diameter.

We have chosen the definitions (3.12) for the fit functions since they describe the principal distribution of the data points shown in Fig. 3.4:  $w(t)$  describes a growth of the source which slows down and finally saturates at the width  $w(t \gg \tau_w) \rightarrow w_f$ ,  $\lambda(t)$  specifies a smooth transition between the decay lengths  $\lambda(t_i) = \lambda_i$  and  $\lambda(t \gg t_i) \rightarrow \lambda_f$ ,  $C_0(t)$  yields a smooth increase from  $C_0(t_i) = 0$  to  $C_0(t \gg t_i) \rightarrow C_0^{(f)}$ , and  $l(t)$  and  $A_P(t)$  describe a slowed down growth of the initial length  $l_0$  and initial area  $A_P^{(0)}$  which sets in at time  $t = t_i$  and saturates at  $l(t \gg t_i + \tau_g) \rightarrow l_0 e^{a_l}$  and  $A_P(t \gg t_i + \tau_g) \rightarrow A_P^{(0)} e^{a_P}$ , respectively. Of course, different fit functions can be chosen, but except for times  $t \approx t_i$  the further analysis does not depend sensitively on the exact choice of these functions. Our definitions (3.12) are motivated by the fact that Dpp is needed for growth [30], which will be discussed in detail in section 3.4. Therefore, we chose the functions  $l(t)$  and  $A_P(t)$  such that the onset of the growth of the disk coincides with the onset of Dpp production. Moreover, we chose the same time scale  $\tau_g$  for  $l(t)$  and  $A_P(t)$ , because when the growth of the disk slows down, it will affect both the growth in length and area. Naturally, the concentration  $C_0$  is zero before Dpp is produced.

The fits describe the data very well, see Fig. 3.4. They can be used to determine the kinetic parameters needed for our analysis of Dpp spreading during development which is focused on the posterior compartment and the Dpp source. The growth rates can thus be determined by  $k_x(t) = \dot{l}(t)/l(t)$  and  $k_g(t) = \dot{A}_P(t)/A_P(t)$ . At times  $t < t_i$  both  $k_x$

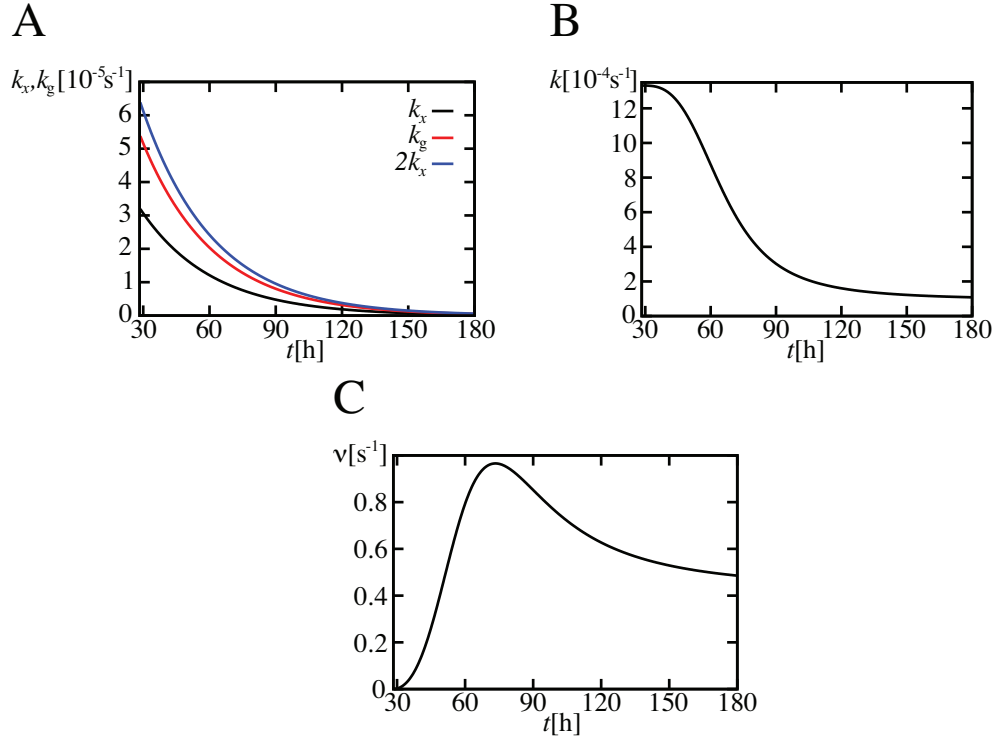


Figure 3.5: Kinetic parameters of GFP-Dpp transport in the wing disk. (A) Growth rates as functions of larval age. The growth rate  $k_x = \dot{l}/l$  characterizing the growth of the length  $l$  of the posterior compartment is compared to the area growth rate  $k_g = \dot{A}_P/A_P$  of the posterior compartment of the disk. The length and area of the posterior compartment as functions of larval age are taken from the fits to the measured data shown in Fig. 3.4, D and E. (B) Degradation rate of GFP-Dpp molecules as a function of larval age. Using the fitted decay length as a function of larval age plotted in Fig. 3.4, C, and considering a constant diffusion coefficient, for which we use the value  $D = 0.1 \mu\text{m}^2/\text{s}$  obtained in FRAP experiments, the degradation rate is determined by  $k(t) = D/\lambda(t)^2$ . (C) Production rate of GFP-Dpp molecules as a function of larval age. The production rate is calculated by  $\nu(t) = 2k(t)C_0(t)[1 - \exp(-w(t)/\lambda(t))]^{-1}$ , where we use  $k(t)$  from B, the fitted concentration  $C_0(t)$  next to the source shown in Fig. 3.4, B, the fitted width  $w(t)$  of the source plotted in Fig. 3.4, A, and the fitted decay length  $\lambda(t)$  shown in Fig. 3.4, C.

and  $k_g$  vanish. With the onset of GFP-Dpp production, the growth rate is maximal and decreases monotonously during development, see Fig. 3.5, A. We find that the growth rate  $k_x$  in  $x$ -direction is slightly bigger than  $k_g/2$  throughout development, reflecting that growth is anisotropic as discussed in chapter 2.

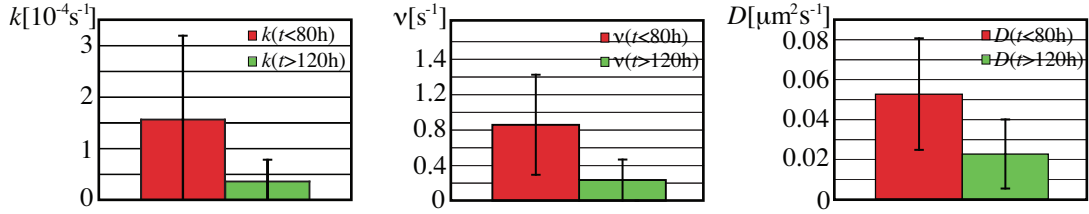


Figure 3.6: Kinetic parameters of GFP-Dpp spreading obtained in FRAP experiments at different stages during development. The mean and standard deviation of the parameters  $k$ ,  $\nu$  and  $D$  are shown for disks younger than 80 h and older than 120 h. The experiments were done in  $n = 9$  disks of an age between 60 h and 80 h with average  $(66 \pm 8)$  h, and in  $n = 6$  disks of an age between 120 h and 180 h with average  $(147 \pm 18)$  h.

Since  $w(t)$  is measured directly, the remaining parameters which need to be determined for our analysis of Dpp transport in the growing wing disk are  $D(t)$ ,  $k(t)$  and  $\nu(t)$ . For that, the measurements of  $\lambda = \sqrt{D/k}$  and  $C_0 = \frac{\nu}{2k} (1 - \exp(-\frac{w}{\lambda}))$  are not yet sufficient. Therefore, FRAP experiments were performed by A. Kicheva [56] in wing disks at different stages during development (see section 3.1.2 for a detailed description of these experiments and their analysis). The optimized parameters  $D$ ,  $k$  and  $\nu$  are displayed in Fig. 3.6, in which the average values of  $D$ ,  $k$  and  $\nu$  in disks younger than 80 h are compared to the average values in disks older than 120 h. We find that from young to old disks the degradation rate and the production rate decrease by a factor of about five and four, respectively, whereas the diffusion coefficient only decreases by a factor of about two. Hence, the data indicates that  $k$  and  $\nu$  change stronger during development than  $D$ . For our further analysis, we therefore consider a scenario in which  $D$  stays constant during development while  $k$  and  $\nu$  change. For the diffusion coefficient, we use the value  $D = 0.1 \mu\text{ m}^2/\text{ s}$  obtained in the FRAP experiments in intermediate disks [55], see section 3.1.2. So now, we can determine  $k(t)$  from the fits of  $\lambda(t)$ , and finally we get  $\nu(t)$  from the fits of  $C_0(t)$ . The functions obtained for  $k(t)$  and  $\nu(t)$  are plotted in Fig. 3.5, B and C. Consistently with our observations in the FRAP experiments, the degradation rate decreases with increasing age of the flies. Furthermore, the production rate for disks of an age between 60 and 80 h is increased compared to the the production rate for disks older than 120 h. And naturally,  $\nu$  increases with the onset of Dpp production at time  $t_i$ , starting from  $\nu(t_i) = 0$ .

### 3.3.2 Evolution of the Dpp concentration profile

We now use the parameters  $D(t)$ ,  $k(t)$ ,  $\nu(t)$ ,  $w(t)$ ,  $k_x(t)$  and  $k_g(t)$  to analyze the full dynamics of Dpp transport in the growing wing disk, including the effects of growth and the non-adiabaticness of the system. We calculate the evolution of the Dpp concentration profile during development by solving the diffusion-advection equation (3.8) numerically, considering the finite length of the disk. As boundary conditions, we impose a vanishing

flux  $j = -D\partial_x c + k_x c$  at the center of the source and at the tissue boundary.

Fig. 3.7, A to D shows the numerically calculated Dpp concentration profiles, which take the full dynamics and boundary effects into account, at different stages during development in comparison with the steady-state gradients (3.3) and (3.10) in the adiabatic approximation. The concentration profiles are plotted from the center of the source at  $x = -w(t)/2$  to the boundary of the tissue at  $x = l(t)$ . We find that the steady-state gradients in the adiabatic approximation match the numerically calculated concentration profiles very well. Moreover, there is hardly any difference between the steady-state gradients with and without drift terms. The effects of the finite tissue size are only apparent for very young disks (see Fig. 3.7, A), when the decay length of the gradient is comparable with the size of the tissue (see Fig. 3.4, C and D), but even then these effects are small.

We can thus conclude that the drift terms of stretching and dilution (see section 3.2) which result from tissue growth have no significant effect on the Dpp gradient throughout wing disk development. Indeed, one can show that for the parameters determined in section 3.3.1  $-k_x(t)x\partial_x c(x,t) \ll D(t)\partial_x^2 c(x,t)$  and  $k_g(t) \ll k(t)$  for all times during development and for all positions within the tissue. Furthermore, the parameters  $D(t)$ ,  $k(t)$ ,  $\nu(t)$ ,  $w(t)$ ,  $k_x(t)$  and  $k_g(t)$  of Dpp spreading change so slowly during development compared to the time scale on which the Dpp gradient relaxes to its steady state that the concentration profile can be considered to be in steady state for all times. This has also been validated for situations in which the diffusion coefficient changes in addition to the degradation and production rate in accordance with the experimental results.

In summary, the Dpp gradient in the receiving tissue can thus be described by the exponentially decaying concentration profile (3.3) throughout development. Thus the Dpp gradient, which is plotted in Fig. 3.7, E for the full disk development, only depends on the decay length  $\lambda(t)$ , on the concentration  $C_0(t)$  at the AP boundary, and on the width  $w(t)$  of the source which are robustly measured quantities (see Fig. 3.4, A to C). Our data analysis in section 3.3.1, in which we used the steady-state gradients (3.3) to determine the values of the kinetic parameters during development, is thus consistent.

Moreover, the common idea that growth leads to a stretching of the Dpp gradient and thus to an increase in the decay length (see e.g. [30]) can be excluded from our analysis. Indeed, the decay length of the Dpp gradient increases during development, but this increase results from a decrease of the degradation rate and is not an effect of tissue growth.

### 3.3.3 Dpp concentration measured by moving cells

In the preceding section, we have shown that tissue growth does not affect the Dpp concentration profile in the developing wing disk. However, what we are actually interested in is the Dpp concentration that is measured by a cell as it moves in the growing tissue rather than the concentration at fixed positions in space. As the tissue grows, cells move along the trajectories  $x(t) = x_0 \exp\left(\int_{t_0}^t dt' k_x(t')\right)$ ,  $y(t) = y_0 \exp\left(\int_{t_0}^t dt' k_y(t')\right)$  with initial position  $(x_0, y_0)$  at time  $t_0$  (see section 2.1.3). The increasing tissue length in  $x$ -direction is described by  $l(t) = l_0 \exp\left(\int_{t_0}^t dt' k_x(t')\right)$ . Hence, a cell at the initial position



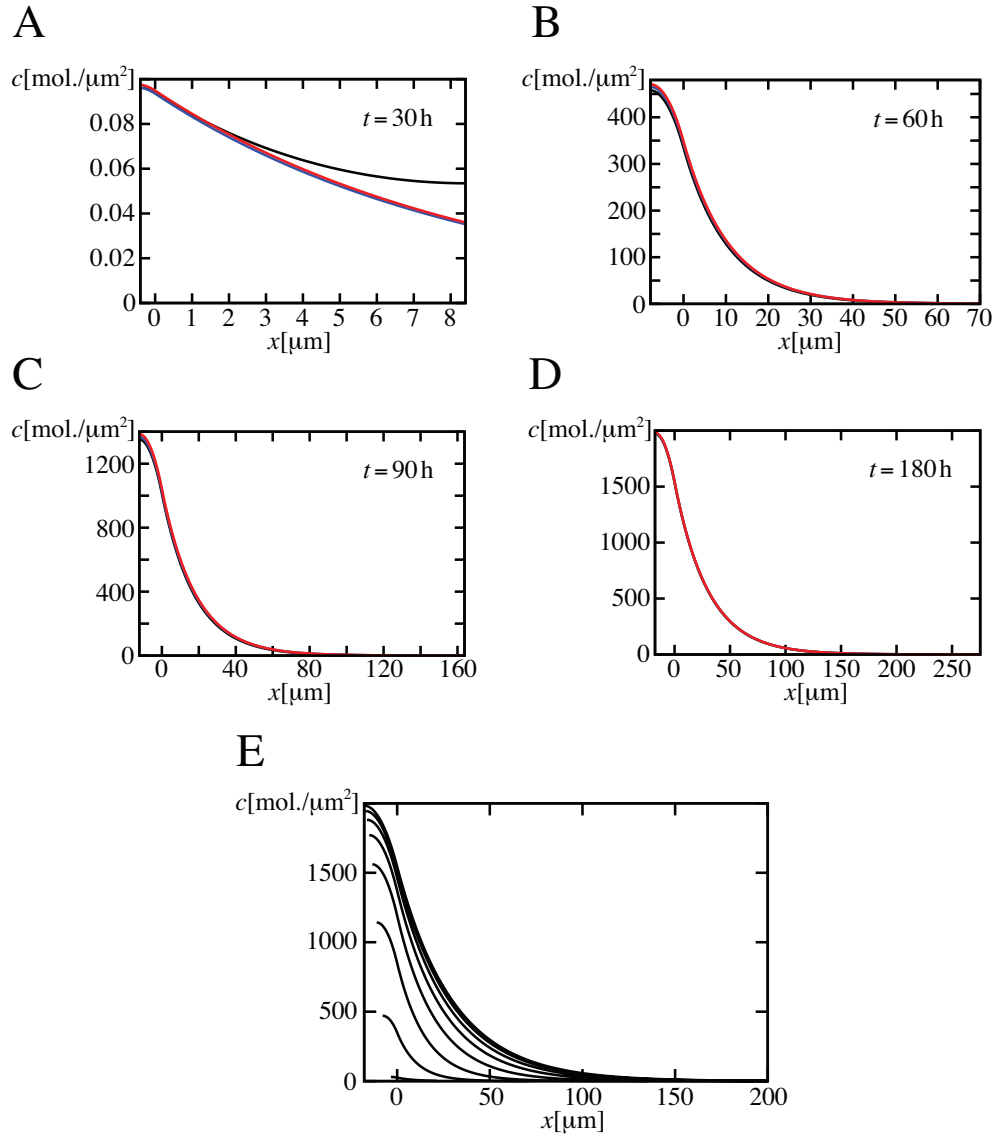


Figure 3.7: Dpp gradients during wing disk development. (A-D) Comparison of the full dynamics of Dpp spreading to steady-state gradients in the adiabatic approximation. The numerically calculated Dpp concentration profile, which takes the full dynamics during tissue growth and boundary effects into account, is plotted in black at 4 different larval ages. For comparison, the steady-state gradients with drift terms (see Eq. (3.10)) are plotted in blue, and those without drift terms (see Eq. (3.3)) are plotted in red. (E) Evolution of the Dpp gradient. The steady-state gradients (3.3) are plotted in the adiabatic approximation from  $t = 40$  h to  $t = 180$  h in steps of 20 hours. Each concentration profile is plotted from the center of the Dpp source  $x = -w(t)/2$  to the boundary of the posterior compartment  $x = l(t)$  (except for E where the plots are cut at  $x = 200 \mu\text{m}$ ). The AP boundary is fixed at  $x = 0$ .

$sl_0$  with  $s \in [0, 1]$  will move along the trajectory  $sl_0 \exp\left(\int_{t_0}^t dt' k_x(t')\right)$ , and thus it will always be located at the fraction  $sl(t)$  of the tissue length. Therefore, we define the Dpp concentration measured by a moving cell in the growing wing disk as

$$c_{\text{mov}}(s, t) = c(sl(t), t). \quad (3.13)$$

Since the spreading of Dpp molecules in the developing wing disk is well described by the adiabatically changing gradients (3.3), the cellular Dpp concentration is given by

$$c_{\text{mov}}(s, t) = C_0(t) \exp\left(\frac{-sl(t)}{\lambda(t)}\right). \quad (3.14)$$

The cellular Dpp concentration is thus determined by two opposing effects: On the one hand, the growth of the Dpp source leads to an increase in the concentration  $C_0$  and thus to an increase of the cellular concentration. But on the other hand, cells move away from the Dpp source as a result of tissue growth which leads to a decrease in the cellular concentration. Hence,  $c_{\text{mov}}$  strongly depends on the position of the cell in the disk since it determines which of these two processes dominates.

In Fig. 3.8,  $c_{\text{mov}}$  is plotted logarithmically as a function of disk age for the positions  $s = 0, 0.1, \dots, 1$ . Cells close to the source measure a monotonic increase of the Dpp concentration since they only move slowly away from the source so that the increase in  $C_0$  is dominant. However, cells closer to the tissue boundary only measure an increasing concentration at the early disk development when the disk is small. Later on, the concentration decreases since these cells move away from the source with a higher velocity than cells close to the source so that the concentration decrease as a result of an increasing distance to the source is dominant. When growth slows down, the Dpp concentration increases again in these cells as a result of the increasing decay length of the gradient. Note that the cellular concentration of the moving cells can be described by the diffusion equation (B.2) which results from a coordinate transformation into a growing system that moves in accordance with the cells, see appendix B.1.

While tissue growth has no significant effect on the Dpp concentration profile, it strongly affects the cellular concentration and thus the signaling process. The cellular concentration depends crucially on the position in the tissue. It is thus difficult to find rules for possible signaling mechanisms on the basis of the cellular Dpp concentration which are position independent, as in particular the regulation of cell division in which Dpp is involved. This will be the topic of the next section.

### 3.4 Possible roles of Dpp in growth control

In the previous sections, we have considered the question how the morphogen Dpp spreads in the growing wing disk of the fruit fly. In this section, we analyze how the cellular Dpp concentration is related to the tissue growth rate. From experiments, it is known that Dpp is needed for the growth of the disk which is approximately uniform, see section 1.2. However, it remains unclear how growth is regulated by Dpp [84, 30, 66, 3].

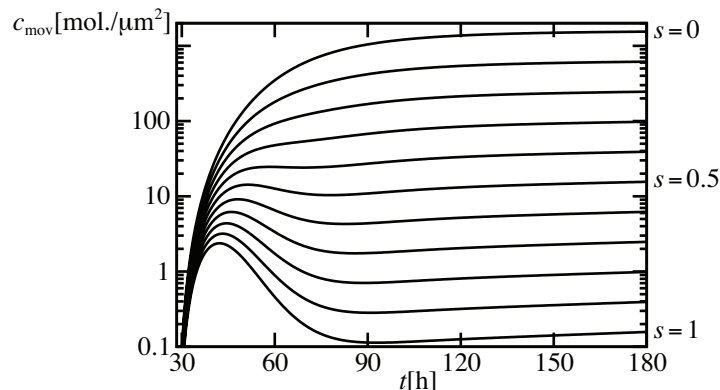


Figure 3.8: Cellular Dpp concentration during wing disk development. The concentration  $c_{\text{mov}}(s, t)$  measured by cells which move away from the Dpp source due to tissue growth is plotted logarithmically as a function of disk age. The cellular concentrations are displayed for 11 different cell trajectories  $x_s(t) = sl(t)$  with  $s = 0, 0.1, \dots, 1$ . Hence  $s = 0$  corresponds to a cell that always sits at the AP boundary and thus measures the concentration  $C_0$ , whereas  $s = 1$  corresponds to a cell that moves in accordance with the boundary of the tissue.

Since the cellular Dpp concentration depends strongly on position (see Fig. 3.8), its absolute value cannot control the growth rate. Several models have been proposed to solve this problem. It has been suggested that the local slope of the Dpp gradient regulates the growth rate [30, 81]. In this model, it is assumed that the steepness of the Dpp gradient decreases as a result of tissue growth, and that growth stops when the local slope falls below a certain threshold level. However, we have shown in section 3.3.2 that the Dpp gradient is not stretched by tissue growth, i.e. growth does not influence the steepness of the gradient. Moreover, there is experimental evidence that ubiquitous Dpp overexpression in the wing disk and thus a flat Dpp concentration profile leads to an increased growth [74] in contradiction to this model.

Another approach suggests that Dpp in combination with mechanical stresses regulates growth [52]. In this model, it is proposed that growth stops when the Dpp concentration in cells close to the boundary of the growing wing disk falls below a certain threshold value. In order to explain the position independence of the growth rate, Hufnagel et al. propose that the stop signal propagates to the interior of the disk by mechanical interactions between the cells [87]. However, we have shown that the concentration at the boundary of the disk reaches a minimal level long before growth stops (see Fig. 3.8). The increase of the concentration at the disk boundary at late stages of development results from the increase of the concentration  $C_0$  next to the source, the slowing down of growth and the increase of the decay length  $\lambda$  of the Dpp gradient (see section 3.3.1), which is not observed in [52] since there the gradients are only measured for the last 45 h of development.

In this section, we want to present possible rules by which Dpp could control growth in agreement with our data. Since Dpp is required for the growth of the wing disk, the growth rate  $k_g \approx 2k_x$  (we do not consider anisotropies of growth in this section) must be some function of the cellular Dpp concentration  $c_{\text{mov}}$  (3.14). As the growth rate is approximately homogeneous in space, our goal is to find a measure that depends on  $c_{\text{mov}}$  but is independent of position in the disk. In Fig. 3.9, A and B, we have plotted the time derivative of  $c_{\text{mov}}$  and the relative rate of change

$$\gamma(s, t) \equiv \dot{c}_{\text{mov}}(s, t)/c_{\text{mov}}(s, t) \quad (3.15)$$

of the cellular Dpp concentration, respectively, as functions of disk age for cells that move on the trajectories  $x_s(t) = sl(t)$  with  $s = 0, 0.1, \dots, 1$ . The absolute rate of change  $\dot{c}_{\text{mov}}$  of the cellular concentration still depends strongly on position. However, the relative rate of change  $\gamma(s, t)$  of the cellular Dpp concentration only shows a position dependence in young disks but is almost position independent for larvae which are older than 100 h. Fig. 3.9, C shows the relation between the growth rate  $2k_x(t)$  and the corresponding values of  $\gamma(s, t)$  at times  $t$  throughout development at different positions in the tissue. Large values of  $2k_x$  and  $\gamma$  correspond to early times, whereas  $2k_x \rightarrow 0$  at late developmental stages. At disk ages between 100 h and 180 h, the relation between  $2k_x(t)$  and the average  $\bar{\gamma}(t) = \frac{1}{N} \sum_{s=1}^N \gamma(s, t)$  is almost linear as plotted in Fig. 3.9, D. At these times, we can describe the relation between  $2k_x$  and  $\bar{\gamma}$  by the function  $2k_x = \alpha\bar{\gamma} + \beta$  with the optimized parameters  $\alpha = 4.07$  and  $\beta = -0.0067 \text{ h}^{-1}$ .

We can thus formulate a first possible rule for growth control by Dpp at a late stage of development: From the larval age  $t_{\text{on}} = 100$  h on, we define the growth rate at time  $t$  and position  $x$  within the tissue by  $k_g(x, t) \equiv 2k_x(t) = \alpha\gamma(x/l(t), t) + \beta$  for  $\gamma(x, t) > -\beta/\alpha$  and  $k_g(x, t) = 0$  otherwise, with  $\alpha = 4.07$  and  $\beta = -0.0067 \text{ h}^{-1}$ . Moreover, we propose that growth starts with the onset of Dpp production at time  $t_i = 28.4$  h (see Table 3.2), i.e.  $k_g = 0$  as long as the cellular Dpp concentration is zero. In appendix B.3, we discuss numerical simulations of the feedback between Dpp spreading, which is described by the diffusion-advection equation (3.8), and the growth rate, which is determined by the cellular Dpp concentration according to our rule. In these simulations, we can reproduce the measured length of the wing disk as a function of time, and we show that the growth rate becomes more and more position dependent if we start growth regulation at times before  $t_{\text{on}} = 100$  h.

Hence, this rule can explain the onset and stop of growth, but it has the drawback that it cannot explain how growth is regulated at early and medial developmental stages. Of course, it could be possible that Dpp regulates the growth rate as suggested by our rule at a late stage of development, whereas growth is controlled by a different mechanism at earlier times. But certainly, this is highly speculative. We were therefore looking for a different rule, by which the growth of the wing disk could be controlled by Dpp during the whole development. Since we could not find such a measure by studying simple functions of the cellular Dpp concentration, we analyzed the concentration profiles of phosphorylated Mad (P-Mad) molecules which mediate Dpp signaling in the wing disk (see Fig. 1.1). Experimental details are described in appendix B.4.

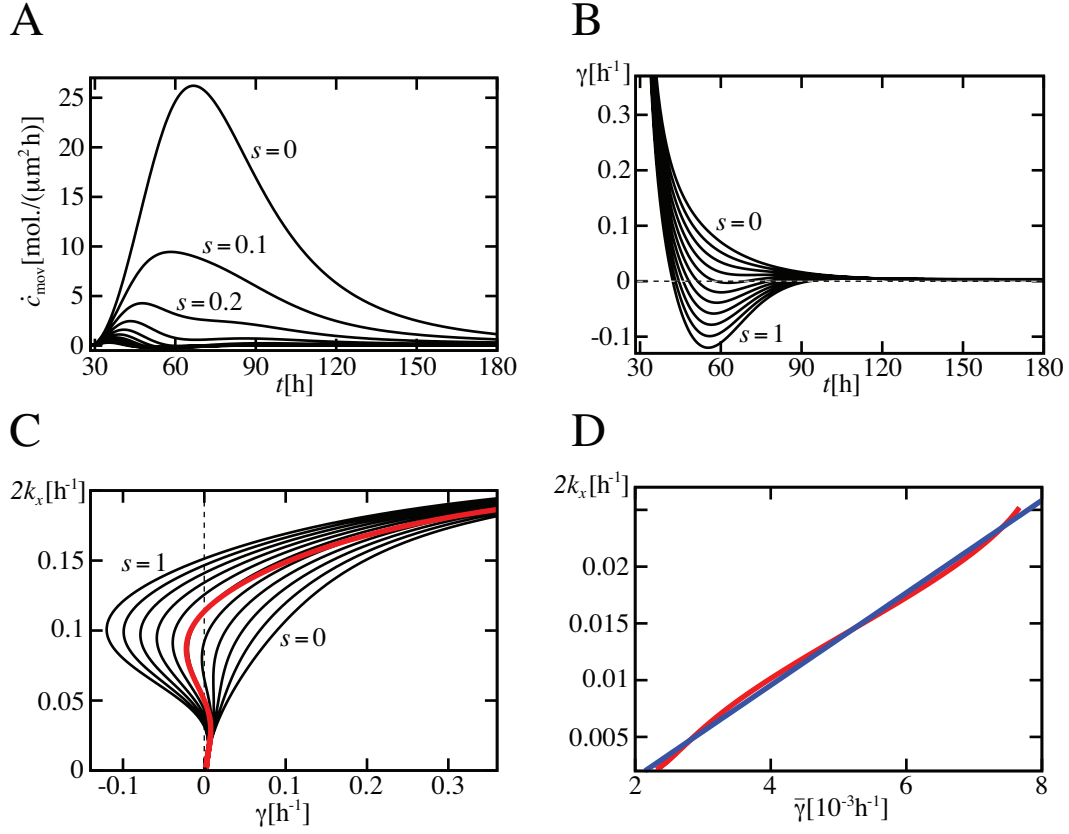


Figure 3.9: Change of the cellular Dpp concentration in time and its relation to the growth rate in the Drosophila wing disk. (A,B) The absolute rate of change  $\dot{c}_{\text{mov}}$  (A) and the relative rate of change  $\gamma$  of the cellular Dpp concentration (B) as functions of disk age for cells that move along the trajectories  $x_s(t) = sl(t)$  with  $s = 0, 0.1, \dots, 1$ . (C,D) Relation between the growth rate  $2k_x$  and the relative rate of change of the cellular Dpp concentration. (C) The values of  $2k_x(t)$  (given in Fig. 3.5, A) that correspond to the values of  $\gamma(s, t)$  at the times  $t$  between  $t_i = 28.4$  h and  $t_f = 180$  h are plotted as black lines for the positions  $s = 0, 0.1, \dots, 1$ . The red line shows the relation between  $2k_x$  and the averaged relative rate of change  $\bar{\gamma}$  of the cellular Dpp concentration. (D) The red line shows values of  $2k_x(t)$  that correspond to the values of  $\bar{\gamma}(t)$  at times  $t$  between  $t_{\text{on}} = 100$  h and  $t_f = 180$  h. The blue line represents a fit of the function  $2k_x = \alpha\bar{\gamma} + \beta$  to the red line, using  $\alpha$  and  $\beta$  as fit parameters. The best fit parameters are given in the text.

Fig. 3.10, A shows two examples of P-Mad gradients at different stages during development. The P-Mad concentration profiles are fitted well by the simple ansatz

$$p(x, t) = P_0(t) \exp\left(-\frac{x}{\lambda_p(t)}\right), \quad (3.16)$$

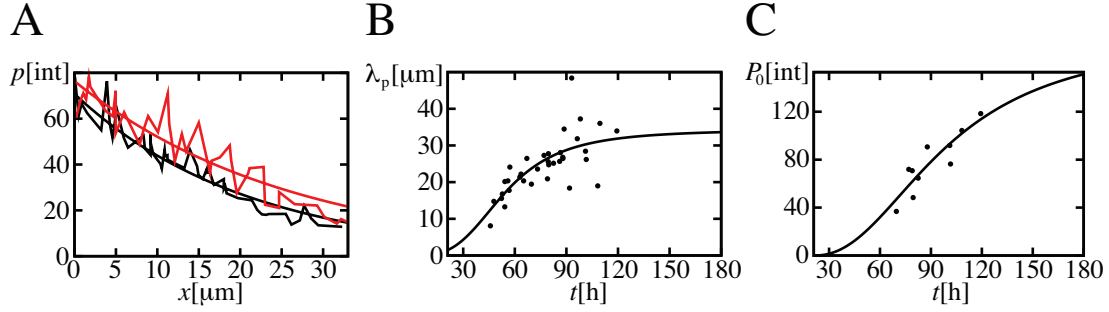


Figure 3.10: P-Mad gradients during wing disk development. (A) P-Mad concentration profiles at different stages during development. The P-Mad concentration measured in cell nuclei in units of fluorescence intensity is plotted as a function of the distance to the Dpp source. The red and black trace represent gradients at the larval ages  $t = 102$  h and  $t = 79$  h, respectively, and the red and black line are exponential fits to the data. (B) Decay length of P-Mad gradients as a function of larval age. (C) P-Mad concentration next to the Dpp source as a function of larval age. The data points in B and C are obtained by fitting Eq. (3.16) to individual gradients in wing disks of different ages. The black lines represent fits of Eqs. (3.17) to  $\lambda_p(t)$  and  $P_0(t)$ . As best fit parameters, we find  $\lambda_f^{(p)} = 34.3 \pm 8.8 \mu\text{m}$ ,  $\tau_p = 54.4 \pm 7.0$  h,  $q_p = 3.3 \pm 1.7$ ,  $P_0^{(f)} = 183 \pm 228$  units of fluorescence intensity,  $\tau_0 = 79 \pm 92$  h, and  $q_0 = 2.2 \pm 2.3$ .

where  $p$  is the P-Mad concentration,  $P_0$  is the P-Mad concentration at  $x = 0$ , and  $\lambda_p$  is the decay length of the P-Mad gradient. We have analyzed P-Mad gradients at many different developmental stages. In Fig. 3.10, B and C, the resulting P-Mad decay lengths and concentrations next to the Dpp source are plotted as functions of larval age, respectively. We fit the following functions to the data in Fig. 3.10, B and C,

$$\begin{aligned} \lambda_p(t) &= \lambda_f^{(p)} \frac{t^{q_p}}{\tau_p^{q_p} + t^{q_p}}, \\ P_0(t) &= P_0^{(f)} \frac{(t - t_i)^{q_0}}{\tau_0^{q_0} + (t - t_i)^{q_0}}. \end{aligned} \quad (3.17)$$

Here  $\lambda_f^{(p)}$ ,  $\tau_p$  and  $q_p$  are the fit parameters of the decay length of the P-Mad gradients, and  $P_0^{(f)}$ ,  $\tau_0$  and  $q_0$  are the fit parameters of the P-Mad concentration next to the Dpp source. The values of the optimized fit parameters are given in the caption of Fig. 3.10.

As in the case of Dpp, we can now calculate the cellular P-Mad concentration  $p_{\text{mov}}$  which is defined as

$$p_{\text{mov}}(s, t) = p(sl(t), t). \quad (3.18)$$

Inserting the exponentially decaying concentration profile (3.16) of P-Mad into this equa-

tion, the cellular P-Mad concentration becomes

$$p_{\text{mov}}(s, t) = P_0(t) \exp\left(\frac{-sl(t)}{\lambda_p(t)}\right). \quad (3.19)$$

Using the fits for  $\lambda_p(t)$  and  $P_0(t)$ , we can thus determine  $p_{\text{mov}}$  at any position during fly development. In Fig. 3.11, A the cellular P-Mad concentration is plotted as a function of larval age for cells that move along the trajectories  $x_s(t) = sl(t)$  with  $s = 0, 0.1, \dots, 1$ . As in the case of Dpp, the cellular P-Mad concentration depends strongly on position. Fig. 3.11, B shows the time derivative  $\dot{p}_{\text{mov}}$  of the cellular P-Mad concentration during development, which also shows a strong position dependence. However, the relative rate of change of the cellular P-Mad concentration

$$\sigma(s, t) = \dot{p}_{\text{mov}}(s, t)/p_{\text{mov}}(s, t), \quad (3.20)$$

which is plotted in Fig. 3.11, C for  $s = 0, 0.1, \dots, 1$  as a function of fly age, is almost position independent throughout development. Therefore, the relation between the growth rate  $2k_x$  and  $\sigma$ , which is plotted in Fig. 3.11, D, is also almost position independent, and it is unique in contrast to the relation between  $2k_x$  and  $\gamma$ , see Fig. 3.9, C. Moreover, it is very intuitive: for large values of  $\sigma$ , the growth rate saturates which can be explained by a minimal cell cycle time needed for a cell to double in size and to replicate its DNA; for small relative changes of the cellular P-Mad concentration in time, the growth rate decreases linearly with decreasing  $\sigma$ , and when  $\sigma \rightarrow 0$ , growth stops.

With the relative rate of change of the cellular P-Mad concentration, we have thus found a quantity (i) which depends on Dpp signaling activity, (ii) which is almost position independent throughout development, and (iii) which has a unique relation to the growth rate throughout development. The relation between  $2k_x$  and  $\sigma$  can be described by the function

$$2k_x = \frac{\alpha\sigma^\beta}{\delta^\beta + \sigma^\beta}, \quad (3.21)$$

which is plotted as the red line in Fig. 3.11, D. The values of the optimized fit parameters  $\alpha$ ,  $\beta$  and  $\delta$  are  $\alpha = 0.2577 \pm 0.0005$ ,  $\beta = 1.0559 \pm 0.0025$ , and  $\delta = 0.0986 \pm 0.0005$ .

Finally, we have thus found a possible rule by which the growth of the *Drosophila* wing disk can be controlled during the whole development: We propose that the growth rate is regulated by the relative rate of change  $\sigma$  of the cellular P-Mad concentration via the functional relation described by Eq. (3.21).

Of course, this hypothesis has to be tested experimentally. Experiments in which the growth of width  $w(t)$  of the Dpp source is manipulated are in preparation. In these experiments, one will find different dynamics of the Dpp gradient during development and thus a different  $\sigma$ , and it will be interesting to see whether the growth rate changes according to Eq. (3.21). Moreover, experiments in another imaginal disk of the fruit fly are planned, namely the haltere disk. It is very similar to the wing disk: Dpp is also produced there in response to Hedgehog and its signal is mediated by P-Mad. The idea of these experiments is that the cellular machinery that causes proliferation in response to the Dpp gradient is likely to be the same in the different disks, i.e. the explanation of

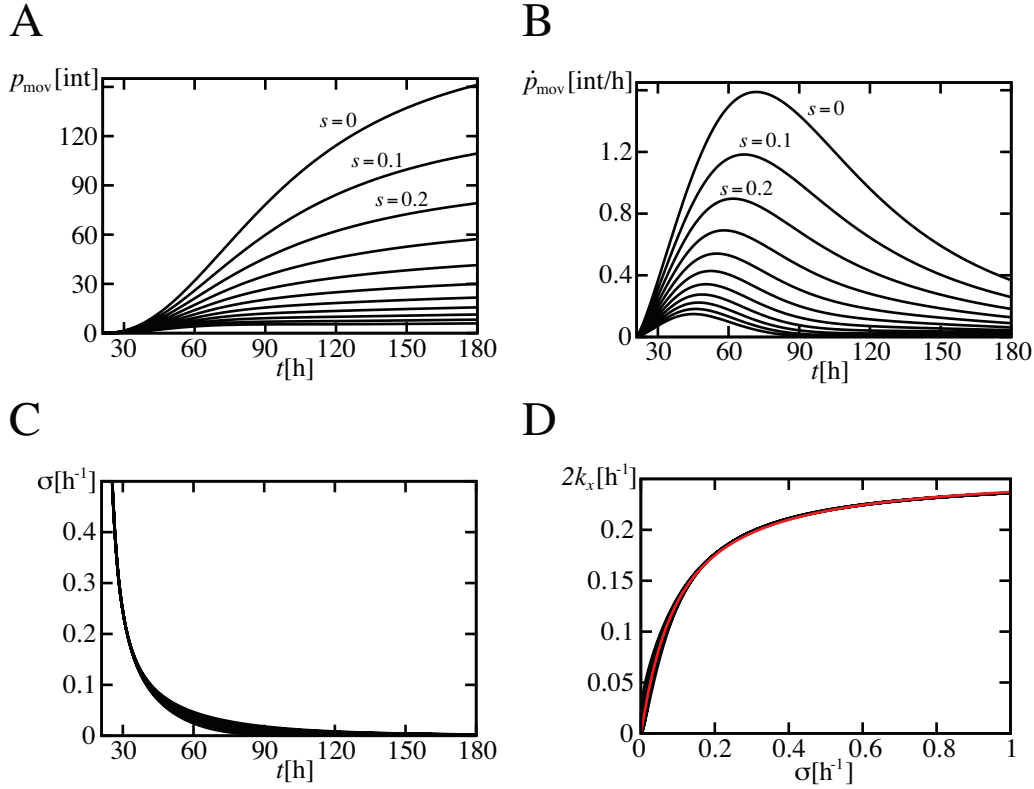


Figure 3.11: Cellular P-Mad concentration and its rate of change during wing disk development. (A) Cellular P-Mad concentration as a function of larval age for cells that move along the trajectories  $x_s(t) = sl(t)$  with  $s = 0, 0.1, \dots, 1$ . (B) Rate of change of the cellular P-Mad concentration as a function of larval age for the positions  $s = 0, 0.1, \dots, 1$  in the wing disk. (C) Relative rate of change of the cellular P-Mad concentration as a function of larval age for the positions  $s = 0, 0.1, \dots, 1$ . (D) Relation between the tissue growth rate  $2k_x$  and the relative rate of change of the cellular P-Mad concentration. The values of  $2k_x(t)$  that correspond to the values of  $\sigma(s, t)$  at times  $t$  throughout development are plotted as black lines for the positions  $s = 0, 0.1, \dots, 1$ . The red line represents a fit of Eq. (3.21) to the set of black lines.

growth control is likely to be universal. If that would be the case, the next step would be to test it also in other, closely related species.

How can cells measure and interpret the relative rate of change of the cellular concentration of P-Mad so that it regulates the cell division rate? One idea behind that is that on the one hand, P-Mad acts as a growth factor, i.e. it is needed for cell division [57], but on the other hand, P-Mad could also regulate the production of a growth inhibitor with some delay. By that, the relative rate of change of the cellular P-Mad concentration might control the ratio between growth factors and growth inhibitors in a cell. We want



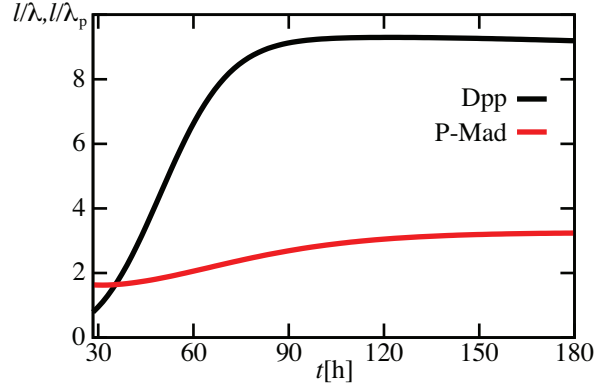


Figure 3.12: Ratio of tissue length and decay length of the Dpp and P-Mad gradients as functions of disk age. The length  $l(t)$  of the posterior compartment of the wing disk, the decay length  $\lambda(t)$  of the Dpp gradient, and the decay length  $\lambda_p$  of the P-Mad gradient are taken from the fits (3.12) and (3.17) to the experimental data.

to study these ideas in a quantitative description in future work.

Next, we want to consider the question why the relative rate of change  $\gamma$  of the cellular Dpp concentration is position dependent, whereas the relative rate of change  $\sigma$  of the cellular P-Mad concentration is almost independent on position in the disk. For that, we calculate  $\sigma(s, t)$  explicitly using Eq. (3.19),

$$\sigma(s, t) = \frac{\dot{P}_0(t)}{P_0(t)} - s \partial_t \left( \frac{l(t)}{\lambda_p(t)} \right). \quad (3.22)$$

Hence, the position dependence of  $\sigma$  vanishes if the ratio between the tissue length and the decay length of the gradient is constant in time. In Fig. 3.12, we have plotted this ratio for P-Mad and Dpp. We find that for P-Mad,  $l(t)/\lambda_p(t)$  shows a weak time dependence, whereas for Dpp,  $l(t)/\lambda(t)$  changes strongly in time in young disks and becomes almost constant at an age of about  $t = 100$  h, which was the time when  $\gamma$  became almost position independent, see Fig. 3.9, B.

In contrast to Dpp, P-Mad does not diffuse between different cells in the wing disk. Since P-Mad is retained in the cells, the stretching of the P-Mad gradient due to growth might be a more important effect than in the case of Dpp. This leads us back to the idea of Day and Lawrence [30] that the slope of a gradient might regulate growth. The relative slope of the P-Mad gradient measured by the moving cells is given by

$$\frac{\partial_x p_{\text{mov}}(x/l, t)}{p_{\text{mov}}(x/l, t)} = -\frac{1}{\lambda_p}, \quad (3.23)$$

where we used Eqs. (3.18) and (3.19). Hence, this quantity is independent of the position in the tissue. Moreover, it is related uniquely to the growth rate throughout development, see Fig. 3.13. Therefore, the relative change of the cellular P-Mad concentration

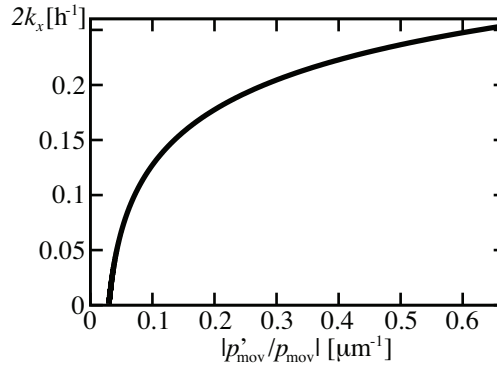


Figure 3.13: Relation between the tissue growth rate  $2k_x$  and the absolute value of the relative change of the cellular P-Mad concentration in space. The plot shows the values of  $2k_x(t)$  that correspond to the values of  $|p'_{\text{mov}}/p_{\text{mov}}| = 1/\lambda_p(t)$  at times  $t$  throughout development.

in space could also control the growth rate. However, wing disks in which Dpp is over-expressed ubiquitously grow to a larger final size than wildtype disks [74]. Since the P-Mad gradients should be rather flat in these disks, these experiments suggest that growth is not controlled by the relative slope of the P-Mad gradient. Since the production and degradation rate of Dpp vary with time, the relative change of the cellular P-Mad concentration in time does not vanish and could therefore control growth in these flies.

Finally, we come to the question how the Dpp concentration is related quantitatively to the P-Mad concentration. Here, we have described the P-Mad concentration by the simple phenomenological ansatz (3.16). However, if we want to simulate the feedback between growth and the P-Mad concentration profiles during development with our growth rule (3.21) as done in appendix B.3 for Dpp, we need to know how the P-Mad concentration is regulated by Dpp within the cells. In the next chapter, we present a microscopic theoretical description of the signal transduction of TGF- $\beta$  ligands such as Dpp via P-Mad on the single cell level. This description is used to analyze experimental data on Mad intracellular trafficking at the neuromuscular junction of the fruit fly, but a similar description might be applicable to capture P-Mad signaling in the wing disk which will be studied in future work.

## Chapter 4

# Kinetics of TGF- $\beta$ signaling in the cell

After the study of cell movements in growing tissues in chapter 2 and the analysis of morphogen spreading in these rearranging cell packings in chapter 3, we now consider morphogenetic signaling on the next scale of detail: On the single cell level, we study the intracellular transduction machinery of TGF- $\beta$  signaling during development [33].

Starting from a microscopic theoretical description that is based on a system of coupled ordinary differential equations, we analyze the kinetics of intracellular Mad trafficking in response to binding of TGF- $\beta$  ligands such as Dpp to receptors on the cell surface (see section 4.1). We determine the steady-state concentrations of Mad and P-Mad in two different compartments of the cell. For the case in which one compartment represents a protein reservoir for the second compartment, the rapid dynamics of the system is solved analytically using a separation of time scales.

We compare our theory to intracellular FRAP experiments performed at the neuromuscular junction of the developing fruit fly (see section 4.2). By optimizing the parameters of our description, we determine the nuclear import and export rates of Mad and P-Mad proteins, as well as the relative pool sizes of the different Mad species. We find that the rate of Mad phosphorylation increases with increasing levels of synaptic activity, which reveals a coupling between TGF- $\beta$  signaling and neuronal signaling during development.

### 4.1 Theoretical description of Mad intracellular trafficking

A microscopic theoretical description of Mad intracellular trafficking is schematically shown in Fig. 4.1. We distinguish between five different Mad species within the cell to account for the concentrations of Mad and P-Mad molecules that are present in the cytosol and nucleus.

The phosphorylation of cytosolic Mad by TGF- $\beta$  receptor activation is captured by the phosphorylation rate  $k_p$ . P-Mad is dephosphorylated in the cytosol with the rate  $k_d$ . Mad enters and exits the nucleus through nuclear pores at the rates  $k_{in}$  and  $k_{out}$ ,

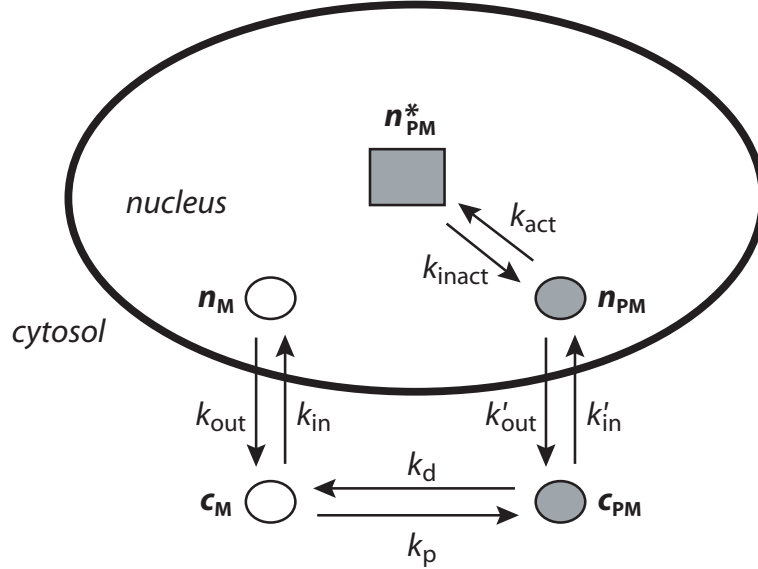


Figure 4.1: Schematic representation of intracellular Mad trafficking. Cytosolic Mad is phosphorylated by TGF- $\beta$  receptor activation. Mad and P-Mad enter and exit the nucleus through nuclear pores with different rates. Inside the nucleus, P-Mad becomes activated and binds to cofactors so that this molecular complex cannot cross the nuclear pore. For a definition of the various Mad pools and rates, see text.

respectively, from which the rates  $k'_{in}$  and  $k'_{out}$  of P-Mad nuclear trafficking might differ. Moreover, there is a third pool of Mad molecules in the nucleus, namely the pool of transcriptionally active P-Mad (P-Mad\*) which exchanges with inactive nuclear P-Mad via the rates  $k_{act}$  and  $k_{inact}$ . The pool P-Mad\* describes nuclear P-Mad molecules that are bound to other transcription factors so that these protein complexes cannot leave the nucleus through the nuclear pores.

Assuming that all exchange processes between the different pools are linear, their kinetics are described by the following system of coupled rate equations:

$$\begin{aligned}
 \frac{dn_M}{dt} &= k_{in}c_M - k_{out}n_M \\
 \frac{dn_{PM}}{dt} &= k'_{in}c_{PM} - k'_{out}n_{PM} + k_{inact}n_{PM}^* - k_{act}n_{PM} \\
 \frac{dn_{PM}^*}{dt} &= k_{act}n_{PM} - k_{inact}n_{PM}^* \\
 \frac{dc_M}{dt} &= \frac{V_n}{V_c} (k_{out}n_M - k_{in}c_M + k_d c_{PM} - k_p c_M) \\
 \frac{dc_{PM}}{dt} &= \frac{V_n}{V_c} (k_p c_M - k_d c_{PM} + k'_{out}n_{PM} - k'_{in}c_{PM}) .
 \end{aligned} \tag{4.1}$$

Here  $n_M$  is the nuclear Mad concentration,  $n_{PM}$  is the nuclear P-Mad concentration,

$n_{\text{PM}}^*$  is the concentration of the transcriptionally active P-Mad\*,  $c_{\text{M}}$  is the cytosolic Mad concentration, and  $c_{\text{PM}}$  is the cytosolic P-Mad concentration. Moreover,  $V_{\text{n}}$  is the volume of the nucleus, and  $V_{\text{c}}$  is the volume of the cytosol. The ratio  $V_{\text{n}}/V_{\text{c}}$  appears in Eqs. (4.1) since an exchange of a molecule between cytosol and nucleus has a different effect on the cytosolic and nuclear concentration.

In steady state (s), the concentrations of the different Mad species can be expressed in terms of the total cytosolic concentration  $c_{\text{tot}} = c_{\text{M}} + c_{\text{PM}}$ ,

$$\begin{aligned} n_{\text{M}}^{\text{s}} &= \frac{Y}{1+Z} c_{\text{tot}}^{\text{s}} \\ n_{\text{PM}}^{\text{s}} &= \frac{Y'}{1+1/Z} c_{\text{tot}}^{\text{s}} \\ n_{\text{PM}}^{*\text{s}} &= \frac{XY'}{1+1/Z} c_{\text{tot}}^{\text{s}} \\ c_{\text{M}}^{\text{s}} &= \frac{1}{1+Z} c_{\text{tot}}^{\text{s}} \\ c_{\text{PM}}^{\text{s}} &= \frac{1}{1+1/Z} c_{\text{tot}}^{\text{s}}. \end{aligned} \tag{4.2}$$

Here  $X = k_{\text{act}}/k_{\text{inact}}$ ,  $Y = k_{\text{in}}/k_{\text{out}}$ ,  $Y' = k'_{\text{in}}/k'_{\text{out}}$ , and  $Z = k_{\text{p}}/k_{\text{d}}$  are dimensionless ratios of the exchange rates.

The concentrations of the different Mad species inside a cell as well as the exchange rates between the different pools can be measured in FRAP experiments. In these experiments, fluorescently labeled Mad molecules are photobleached in a cell nucleus and the recovery of the nuclear fluorescence is recorded and quantified. We assume that the experiments are initiated at a moment when the system has relaxed to the steady state. Therefore, the steady-state values of the concentrations (4.2) are chosen as an initial condition for our theoretical description of the FRAP experiments. By bleaching the fluorescence in the nucleus, the concentration of fluorescent nuclear Mad is reduced to the fraction  $b$  (bleaching depth), while the cytosolic concentration of fluorescent molecules remains unchanged. We assume here that the bleaching process occurs instantaneously.

In order to describe the recovery of the nuclear fluorescence after bleaching, we assume that the exchange of  $n_{\text{PM}}^*$  with  $n_{\text{PM}}$  via the rates  $k_{\text{act}}$  and  $k_{\text{inact}}$  is slow compared to the duration of the experiments (1000 seconds) and accounts for the fraction of molecules which is immobile and does not recover during the experiment (immobile fraction). To describe the fluorescence recovery, we thus neglect the exchange by the rates  $k_{\text{act}}$  and  $k_{\text{inact}}$ . Since  $V_{\text{n}} \ll V_{\text{c}}$ , changes of the cytosolic concentrations during recovery can be ignored (see Eqs. (4.1)). With these assumptions, the FRAP kinetics is described by

$$\begin{aligned} \frac{dn_{\text{M}}}{dt} &= k_{\text{in}}c_{\text{M}} - k_{\text{out}}n_{\text{M}} \\ \frac{dn_{\text{PM}}}{dt} &= k'_{\text{in}}c_{\text{PM}} - k'_{\text{out}}n_{\text{PM}} \\ \frac{dn_{\text{PM}}^*}{dt} &= 0. \end{aligned} \tag{4.3}$$

The solution to these equations is

$$\begin{aligned} n_M(t) &= n_{M,0} \left( 1 - (1-b)e^{-k_{\text{out}}t} \right) \\ n_{PM}(t) &= n_{PM,0} \left( 1 - (1-b)e^{-k'_{\text{out}}t} \right), \end{aligned} \quad (4.4)$$

where the constants  $n_{M,0}$  and  $n_{PM,0}$  are equal to the steady-state values of the nuclear Mad and P-Mad concentrations  $n_M^s$  and  $n_{PM}^s$ , respectively, as given in Eqs. (4.2). The observed nuclear fluorescence per unit volume  $I(t)$  is proportional to the total nuclear concentration  $n_{\text{tot}} = n_M + n_{PM} + n_{PM}^*$ . The normalized fluorescence recovery  $F(t) = (I(t) - I(0))/I_0$ , where  $I(0)$  is the fluorescence intensity immediately after bleaching and  $I_0$  its pre-bleach value, is therefore equal to the normalized nuclear concentration  $(n_{\text{tot}}(t) - n_{\text{tot}}(0))/n_{\text{tot}}^s$ . According to Eq. (4.4),  $F(t)$  behaves thus as

$$F(t) = A(1-b) \left( 1 - e^{-k_{\text{out}}t} \right) + B(1-b) \left( 1 - e^{-k'_{\text{out}}t} \right), \quad (4.5)$$

where  $A = n_M^s/n_{\text{tot}}^s$  and  $B = n_{PM}^s/n_{\text{tot}}^s$ .

In a situation, in which either one of the two mobile Mad pools dominates, Eq. (4.5) reduces to a single exponential. This case corresponds to a simple phenomenological model which only describes effective exchanges between the total cytosolic ( $c_{\text{tot}}$ ) and mobile Mad pool ( $n_{\text{mob}}$ ) via the rates  $k_i$  and  $k_e$ , whereas the immobile nuclear pool of concentration  $n_{\text{im}}$  is assumed to be constant during the experiment, see Fig. 4.2. Moreover, the cytosolic concentration is assumed to be constant during the time course of the FRAP experiment in this description. Therefore, the FRAP kinetics in the phenomenological model is described by

$$\begin{aligned} \frac{dn_{\text{mob}}}{dt} &= k_i c_{\text{tot}} - k_e n_{\text{mob}} \\ \frac{dn_{\text{im}}}{dt} &= 0 \\ \frac{dc_{\text{tot}}}{dt} &= 0, \end{aligned} \quad (4.6)$$

The solution to the equation describing the recovery of the mobile pool is

$$n_{\text{mob}}(t) = n_{\text{mob}}^s \left( 1 - (1-b)e^{-k_e t} \right), \quad (4.7)$$

and thus the recovery of the normalized nuclear fluorescence  $F(t) = (n_{\text{tot}}(t) - n_{\text{tot}}(0))/n_{\text{tot}}^s$  where  $n_{\text{tot}} = n_{\text{mob}} + n_{\text{im}}$  can be described by the single exponential equation

$$F(t) = m(1-b) \left( 1 - e^{-k_e t} \right), \quad (4.8)$$

where  $m = n_{\text{mob}}^s/n_{\text{tot}}^s$  is the nuclear mobile fraction.

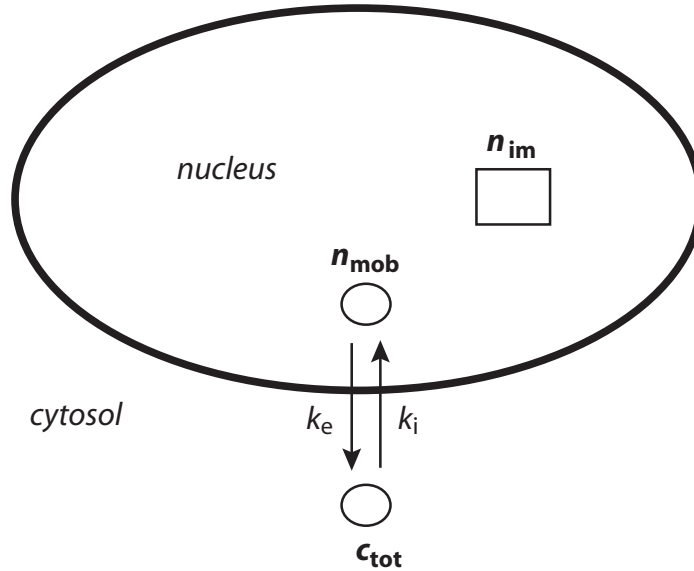


Figure 4.2: Phenomenological description for nuclear Mad trafficking. Cytosolic Mad ( $c_{\text{tot}}$ ) enters the nucleus through nuclear pores with the effective rate  $k_i$ . Inside the nucleus, we distinguish between two different Mad populations, namely an immobile one ( $n_{\text{im}}$ ), which is constant during the FRAP experiment, and a mobile one ( $n_{\text{mob}}$ ), which exits the nucleus with rate  $k_e$ .

## 4.2 Kinetic parameters of Mad intracellular trafficking

We fit Eqs. (4.5) and (4.8) to recovery curves of FRAP experiments performed in muscle cells of the developing fruit fly which are connected to neurons via neuromuscular junctions [4, 99]. In this system, the presence of the integral components of TGF- $\beta$  signaling (see Fig. 1.1), i.e. TGF- $\beta$  ligands, Tkv receptors, as well as Mad and P-Mad molecules, has been shown recently [33]. To study the influence of synaptic activity on the nuclear import and export kinetics of Mad, the experiments were done under three different conditions, namely in control animals without synaptic activity, in animals with synaptic stimulation by a high potassium ( $\text{K}^+$ ) solution, and in mutant flies expressing the constitutively active Tkv<sup>QD</sup> receptors at which Mad is permanently phosphorylated, see Fig. 4.3.

Expression (4.5) derived from our microscopic theoretical description is fitted to the averaged experimental data (see Fig. 4.3, A) using  $A$ ,  $B$ ,  $k_{\text{out}}$  and  $k'_{\text{out}}$  as fit parameters. This fit is done under the constraint that the fit parameters  $k_{\text{out}}$  and  $k'_{\text{out}}$ , as well as the quantities  $X$ ,  $Y$  and  $Y'$  are the same for all three experimental conditions (control,  $\text{K}^+$  and Tkv<sup>QD</sup>), and that only  $Z$  differs (see Eqs. (4.2)). These constraints correspond to a situation in which the different synaptic activity levels only affect the phosphorylation rate of Mad while all other rates are constant. By that, we can effectively reduce

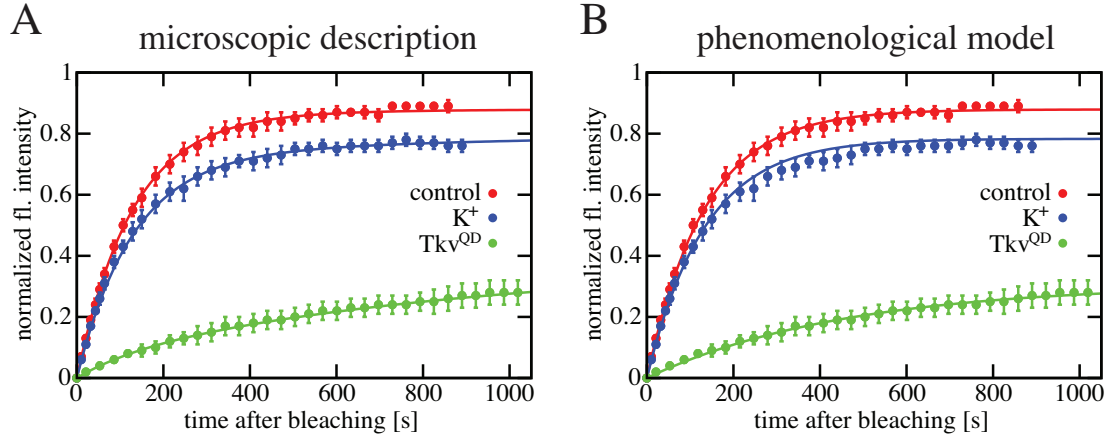


Figure 4.3: Recovery curves of FRAP experiments in nuclei of *Drosophila* muscle cells for the 3 different conditions control,  $K^+$ , and  $Tkv^{QD}$ . In both diagrams, the average fluorescence intensity of at least  $n = 5$  experiments for each condition normalized to its value before bleaching and the bleaching depth is plotted as a function of time after bleaching. The error bars indicate the standard deviations from the mean values. (A) Fit of the specific microscopic description to the data. (B) Fit of the phenomenological model to the FRAP curves. For details of the fits, see text.

the number of free fit parameters to six parameters for the three recovery curves as explained in appendix C.1. For comparison, we fit Eq. (4.8) of the phenomenological model independently to each recovery curve of the at least  $n = 5$  experiments for each of the three conditions (control,  $K^+$  and  $Tkv^{QD}$ ), using  $m$  and  $k_e$  as fit parameters (see Fig. 4.3, B). The effective import rate  $k_i$  can then be determined by Eq. (C.3). The values of all parameters obtained by these fits are displayed in Table 4.1.

The two fit functions (4.5) and (4.8) derived in the specific microscopic description and the phenomenological model, respectively, describe the experimental data well (see Fig. 4.3, A and B). As the mobile nuclear pool for the control and  $K^+$  condition consists mainly of non-phosphorylated Mad (see Table 4.1), the double exponential Eq. (4.5) is dominated by its first term. Conversely, in the case of  $Tkv^{QD}$ , the mobile nuclear pool mainly contains phosphorylated Mad (see Table 4.1) so that Eq. (4.5) is dominated by the second exponential. Thus the single exponential fit (4.8) represents a good approximation of the double exponential fit (4.5) for the three mutant conditions. Note however that the double exponential fit allows us to determine the changes of the phosphorylation rate  $k_p$  in the different conditions and can account for the different mobile fractions.

We find that in the case of  $Tkv^{QD}$ , the phosphorylation rate  $k_p$  increases by a factor of about 200 with respect to control muscles, assuming that all other rates are fixed. This leads to a 14 times higher level of steady-state mobile P-Mad in the nucleus. The  $K^+$  stimulation increases the phosphorylation rate by a factor of about 5 with respect to resting muscles, and the nuclear P-Mad concentration 4 times. Furthermore, only



	control	K <sup>+</sup>	Tkv <sup>QD</sup>
$k_{\text{in}} [\text{s}^{-1}]$	<b>0.0283 ± 0.0003</b>		
$k_{\text{out}} [\text{s}^{-1}]$	<b>0.0080 ± 0.0001</b>		
$k'_{\text{in}} [\text{s}^{-1}]$	<b>0.0164 ± 0.0064</b>		
$k'_{\text{out}} [\text{s}^{-1}]$	<b>0.0012 ± 0.0003</b>		
$k_{\text{act}}/k_{\text{inact}}$	<b>1.80 ± 0.32</b>		
$k_{\text{p}}/k_{\text{d}}$	0.0064 ± 0.0021	0.029 ± 0.010	1.28 ± 0.93
$n_{\text{M}}^{\text{s}}/n_{\text{tot}}^{\text{s}}$	0.935 ± 0.004	0.758 ± 0.008	0.068 ± 0.028
$n_{\text{PM}}^{\text{s}}/n_{\text{tot}}^{\text{s}}$	0.023 ± 0.003	0.086 ± 0.011	0.332 ± 0.043
$n_{\text{PM}}^{*\text{s}}/n_{\text{tot}}^{\text{s}}$	0.042 ± 0.005	0.156 ± 0.014	0.600 ± 0.051
$c_{\text{M}}^{\text{s}}/c_{\text{tot}}^{\text{s}}$	0.994 ± 0.002	0.971 ± 0.009	0.439 ± 0.180
$c_{\text{PM}}^{\text{s}}/c_{\text{tot}}^{\text{s}}$	0.006 ± 0.002	0.029 ± 0.009	0.561 ± 0.180
$k_{\text{i}} [\text{s}^{-1}]$	0.028 ± 0.002	0.020 ± 0.002	0.017 ± 0.004
$k_{\text{e}} [\text{s}^{-1}]$	0.0078 ± 0.0005	0.0074 ± 0.0006	0.0023 ± 0.0003
$n_{\text{im}}^{\text{s}}/n_{\text{tot}}^{\text{s}}$	0.052 ± 0.015	0.19 ± 0.01	0.67 ± 0.04

Table 4.1: Specific rates and pool sizes of Mad and P-Mad determined with the microscopic theoretical description, as well as effective rates and immobile fraction determined with the phenomenological model for unstimulated controls, K<sup>+</sup> stimulated muscles, and Tkv<sup>QD</sup> expressing flies. The values are obtained by fitting Eqs. (4.5) and (4.8) to the data, details are discussed in the text. Note that the specific import and export rates of Mad and P-Mad as well as the ratio of the exchange rates between nuclear P-Mad and P-Mad\* (bold) are the same for the 3 conditions control, K<sup>+</sup>, and Tkv<sup>QD</sup>. For each quantity, the best fit parameter of the least squares fit and the corresponding standard error are displayed.

about 4% of nuclear Mad is immobile in control muscles during the FRAP experiment, suggesting low levels of Mad signaling in the resting synapse. In contrast, synaptic K<sup>+</sup> stimulation increases the immobile pool of Mad in the nucleus by a factor of about 4, and constitutive signaling in Tkv<sup>QD</sup> mutants leads to an increase by an order of magnitude of the immobile fraction. These data suggest that Mad signaling is increased upon stimulation of the muscle. The origin of the immobile fraction of the nuclear Mad molecules is studied in appendix C.2.

In control muscles, the effective nuclear import rate  $k_i$  of Mad is higher than its export rate, accounting for a 3.7 times higher concentration of Mad in the nucleus than in the cytosol which has been measured experimentally [33]. Upon constitutive signaling in the  $\text{Tk}v^{\text{QD}}$  mutants, the ratio of import to export rate (7.4) is higher than in the control (3.6). This difference in the import to export ratio leads to a net accumulation of nuclear Mad in  $\text{Tk}v^{\text{QD}}$  muscles about 3.5 times above the levels of the control [33]. Interestingly, the effective import rate does not increase, but decreases slightly upon constitutive signaling, while the effective export rate significantly decreases. Consistently, the specific import rate of P-Mad is about 1.7 times smaller than for Mad, while the specific export rate is much smaller (7-fold) compared to the non-phosphorylated protein. Thus the increase in the net nuclear accumulation of Mad during signaling is explained by a decrease in the export of the total Mad pool, rather than by an increase in its import into the nucleus.

### 4.3 Discussion

We can relate our microscopic theoretical description (see Fig. 4.1) to the phenomenological model (see Fig. 4.2). The different pools of Mad molecules of the two descriptions are related by  $c_{\text{tot}} = c_{\text{M}} + c_{\text{PM}}$ ,  $n_{\text{mob}} = n_{\text{M}} + n_{\text{PM}}$  and  $n_{\text{im}} = n_{\text{PM}}^*$ . Moreover, the effective import and export rates can be related to the specific rates:

$$\begin{aligned} k_i &= \frac{k_{\text{in}}^s c_{\text{M}}^s + k'_{\text{in}} c_{\text{PM}}^s}{c_{\text{M}}^s + c_{\text{PM}}^s} \\ k_e &= \frac{k_{\text{out}} n_{\text{M}}^s + k'_{\text{out}} n_{\text{PM}}^s}{n_{\text{M}}^s + n_{\text{PM}}^s}. \end{aligned} \tag{4.9}$$

Using the fit results for the specific import and export rates, the calculated values of these quantities are consistent with the values found by the single exponential fits, see Table 4.1.

In summary, our microscopic theoretical description of Mad intracellular trafficking describes the data well. We have shown that Mad and P-Mad molecules enter and exit the nuclei of the muscle cell at different specific rates. The rate of Mad phosphorylation increases upon synaptic stimulation and leads to higher levels of transcriptionally active P-Mad in the nucleus. Our findings are consistent with the existence of a  $\text{TGF-}\beta$  signaling cascade at the developing neuromuscular junction of the fruit fly which is initiated in the synapse through exocytosis of  $\text{TGF-}\beta$  ligands. Binding of the ligands to  $\text{Tk}v$  receptors on the cell surface of the muscle cell leads to activation of the receptors and thereby to phosphorylation of Mad. P-Mad accumulates in the nuclei of the muscle cell, where it might mediate transcriptional control of the target genes of the signaling pathway.

It has been shown that signaling events from the muscle to the synapse exist and that they control growth, morphology and synaptic function [1, 68, 70]. What could then be the role of a signaling event from the synapse to the muscle? We speculate that upon synaptic stimulation,  $\text{TGF-}\beta$  ligands are released together with the neurotransmitters. If this is true, postsynaptic signaling coupled to synaptic activity could provide the muscle

with information about the activity of the neuron and thus control the growth and development of the neuromuscular junction. It will be interesting to study experimentally whether the same vesicles that contain the neurotransmitter contain the TGF- $\beta$  growth factor.

In future work, our theoretical description of Mad intracellular trafficking can be used to examine the relation between the Dpp and P-Mad gradients in the growing wing disk. Based on our microscopic description for a single cell, one can develop a continuum theory of Mad intracellular trafficking on the level of a tissue. In this description, the concentration  $p_{\text{mov}}$  in the nuclei of the moving cells corresponds to the concentration  $n_{\text{PM}} + n_{\text{PM}}^*$  of the discrete description, and the rate  $k_p$  of Mad phosphorylation will be some function of the Dpp concentration and thus depend on space. Moreover, our microscopic description might also be useful to investigate on the single cell level possible mechanisms for the regulation of the cell division rate by Dpp and P-Mad as discussed in section 3.4. Eventually, this would allow us to study the full feedback between cell rearrangements in growing tissues, the formation of morphogen gradients, and the control of the cell division rate via P-Mad signaling in response to the morphogenetic signal.



## Chapter 5

# Summary and outlook

In this work, we theoretically investigated morphogenetic signaling processes that occur during the development and growth of multicellular organisms. As our main results, we developed a continuum description of cell rearrangements in anisotropically growing tissues. We have shown that the flow field of cell movements which result from oriented cell division and apoptosis enters as a drift term in the transport equation of morphogen spreading, which we have discussed in detail. And finally, we developed a microscopic theoretical description of the transduction machinery of morphogenetic signals within an individual cell.

**Dynamics of anisotropic tissue growth** In chapter 2, we have presented a coarse-grained physical description of cell rearrangements in growing tissues caused by oriented cell division and apoptosis [14]. Our continuum theory which describes the tissue as an effective viscous material predicts average cellular trajectories that exhibit anisotropic scaling behaviors. If cell division and apoptosis balance, there is no net growth, but for anisotropic cell division the tissue undergoes spontaneous shear deformations.

Moreover, we developed a discrete fluid-like model in which individual cells are treated as elastic objects that interact with each other via potential forces and friction forces. In our numerical simulations, in which cell division and apoptosis is implemented as a stochastic process, we found flow fields and cell trajectories that are on average well described by our continuum theory.

Based on our continuum description, we predicted shape changes of epithelia caused by oriented cell division and apoptosis. Our theoretical results were compared to measured shapes of the *Drosophila* wing disk during development. We have shown that our continuum theory describes the observed shape changes of the tissue boundary very well, which allowed us to determine the isotropic and anisotropic parts of the growth rate in the wing disk. We thereby revealed that the disk does grow anisotropically, and that the strength of the anisotropy depends on the expression level of the morphogen Dpp.

**Morphogen gradients in growing tissues** In section 3.2, we have discussed the effects of cell rearrangements on the spreading of morphogens at the example of Dpp in

the growing wing disk. Based on the continuum description of morphogen transport by Bollenbach et al. [17, 18, 19], we have shown that cell movements due to cell division cause a drift term in the effective diffusion equation for morphogen transport. We have calculated the steady state of the concentration profile (see Eq. (3.10)) which is given by a sum of confluent hypergeometric functions and approaches the exponentially decaying concentration profile (3.3) in the limit of vanishing growth rate. As for the average cell trajectories in the tissue, growth causes a power law for the decay of the morphogen gradient. We have discussed the growth effects of stretching and dilution on morphogen gradients which are captured by the drift term in the transport equation. For Dpp, the stretching of the gradient leads to a symmetry break in the concentration profile (see Fig. 3.3), which became evident by a coordinate transformation of the diffusion-advection equation into the system of fixed center of the Dpp source, see Eq. (3.11).

In sections 3.1 and 3.3, we applied our theory of morphogen transport in growing tissues on recent experimental data on the spreading of Dpp in the developing wing disk. We presented an analysis of FRAP experiments by which the kinetic parameters of Dpp spreading have been determined at different stages of wing disk development. Furthermore, our FRAP analysis for thermosensitive “shibire-rescue” mutant flies has shown that endocytosis is required for Dpp movement, which is dominated by intracellular transport in agreement with transcytosis and inconsistent with extracellular diffusion [55]. We have used the measured parameters for a numerical calculation of the evolution of the Dpp concentration profile during wing disk development, which is well described by a succession of adiabatically changing steady-state gradients. It turned out that the drift of Dpp molecules due to growth is negligible, so that the decay length of the Dpp gradient is not significantly changed by growth. Nevertheless, tissue growth plays a crucial role for morphogenetic signaling since it strongly affects the cellular Dpp concentration as the cells change their position within the Dpp gradient, see Fig. 3.8.

In section 3.4, we finally addressed the unsolved question how the graded Dpp concentration profile can control the approximately homogeneous growth rate in the wing disk. In view of our results on the Dpp gradient during wing disk development, we have discussed several approaches that try to explain growth regulation by Dpp. We found that the relative change of the cellular Dpp concentration in time provides a possible rule for growth control at late developmental stages, even though it lacks an explanation for growth regulation at early times. Eventually, we investigated concentration profiles of P-Mad in the developing wing disk, which mediates the Dpp signal within the cells. We have shown that the relative rate of change  $\sigma$  of the cellular P-Mad concentration is position independent throughout development. Furthermore, it turned out that the growth rate of the wing disk increases linearly with small  $\sigma$  and saturates at large  $\sigma$ . Therefore, the relative change of the cellular P-Mad concentration in time is a possible measure for the regulation of the cell division rate throughout wing disk development.

**Kinetics of TGF- $\beta$  signaling in the cell** In chapter 4, we focused on the intracellular transduction of the morphogenetic signal via the phosphorylation of Mad proteins. We developed a microscopic theoretical description of the kinetics of Mad intracellular

trafficking in response to the binding of TGF- $\beta$  ligands to receptors on the cell surface [33]. We determined the concentrations of different Mad species in the cytosol and nucleus of the cell at steady state, and we solved the dynamics for the nuclear trafficking of Mad and P-Mad in case of a cytosolic protein reservoir.

Our theoretical results were compared to FRAP experiments within muscle cells at developing neuromuscular junctions of the fruit fly. We determined the relative pool sizes of Mad and P-Mad in the cytosol and nucleus, as well as the nuclear import and export rates of the different Mad species. Moreover, we determined the phosphorylation rate of Mad in response to receptor-mediated TGF- $\beta$  signaling. We found that the phosphorylation rate increases with increasing levels of synaptic activity, which shows that synaptic signaling via neuronal action potentials modulates developmental signaling via TGF- $\beta$  growth factors.

**Discussion** In our investigation of the growth of incompressible tissues (see section 2.1.3), we focused on internal force balances since we were mostly interested in average cell rearrangements that result from cell division and apoptosis. Possible external interactions as e.g. friction on a substrate can be taken into account by an external force density as introduced in Eq. (2.2). Moreover, the parameters of our theory might depend on position in the tissue as in particular the orientation  $\mathbf{p}$  of the cell division axis [9]. Such position dependencies, which we have neglected for simplicity, may cause the small deviations between the measured effective growth rates in the wing disk and the optimized function  $k_{\text{eff}}(\varphi)$  that results from our theory (see Fig. 2.9).

While we focused in our discussion of the morphogen transport equation (3.7) on Dpp spreading in the growing wing disk, Eq. (3.7) also holds for the spreading of other morphogens in growing epithelia with modified source terms. An example for morphogen transport that can be described by Eq. (3.7) with a different source term is given by Hh, which is produced in the whole posterior compartment of the wing disk and spreads into the anterior compartment where it regulates the production of Dpp. Another example is Wg, which is produced in a small stripe at the dorsal-ventral compartment boundary in the wing disk. In contrast to Dpp, Wg is produced on both sides of the compartment boundary so that the stretching of the gradient due to growth does not cause a symmetry breaking in the Wg concentration profile.

Concerning our data analysis in sections 3.3 and 3.4, the fits to the measured decay length  $\lambda_p(t)$  of the P-Mad gradient and the concentration  $P_0(t)$  next to the Dpp source as functions of larval age (see Fig. 3.10) are not as reliable as the fits to the data for the corresponding quantities  $\lambda(t)$  and  $C_0(t)$  that characterize the Dpp gradient (see Fig. 3.4). Further experiments need to be performed to validate the optimized functions of  $\lambda_p(t)$  and  $P_0(t)$ . Nevertheless, the current data strongly indicates that the decay length of the P-Mad gradients undergoes a faster increase during wing disk development than the decay length of the Dpp gradients, which is the reason for the different position dependencies of the relative rate of change of the cellular concentrations of the two proteins (see Figs. 3.9, B and 3.11, C). In the possible rule for growth regulation by the relative change of the cellular P-Mad concentration in time (see Eq. (3.21)), it seems that

the decay length  $\lambda_p(t)$  scales with the tissue length (see Fig. 3.12) in order to generate homogeneous tissue growth (see Eq. (3.22)).

In our microscopic theoretical description of the kinetics of Mad intracellular trafficking in response to receptor-mediated TGF- $\beta$  signaling, we only took linear exchange processes between the different Mad pools into account (see Eq. (4.1)), which was sufficient to describe the FRAP data of Mad nuclear trafficking at the *Drosophila* neuromuscular junction. However, nonlinear exchange processes might be relevant in other systems as e.g. in the wing disk. So far, we did not study the kinetics of Mad intracellular trafficking in the wing disk, because there, the cells with an average diameter of about  $2.6 \mu\text{m}$  are much smaller than the muscle cells, in which a cell nucleus has an average diameter of about  $6.7 \mu\text{m}$ . Therefore, FRAP experiments within individual cells in the wing disk are much more difficult than in muscle cells and have not yet been performed.

**Outlook** Our theoretical description of the dynamics of anisotropic tissue growth, which was developed in this work and tested experimentally by measured shape changes of the *Drosophila* wing disk during development, can be further tested by clone experiments in the wing disk. In these experiments, some cells are marked fluorescently at an early stage of wing disk development. At each cell division, the two daughter cells inherit the fluorescent signal from the dividing mother cell. By that, the area, shape, and position of cell clusters formed by the descendants of the initially marked cells can be recorded and quantified at a later stage of development. The average area and shape of clones depending on the position in the tissue can be determined from our continuum theory and compared to the experimental data. Moreover, the formation of clones can be studied in our discrete fluid model. In our growth simulations, we have found that the fragmentation of clones, i.e. the number of cell clusters into which a single clone is separated, depends on tissue viscosity. Therefore, the clone experiments can be used to constrain the parameter space of our theoretical description.

Furthermore, our simulations of tissue growth can be applied to study the conditions under which a straight compartment boundary between two distinguishable cell populations forms, as e.g. the AP boundary in the wing disk, see Fig. 1.2. It has been shown that a reduction of the attractive force  $f_1$  in our discrete fluid model (see Fig. 2.2) for the interaction between cells of different type, while keeping the interaction between cells of the same type unchanged, leads to the formation of a straight compartment boundary [79].

Concerning our analysis of morphogen gradients in growing epithelia, we still lack a theoretical description of the formation of the P-Mad gradient which intracellularly mediates the Dpp signal in the growing wing disk. In such a description, one has to take into account the phosphorylation of Mad in response to the Dpp signal, the dephosphorylation of P-Mad molecules, the stretching and dilution of the P-Mad gradient due to tissue growth, and a possible boost of the cellular P-Mad concentration during each cell division that has been observed in experiments [15]. Moreover, the intracellular trafficking of Mad and P-Mad which has been investigated in this thesis has to be taken into account, since the measured concentration profiles in the wing disk represent nuclear



P-Mad inside the cells (see Fig. 3.10). An understanding of the relation between the cellular Dpp and P-Mad concentration would allow to simulate the feedback between the formation of the concentration profiles of these proteins and tissue growth on the basis of our rule for growth control by the relative rate of change of the cellular P-Mad concentration (see Eq. (3.21)).

To answer the question, how the relative rate of change of the cellular P-Mad concentration could regulate the division rate of a cell, a microscopic theoretical description of growth control needs to be developed. Moreover, our rule for growth regulation has to be tested experimentally. Experiments in which the relative rate of change of the cellular P-Mad concentration is manipulated are in preparation. Such a manipulation can e.g. be achieved in experiments, in which the increase of the width  $w(t)$  of the Dpp source is stopped at different larval ages during development. Another example are cell culture experiments, in which the relative rate of change of the Dpp and P-Mad concentration can be controlled by hand. It will be interesting to see whether modifications of the relative rate of change of the cellular P-Mad concentration lead to changes in the growth rate that are consistent with our rule for growth control (see Eq. (3.21)).

Overall, this work demonstrates the strength of the interplay between quantitative biological experiments and concepts of theoretical physics for shedding more light on morphogenetic signaling processes in growing tissues. We look forward to future research in this exciting field, which maybe will answer questions such as why cats are smaller than lions, and why our left and right arm are roughly of the same length.



# Appendix A

## Mechanics of tissue growth

Here we present some analytical calculations performed on the basis of our theory of anisotropic tissue growth. First we discuss the growth of compressible tissues. In the continuum limit, we show how the growth rate  $k_g$  and the apoptosis rate  $k_a$  are related to the probability  $p$  for cell division and the cell lifetime  $t_L$  of our discrete description. We briefly explain how the force balance Eq. (2.10) of the discrete model is solved numerically. Moreover, we show how tissues change their shapes according to cell rearrangements caused by oriented cell division. And finally, we discuss how the shape changes of the wing disk are measured.

### A.1 Growth of compressible tissues

In this section, we consider a compressible tissue with bulk elastic modulus  $\chi$ . For simplicity, we focus on the case of isotropic growth in polar coordinates, i.e.  $\mu = 0$ ,  $\mathbf{v}(\mathbf{r}) = v(r)\mathbf{e}_r$  with constant rates of growth and apoptosis. The cell density and the flow velocity obey

$$\partial_t \rho = (k_g - k_a)\rho - \frac{1}{r}\rho v - \rho \partial_r v - v \partial_r \rho, \quad (\text{A.1})$$

$$\left( \partial_r^2 + \frac{1}{r}\partial_r - \frac{1}{r^2} \right) v = \frac{1}{\eta + \zeta} \partial_r P. \quad (\text{A.2})$$

With the initial condition  $\rho(r \leq R_0, t = 0) = \rho_i$  of constant cell density  $\rho_i$  within an area of radius  $R_0$ , the dynamics of the cell density and the flow velocity are given by

$$\rho(r, t) = \frac{\rho_s}{1 - \left(1 - \frac{\rho_s}{\rho_i}\right)e^{-k_r t}}, \quad (\text{A.3})$$

$$\mathbf{v}(r, t) = \frac{1}{2\zeta} \left( \chi \frac{\rho(r, t) - \rho_p}{\rho_p} - P_{\text{ext}} \right) r \mathbf{e}_r. \quad (\text{A.4})$$

Here the relaxation rate is  $k_r = k_g - k_a + (P_{\text{ext}} + \chi)/\zeta$ . In the absence of cell division, apoptosis and external pressure the tissue relaxes with the rate  $\chi/\zeta$ . The cell density in

the limit of stationary growth for  $t > k_r^{-1}$  becomes a constant  $\rho_s = \rho_p(\chi + P_{\text{ext}} + \zeta(k_g - k_a))/\chi$ , where  $\rho_p$  is the reference cell density at which the pressure vanishes. During stationary growth, the pressure is given by  $P_s = P_{\text{ext}} + \zeta(k_g - k_a)$ , and the flow field is  $v = (k_g - k_a)r/2$ . The growth of the tissue radius then obeys  $\dot{R} = (k_g - k_a)R/2$ . Therefore, the system grows exponentially with cell doubling time  $t_2 = \ln 2/(k_g - k_a)$ .

## A.2 Cell division and apoptosis in the continuum limit of the discrete description

In this section, we calculate the growth rate  $k_g$  and the apoptosis rate  $k_a$  in the continuum limit from the average lifetime  $\bar{t}_L$  of a cell after which it divides with probability  $p$  and undergoes apoptosis with probability  $1 - p$ . The rates of the continuum description as well as the average cell lifetime and probability for cell division are considered to be constants.

Given  $N_0$  cells at time 0, the number of tissue cells at time  $t$  is

$$N(t) = N_0 + Z(t) - D(t). \quad (\text{A.5})$$

Here  $Z(t)$  is the total number of new cells that have been born until time  $t$  where we count one new cell for each cell division.  $D(t)$  is the total number of dead cells until time  $t$ . In the continuum limit, the change of the total number of tissue cells is thus given by  $\dot{N} = \dot{Z} - \dot{D}$ . On the other hand, the change of the total cell number of the tissue obeys  $\dot{N} = (k_g - k_a)N$  according to Eq. (2.1). Therefore the change of new cells and dead cells can be described by  $\dot{Z} = k_g N$  and  $\dot{D} = k_a N$ , respectively. From these differential equations, we can calculate the total number of new cells  $Z(t)$  and of dead cells  $D(t)$  as

$$Z(t) = N_0 \frac{k_g}{k_g - k_a} \left( e^{(k_g - k_a)t} - 1 \right), \quad (\text{A.6})$$

$$D(t) = N_0 \frac{k_a}{k_g - k_a} \left( e^{(k_g - k_a)t} - 1 \right). \quad (\text{A.7})$$

Now in order to relate the rates  $k_g$  and  $k_a$  to the average cell lifetime  $\bar{t}_L$  and the probability  $p$  for cell divisions, we calculate  $Z(t)$  and  $D(t)$  in the discrete model. As before, the tissue consists of  $N_0$  cells at time 0. After the time  $\bar{t}_L$ , there will be on average  $Z(\bar{t}_L) = pN_0$  new cells and  $D(\bar{t}_L) = (1 - p)N_0$  cells will have died. Thus the total number of cells at time  $\bar{t}_L$  is on average given by  $N(\bar{t}_L) = 2pN_0$ . Similarly, we can calculate the average total number of new and dead cells at time  $g\bar{t}_L$

$$Z(g\bar{t}_L) = N_0 \frac{p}{2p - 1} ((2p)^g - 1), \quad (\text{A.8})$$

$$D(g\bar{t}_L) = N_0 \frac{1 - p}{2p - 1} ((2p)^g - 1). \quad (\text{A.9})$$

In the continuum limit, these equations have to be equal to the expressions (A.6) and (A.7) for  $Z(t)$  and  $D(t)$  at time  $t = g\bar{t}_L$ . This leads to the relations  $k_g/(k_g - k_a) =$

$p/(2p-1)$  and  $k_g - k_a = \ln(2p)/\bar{t}_L$ , from which the Eqs. (2.11) and (2.12) as well as the relation between the effective cell doubling time  $t_2 = \ln 2/(k_g - k_a)$  and the average cell lifetime  $\bar{t}_L$  follow, see section 2.2.2.

### A.3 Numerical simulations of tissue growth

In order to solve the dynamic Eq. (2.10) numerically, we write it as

$$\bar{\eta} \sum_{j=1}^N \Lambda_{ij} \frac{d\mathbf{x}_j}{dt} = \mathbf{f}_i, \quad (\text{A.10})$$

where  $\mathbf{f}_i = -\nabla_i U(\mathbf{x}_1, \mathbf{x}_2, \dots, \mathbf{x}_N)$  is the total force acting on particle  $i$ . The matrix  $\Lambda_{ij} = n_i \delta_{ij} - m_{ij}$  is determined by the number  $n_i$  of the nearest neighbors of particle  $i$  and the matrix elements  $m_{ij}$  which are one if particle  $j$  is neighbor of particle  $i$  and zero otherwise.

All forces in Eq. (2.10) are internal forces, i.e.  $\sum_i \mathbf{f}_i = 0$ , and thus the matrix  $\Lambda_{ij}$  cannot be inverted. Therefore the motion of the center of mass  $\bar{\mathbf{x}} = (1/N) \sum_i \mathbf{x}_i$  needs to be specified. In our simulations  $\bar{\mathbf{x}}$  is fixed. Inserting  $d\mathbf{x}_1/dt = -\sum_{j=2}^N d\mathbf{x}_j/dt$  into Eq. (A.10), we get

$$\bar{\eta} \sum_{j=2}^N \tilde{\Lambda}_{ij} \frac{d\mathbf{x}_j}{dt} = \mathbf{f}_i, \quad (\text{A.11})$$

with the invertible matrix  $\tilde{\Lambda}_{ij} = \Lambda_{ij} - \Lambda_{i1}$ . With this equation, we can now calculate the velocities  $d\mathbf{x}_i/dt$  for all particles at each time step.

As parameter values, we choose for all simulations the average cell lifetime  $\bar{t}_L = 8$  h, with standard deviation  $\sigma_L = 0.5$  h, length ratios  $b/a = 1.25$ ,  $d/a = 1.75$ , cell diameter  $a = 2.6 \mu\text{m}$ ,  $|f_0/f_1| = 10$  (see Fig. 2.2), and nearest neighbor number  $n = 6$ . The spread  $\Delta\varphi$  of the division angles around the  $x$ -axis is varied in our simulations and specified in the Figs. 2.3 to 2.6. Note that the viscosity  $\bar{\eta}$  as well as the forces  $f_0$  and  $f_1$  are not themselves simulation parameters, because only the ratios  $f_0/\bar{\eta}$  and  $f_1/\bar{\eta}$  occur in the dynamic Eq. (2.10). Together with the values given here, these ratios are specified by the values for the dimensionless parameter  $\xi = \bar{\eta}a/(\bar{t}_L f_0)$ , which are given in the captions of Figs. 2.3 to 2.6. Simulations in the absence of apoptosis ( $p = 1$ ) start with a single cell at time zero. For simulations with  $p < 1$ , we start with an initial configuration of 512 cells generated by isotropic growth.

### A.4 Relation between cell movements and tissue shapes

Here we calculate how epithelium boundaries change their shapes in growing incompressible tissues if cell division is oriented. The radial distance between the center of mass of a tissue and a cell located at the tissue boundary is defined as  $R(\varphi(t), t)$ . The polar angle  $\varphi(t)$  is a function of time since it can change during development (see Fig. 2.7).

The initial angle is defined as  $\varphi_0 = \varphi(t_0)$ . The cell trajectory  $(x(t), y(t))$  is characterized by the flow velocity (2.7). It follows that  $x(t) = R_0(\varphi_0) \cos \varphi_0 \exp((k_0 + k_1)(t - t_0))$ ,  $y(t) = R_0(\varphi_0) \sin \varphi_0 \exp((k_0 - k_1)(t - t_0))$  where  $R_0$  is the initial radial distance of the cell. The radial position  $R(\varphi(t), t)$  of the boundary cell at time  $t$  can be written as

$$R(\varphi(t), t) = \frac{y(t)}{\sin \varphi(t)} = R_0(\varphi_0) e^{(k_0 - k_1)(t - t_0)} \frac{\sin \varphi_0}{\sin \varphi}. \quad (\text{A.12})$$

The polar angle describing the position of the boundary cell at time  $t$  is related to its initial value by

$$\tan \varphi = \frac{y(t)}{x(t)} = \tan(\varphi_0) e^{-2k_1(t - t_0)}, \quad (\text{A.13})$$

so that the initial angle  $\varphi_0$  obeys

$$\varphi_0 = \arctan \left( \tan(\varphi) e^{2k_1(t - t_0)} \right). \quad (\text{A.14})$$

Inserting this expression for  $\varphi_0$  into Eq. (A.12) and using the identity  $\sin(\arctan(\alpha)) = \alpha / \sqrt{1 + \alpha^2}$ , Eq. (A.12) becomes

$$R(\varphi, t) = R_0 \left( \arctan \left( \tan(\varphi) e^{2k_1(t - t_0)} \right) \right) \frac{e^{(k_0 + k_1)(t - t_0)}}{\cos \varphi \sqrt{1 + e^{4k_1(t - t_0)} \tan^2 \varphi}}, \quad (\text{A.15})$$

from which Eq. (2.14) follows.

## A.5 Shape changes of the developing *Drosophila* wing disk

In experiments performed by O. Wartlick, the shapes of wing disk boundaries have been measured at different stages during larval development. The wing disks are dissected from the larvae and visualized under the confocal microscope by DAPI stainings. In these experiments, the fluorescent molecule DAPI binds to the DNA in the nuclei of the disk cells. The molecules are excited with ultraviolet light, and their light emission at 461 nm is measured. The pictures resulting from the fluorescent microscopy are read with MATLAB software with which the boundary, the area and the center of mass of the disks are determined. For each disk, the radial distances  $R(\varphi_m, t)$  between the boundary and the center of mass are measured for the angles  $\varphi_m = m2\pi/400$  ( $m = 0, 1, \dots, 399$ ). The disks are oriented such that  $R(\pi/2, t)$  is the longest distance.

Unfortunately, the growth of an individual disk cannot be visualized in vivo, because the disks die about one hour after dissection. Hence one has to measure the shapes of different wing disks of varying ages. In Fig. A.1, the area  $A$  of the disks is plotted logarithmically as a function of disk age. For our analysis, we consider only those disks with lifetimes between  $t_0 = 24$  h and  $t_f = 66$  h, when the area grows exponentially as indicated by the red fit curves.

We have quantified the effective growth rate  $k_{\text{eff}}(\varphi_m)$  of the wing disk along the angle  $\varphi_m$  by a simple phenomenological description. Since we focus on the exponential growth

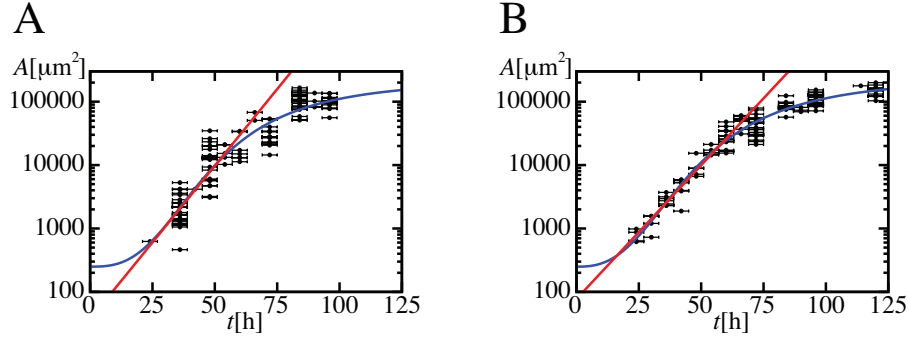


Figure A.1: Growth of the *Drosophila* wing disk during development. (A,B) Area growth of wildtype (WT) (A) and GFP-Dpp wing disks (B). The area  $A$  of 119 individual WT and 126 GFP-Dpp disks is plotted logarithmically as a function of larval age (in hours after hatching). The blue curves represent fits of the function  $A(t) = A_0 \exp(at^q/(\tau^q + t^q))$  to the data, using  $a$ ,  $\tau$ , and  $q$  as fit parameters. The initial area  $A_0$  can be estimated by  $A_0 = 250 \mu\text{m}^2$  by analyzing pictures of the wing disk at this early stage [16]. The red curves are exponential fits to the data points of 56 WT and 49 GFP-Dpp disks between the ages  $t_0 = 24$  h and  $t_f = 66$  h. The fits show that the area of both WT and GFP-Dpp disks grows exponentially by about two orders of magnitude during the time interval  $[t_0, t_f]$ .

phase of the disk, we describe the radial position  $R(\varphi_m, t)$  of the disk boundary at each angle  $\varphi_m$  by the ansatz

$$R(\varphi_m, t) = R_0(\varphi_m) \exp(k_{\text{eff}}(\varphi_m)(t - t_0)). \quad (\text{A.16})$$

Here  $R_0(\varphi_m)$  is the initial radius at time  $t_0$  and angle  $\varphi_m$ . For each of the 400 angles  $\varphi_m$ , we fit the logarithm of Eq. (A.16) to the logarithms of the measured radii  $R(\varphi_m, t)$ , using  $R_0(\varphi_m)$  and  $k_{\text{eff}}(\varphi_m)$  as fit parameters. The best fit parameters for  $k_{\text{eff}}(\varphi_m)$  are plotted in Fig. 2.9. The average initial disk shape is approximated by the truncated Fourier series  $R_0^F(\varphi) = a_0/2 + \sum_{i=1}^{20} (a_i \cos(i\varphi) + b_i \sin(i\varphi))$ , which is fitted to  $R_0(\varphi_m)$  with the fit parameters  $a_i$  and  $b_i$  ( $i = 1, \dots, 20$ ).





## Appendix B

# The Dpp gradient in the growing wing disk

In this chapter, we present several aspects of the dynamics of Dpp spreading in the growing wing disk. We show how Dpp transport is described from the view of a moving and proliferating cell. Then we calculate the steady state of the diffusion-advection equation (3.8) that describes Dpp transport in the growing disk. Furthermore, we present simulations of the feedback between the Dpp concentration and the tissue growth rate if growth is controlled by the relative rate of change of the cellular Dpp concentration as discussed in section 3.4. Finally, we discuss the measurements of P-Mad gradients in the wing disk.

### B.1 Coordinate transformation of the Dpp transport equation

In section 3.2.1, we have derived the transport equation for the morphogen Dpp in the growing *Drosophila* wing disk. Here we perform a coordinate transformation into a growing system to get the transport equation from the view of the proliferating and moving cells.

The coordinate transformation from the static system  $S$  in which cell rearrangements are described by the flow velocity (2.7) into the growing system  $\tilde{S}$  in which the disk seems to be static is characterized by the position vector  $\tilde{\mathbf{r}}$  which is given by

$$\begin{pmatrix} \tilde{x} \\ \tilde{y} \end{pmatrix} = \begin{pmatrix} x \exp\left(-\int_{t_i}^t dt' k_x(t')\right) \\ y \exp\left(-\int_{t_i}^t dt' k_y(t')\right) \end{pmatrix}, \quad (\text{B.1})$$

where  $t_i$  denotes the age of the larva when the disk starts to grow. The Dpp concentration in the growing system is defined as  $\tilde{c}(\tilde{\mathbf{r}}, t) = c(\mathbf{r}, t)$ . The derivatives of  $\tilde{c}$  in time and space are thus given by  $\partial_t c = \partial_t \tilde{c} - k_x x e^{-\int_{t_i}^t dt' k_x(t')} \partial_{\tilde{x}} \tilde{c} - k_y y e^{-\int_{t_i}^t dt' k_y(t')} \partial_{\tilde{y}} \tilde{c}$ ,  $\partial_x c = e^{-\int_{t_i}^t dt' k_x(t')} \partial_{\tilde{x}} \tilde{c}$ ,  $\partial_y c = e^{-\int_{t_i}^t dt' k_y(t')} \partial_{\tilde{y}} \tilde{c}$ ,  $\partial_x^2 c = e^{-2\int_{t_i}^t dt' k_x(t')} \partial_{\tilde{x}}^2 \tilde{c}$ , and  $\partial_y^2 c =$

$e^{-2 \int_{t_i}^t dt' k_y(t')} \partial_{\tilde{y}}^2 \tilde{c}$ . Here the derivative  $\partial_t \tilde{c}$  denotes the time derivative of  $\tilde{c}$  at fixed position  $\tilde{\mathbf{r}}$  within the growing coordinate system. Inserting these expressions into the Dpp transport equation (3.7) and using  $c(\mathbf{r}, t) \approx c(x, t)$  due to the symmetry of the problem (see section 3.1.1), we get

$$\begin{aligned} \partial_t \tilde{c}(\tilde{x}, t) = & D(t) \exp\left(-2 \int_{t_i}^t dt' k_x(t')\right) \partial_{\tilde{x}}^2 \tilde{c}(\tilde{x}, t) - (k(t) + k_g(t)) \tilde{c}(\tilde{x}, t) \\ & + \nu(t) \Theta(-\tilde{x}) \Theta\left(\tilde{x} + w(t) \exp\left(-\int_{t_i}^t dt' k_x(t')\right)\right). \end{aligned} \quad (\text{B.2})$$

We find that in the growing coordinate system, the Dpp transport equation does not contain the stretching term  $-k_x x \partial_x c$  as in the case of the static coordinate system, see Eq. (3.8). However, the diffusion coefficient and the width of the Dpp source are modified. How can we interpret these findings? An observer in the growing system  $\tilde{S}$  neither observes growth nor movement of the cells. From the view of the static system  $S$ , this observer moves with the cells that carry Dpp molecules with themselves. Hence the observer does not see a stretching of the gradient. However, the observer in the growing coordinate system observes a decreasing diffusion coefficient because due to tissue growth, the time it takes for molecules to diffuse between two points  $\tilde{x}_1$  and  $\tilde{x}_2$  in the growing system  $\tilde{S}$  increases during development as their distance increases in the static system  $S$ . Similarly, the source shrinks from the view of this observer, because it grows slower than the tissue within the static coordinate system (see section 3.3.1).

In section 3.3.2, we have shown that the Dpp concentration profile during development can be well described as a succession of steady-state gradients. In this approximation, the adiabatically changing steady state of Eq. (B.2) for  $x > 0$  is given by

$$\tilde{c}(\tilde{x}, t) = \frac{\nu}{2k} \left(1 - \exp\left(-\frac{w}{\lambda}\right)\right) \exp\left(-\frac{\tilde{x} e^{\int_{t_i}^t dt' k_x(t')}}{\lambda}\right). \quad (\text{B.3})$$

Using the definition  $\tilde{c}(sl_0, t) = c_{\text{mov}}(s, t)$ , this expression for the cellular Dpp concentration can be identified with Eq. (3.14).

## B.2 Steady state of the diffusion equation with drift term

In this section, we calculate the steady state of the 1d Dpp transport equation (3.8) for fixed values of the parameters  $D$ ,  $k$ ,  $\nu$ ,  $w$ ,  $k_x$  and  $k_g$ . We thus have to solve Eq. (3.9), for which we have imposed the following boundary conditions: (i)  $c(x) \rightarrow 0$  for  $x \rightarrow \pm\infty$ , (ii)  $c$  continuous at  $x = 0$ , (iii)  $j = -D\partial_x c + k_x x c$  and thus  $\partial_x c$  continuous at  $x = 0$ , (iv)  $c$  continuous at  $x = -w$ , and finally (v)  $\partial_x c$  continuous at  $x = -w$ .

First of all, we can identify the homogeneous part of Eq. (3.9) with the general confluent equation [2]

$$w'' + \left(\frac{2A}{x} + \frac{bh'}{h} - h' - \frac{h''}{h'}\right) w' + \left(\left(\frac{bh'}{h} - h' - \frac{h''}{h'}\right) \frac{A}{x} + \frac{A(A-1)}{x^2} - \frac{ah'^2}{h}\right) w = 0, \quad (\text{B.4})$$

choosing  $w(x) = c(x)$ ,  $h(x) = \frac{k_x}{2D}x^2$  and either (1)  $A = 0$ ,  $a = \frac{k+k_g}{2k_x}$  and  $b = 1/2$ , or (2)  $A = -1$ ,  $a = \frac{k+k_g}{2k_x} + 1/2$  and  $b = 3/2$ . The two linear independent solutions of Eq. (B.4) are  $w(x) = x^{-A}F(a, b, h(x))$  and  $w(x) = x^{-A}Q(a, b, h(x))$ , where  $F(a, b, z) \equiv {}_1F_1(a, b, z)$  is the confluent hypergeometric function, and  $Q(a, b, z) = F(a, b, z) - z^{1-b} \frac{\Gamma(1+a-b)\Gamma(b)}{\Gamma(a)\Gamma(2-b)} \times F(1+a-b, 2-b, z)$ . With the above choices of the function  $h(x)$  and the parameters  $A$ ,  $a$  and  $b$ , we find the two linear independent solutions  $c(x) = Q\left(\frac{k+k_g}{2k_x}, \frac{1}{2}, \frac{k_x}{2D}x^2\right)$  and  $c(x) = xF\left(\frac{k+k_g}{2k_x} + \frac{1}{2}, \frac{3}{2}, \frac{k_x}{2D}x^2\right)$  of the homogeneous part of Eq. (3.9). For  $-w \leq x \leq 0$ , a special solution of the inhomogeneous equation (3.9) is given by  $c(x) = \frac{\nu}{k+k_g}$ . The general solution of Eq. (3.9) can thus be written as

$$c(x) = \begin{cases} C_1 Q\left(\frac{k+k_g}{2k_x}, \frac{1}{2}, \frac{k_x}{2D}|x|^2\right) + C_4 x F\left(\frac{k+k_g}{2k_x} + \frac{1}{2}, \frac{3}{2}, \frac{k_x}{2D}x^2\right) & x \leq -w \\ C_2 Q\left(\frac{k+k_g}{2k_x}, \frac{1}{2}, \frac{k_x}{2D}x^2\right) + C_5 x F\left(\frac{k+k_g}{2k_x} + \frac{1}{2}, \frac{3}{2}, \frac{k_x}{2D}x^2\right) + \frac{\nu}{k+k_g} & -w \leq x \leq 0. \\ C_3 Q\left(\frac{k+k_g}{2k_x}, \frac{1}{2}, \frac{k_x}{2D}x^2\right) + C_6 x F\left(\frac{k+k_g}{2k_x} + \frac{1}{2}, \frac{3}{2}, \frac{k_x}{2D}x^2\right) & x \geq 0 \end{cases} \quad (\text{B.5})$$

For  $x \leq -w$ , we chose the function  $Q\left(\frac{k+k_g}{2k_x}, \frac{1}{2}, \frac{k_x}{2D}|x|^2\right) = Q\left(\frac{k+k_g}{2k_x}, \frac{1}{2}, \frac{k_x}{2D}x^2\right) + 2xq \times F\left(\frac{k+k_g}{2k_x} + \frac{1}{2}, \frac{3}{2}, \frac{k_x}{2D}x^2\right)$  with  $q = \sqrt{2k_x/D} \Gamma\left(\frac{k+k_g}{2k_x} + \frac{1}{2}\right) / \Gamma\left(\frac{k+k_g}{2k_x}\right)$  as one of the two linear independent solutions of Eq. (3.9), which will be useful to satisfy the boundary conditions.

We now have to specify the constants  $C_1, \dots, C_6$  such that the boundary conditions (i)-(v) are fulfilled. For condition (i), we need to study the asymptotic behavior of Eq. (B.5). Using  $F(a, b, z) = \Gamma(b)/\Gamma(a) e^z z^{a-b} (1 + O(z^{-1}))$  and  $Q(a, b, z) = \sin(\pi b)/\pi \Gamma(b)\Gamma(1+a-b) z^{-a} (1 + O(z^{-1}))$  for  $z \rightarrow \infty$  (see e.g. [2]), as well as  $\lim_{x \rightarrow -\infty} Q\left(\frac{k+k_g}{2k_x}, \frac{1}{2}, \frac{k_x}{2D}|x|^2\right) = \lim_{x \rightarrow \infty} Q\left(\frac{k+k_g}{2k_x}, \frac{1}{2}, \frac{k_x}{2D}x^2\right)$ , we can conclude that

$$C_4 = 0 \quad \text{and} \quad C_6 = 0. \quad (\text{B.6})$$

With the formula  $F(a, b, 0) = 1 \forall a, b > 0$  and thus  $Q\left(\frac{k+k_g}{2k_x}, \frac{1}{2}, 0\right) = 1$ , the boundary condition (ii) implies that

$$C_3 = C_2 + \frac{\nu}{k+k_g}. \quad (\text{B.7})$$

Next we consider the first derivatives of the functions  $F$  and  $Q$  to study boundary condition (iii). Using  $\partial_x F(a, b, cx^2) = 2cxa/b F(a+1, b+1, cx^2)$  and  $\partial_x Q(a, b, cx^2) = -2cxa/b \sin(\pi b)/\sin(\pi(b+1)) Q(a+1, b+1, cx^2)$ , it follows that  $\partial_x Q\left(\frac{k+k_g}{2k_x}, \frac{1}{2}, \frac{k_x}{2D}x^2\right) \Big|_{x=0} = -q$ . Condition (iii) hence implies that  $-C_2q + C_5 = -C_3q$ , and thus

$$C_5 = -\frac{\nu}{k+k_g} q. \quad (\text{B.8})$$

Let us now determine the remaining constants  $C_1$  and  $C_2$  with the help of the boundary

conditions (iv) and (v). The continuity of the Dpp concentration at  $x = -w$  (iv) yields

$$C_1 = C_2 \left( 1 + \frac{2qwF\left(\frac{k+k_g}{2k_x} + \frac{1}{2}, \frac{3}{2}, \frac{k_x}{2D}w^2\right)}{Q\left(\frac{k+k_g}{2k_x}, \frac{1}{2}, \frac{k_x}{2D}w^2\right)} \right) + \frac{\nu}{k+k_g} \frac{1 + qwF\left(\frac{k+k_g}{2k_x} + \frac{1}{2}, \frac{3}{2}, \frac{k_x}{2D}w^2\right)}{Q\left(\frac{k+k_g}{2k_x}, \frac{1}{2}, \frac{k_x}{2D}w^2\right)}. \quad (\text{B.9})$$

And finally, we specify  $C_2$  by using the boundary condition (v). After a rather lengthy calculation in which we apply the identities already used above, one finds

$$\begin{aligned} C_2 = \frac{\nu}{k+k_g} & \left[ \left[ (k+k_g)wF\left(\frac{k+k_g}{2k_x} + 1, \frac{3}{2}, \frac{k_x}{2D}w^2\right) - DqF\left(\frac{k+k_g}{2k_x} + \frac{1}{2}, \frac{3}{2}, \frac{k_x}{2D}w^2\right) \right. \right. \\ & \left. \left. - \frac{k+k_g+k_x}{3}qw^2F\left(\frac{k+k_g}{2k_x} + \frac{3}{2}, \frac{5}{2}, \frac{k_x}{2D}w^2\right) \right] \right. \\ & \left. \left/ \left[ -2q(k+k_g)w^2F\left(\frac{k+k_g}{2k_x} + 1, \frac{3}{2}, \frac{k_x}{2D}w^2\right)F\left(\frac{k+k_g}{2k_x} + \frac{1}{2}, \frac{3}{2}, \frac{k_x}{2D}w^2\right) \right. \right. \right. \\ & \left. \left. + 2F\left(\frac{k+k_g}{2k_x}, \frac{1}{2}, \frac{k_x}{2D}w^2\right) \left( DqF\left(\frac{k+k_g}{2k_x} + \frac{1}{2}, \frac{3}{2}, \frac{k_x}{2D}w^2\right) \right. \right. \right. \\ & \left. \left. \left. + \frac{k+k_g+k_x}{3}qw^2F\left(\frac{k+k_g}{2k_x} + \frac{3}{2}, \frac{5}{2}, \frac{k_x}{2D}w^2\right) \right) \right] - \frac{1}{2} \right]. \quad (\text{B.10}) \end{aligned}$$

We can summarize that the Dpp concentration in steady state for given values of the parameters  $D$ ,  $k$ ,  $\nu$ ,  $w$ ,  $k_x$  and  $k_g$  is described by Eq. (3.10) with the constants  $C_1$ ,  $C_2$  and  $C_3$  given in the Eqs. (B.7), (B.9), and (B.10).

### B.3 The feedback between concentration and growth rate

In this section, we discuss numerical simulations of the feedback between the Dpp concentration and the growth rate in the wing disk, see section 3.4. In these simulations, we solve the one dimensional diffusion-advection equation (3.8) which describes Dpp transport in the growing wing disk, and we calculate the cellular Dpp concentration via  $\dot{c}_{\text{mov}} = \dot{c} + v_x \partial_x c$ . We put in the parameters  $D(t)$ ,  $k(t)$ ,  $\nu(t)$ , and  $w(t)$  that have been determined experimentally, see section 3.3.1. With the onset of Dpp production at time  $t_i = 28.4$  h, we start tissue growth. Until the disk age  $t_{\text{on}} = 100$  h, we use the growth rate  $k_x(t) = \dot{l}(t)/l(t)$ , putting in the fit of the measured length  $l(t)$  of the posterior disk compartment, and we consider  $k_g(t) = 2k_x(t)$  throughout development. When the larva has reached the age  $t_{\text{on}} = 100$  h, we determine the growth rate by our rule  $k_g(x, t) = \alpha\gamma(x/l(t), t) + \beta$ . Thus  $k_g$  will now be a function of space and time, and we calculate the flow velocity by  $v_x = \frac{1}{2} \int_0^x dx' k_g(x', t)$ .

So on the one hand,  $k_g(x, t)$  depends on the cellular Dpp concentration  $c_{\text{mov}}(x, t)$ , and on the other hand,  $c_{\text{mov}}(x, t)$  depends on  $k_g(x, t)$ . In order to solve this feedback problem, we use the following algorithm. Given that we know at time  $t$  the Dpp concentration  $c$  and the growth rate  $k_g$  at all positions in the tissue, and thus the cell velocity  $v_x =$

$\frac{1}{2} \int_0^x dx' k_g(x', t)$ , the spacial derivatives  $\partial_x c$  and  $\partial_x^2 c$ , as well as the Dpp flux  $j = -D\partial_x c + v_x c$  and its derivative  $del_x j$ , we can determine the dynamics of Dpp transport and tissue growth iteratively: (i) We calculate the time derivative of the Dpp concentration at time  $t$  by Eq. (3.8), so that  $\dot{c}$  is some function  $f_1$  that depends on the known values  $c(x, t)$ ,  $\partial_x j(x, t)$ , and  $k_g(x, t)$ , i.e. we can write  $\dot{c}(x, t) = f_1(c(x, t), \partial_x j(x, t), k_g(x, t))$ . (ii) The time derivative of the cellular Dpp concentration at time  $t$  is determined by  $\dot{c}_{\text{mov}} = \dot{c} + v_x \partial_x c$ , and thus  $\dot{c}_{\text{mov}}$  can be expressed as  $\dot{c}_{\text{mov}} = f_2(\partial_x c(x, t), \dot{c}(x, t), v_x(x, t))$ . (iii) The Dpp concentration at time  $t + \Delta t$  is calculated by  $c(x, t + \Delta t) = c(x, t) + \Delta t \dot{c}(x, t)$ , and hence  $c(x, t + \Delta t) = f_3(c(x, t), \dot{c}(x, t))$ . (iv) Since we do not know the time derivative  $\dot{c}_{\text{mov}}$  of the cellular Dpp concentration at time  $t + \Delta t$ , we need to calculate  $k_g$  explicitly as

$$k_g = \alpha \left( \frac{D\partial_x^2 c}{c} - (k + k_g) + \frac{\nu}{c} \Theta(-x) \Theta(x + w) \right) + \beta, \quad (\text{B.11})$$

and therefore, the growth rate at time  $t + \Delta t$  and position  $x$  in the wing disk is given by

$$k_g = \frac{1}{1 + \alpha} \left( \beta + \alpha \left( \frac{D\partial_x^2 c}{c} - k + \frac{\nu}{c} \Theta(-x) \Theta(x + w) \right) \right). \quad (\text{B.12})$$

Hence we can write  $k_g$  as  $k_g(x, t + \Delta t) = f_4(c(x, t + \Delta t), \partial_x^2 c(x, t + \Delta t))$ , where  $\partial_x^2 c(x, t + \Delta t)$  can be calculated from  $c(x, t + \Delta t)$  for all positions in the tissue. (v) From  $k_g$ , we can now determine the cell velocity  $v_x = \frac{1}{2} \int_0^x dx' k_g(x', t + \Delta t)$  at time  $t + \Delta t$ , i.e.  $v_x(x, t + \Delta t) = f_5(k_g(x, t + \Delta t))$ , and finally (vi), we calculate the Dpp flux at time  $t + \Delta t$  by  $j(x, t + \Delta t) = -D(t) \partial_x c(x, t + \Delta t) + v_x(x, t + \Delta t) c(x, t + \Delta t)$ , so that  $j(x, t + \Delta t) = f_6(c(x, t + \Delta t), \partial_x c(x, t + \Delta t), v_x(x, t + \Delta t))$ . By that, the functions  $f_1$  to  $f_6$  are well defined and depend only on quantities that have been calculated before.

In Fig. B.1, A the length of the simulated wing disk is plotted logarithmically as a function of time in comparison to the experimental data and the corresponding fit curve described in section 3.3.1. We find that after the onset of growth control by the relative rate of change of the cellular Dpp concentration at time  $t_{\text{on}} = 100$  h, the simulated growth of the tissue length matches the fit to the experimental data perfectly. Fig. B.1, B shows the comparison between the simulated growth rate  $k_g = 2k_x$  and  $2k_x = 2\dot{l}/l$  determined from the fit to the experimental data in Fig. B.1, A as functions of time. With the onset of our growth rule, the simulated growth rate starts to depend on position within the tissue. However, this position dependence of the growth rate is rather small in agreement with the observed weak position dependences of the growth rate [44].

We then studied whether we could start growth control by Dpp with our rule at earlier times. Fig. B.1, C and D shows the results of a simulation in which growth control by the relative rate of change of the cellular Dpp concentration is initiated at time  $t_{\text{on}} = 80$  h. Still, there is hardly any difference between the simulated tissue length as a function of time and the fit to the experimental data, see Fig. B.1, C. However, the position dependence of the growth rate plotted in Fig. B.1, D increases significantly compared to the simulation in which growth control by  $\gamma$  was started at time  $t_{\text{on}} = 100$  h. Between the larval ages  $t = 80$  h and  $t = 120$  h, the growth rate in our simulation shows a variation of up to a factor of about 3 between different positions in the tissue.

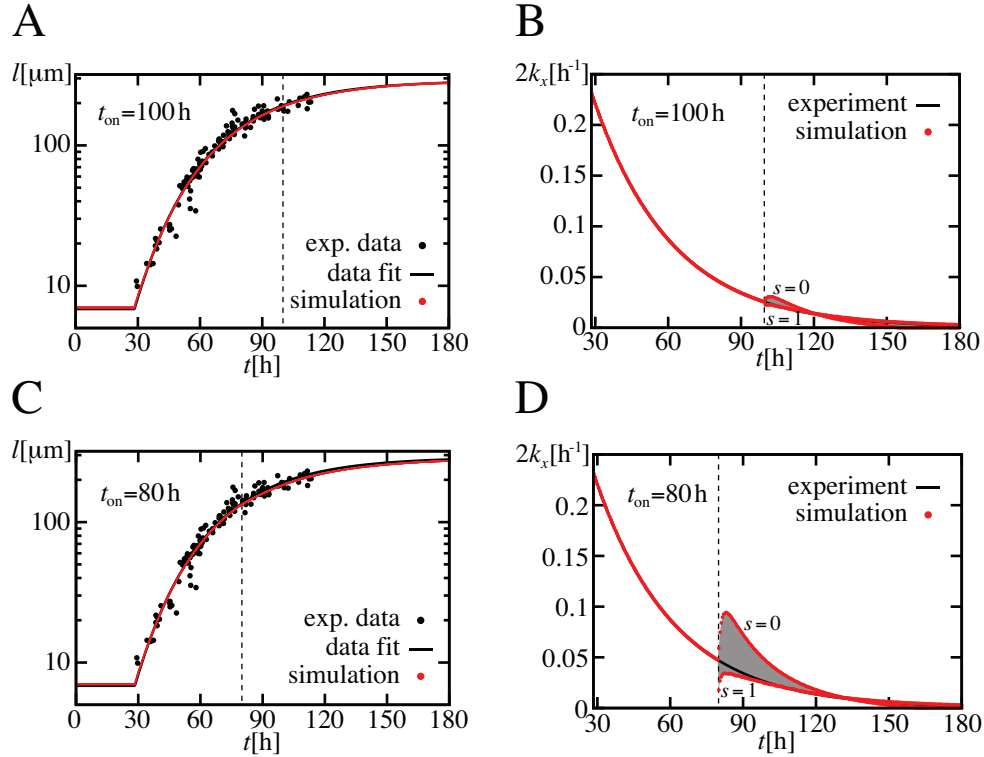


Figure B.1: Simulated growth of the wing disk with onset of growth control by Dpp at larval age  $t_{\text{on}} = 100$  h (A,B) and  $t_{\text{on}} = 80$  h (C,D). (A,C) Length of the posterior compartment as a function of larval age. In these logarithmic plots, the growth of the length of the simulated tissues is compared to the measured data and the corresponding fit curve (see Fig. 3.4, D). (B,D) Tissue growth rate as a function of larval age. The simulated growth rate is displayed as red dots for the positions  $x_s(t) = sl(t)$  in the tissue with  $s = 0$  (boundary of the Dpp source) and  $s = 1$  (boundary of the disk). The gray regions between these curves represent the simulated growth rates for all other positions in the receiving tissue,  $0 < s < 1$ . The growth rate  $2k_x(t) = 2\dot{l}(t)/l(t)$  with  $l(t)$  taken from the fit to the experimental data in A and C is plotted in black. The dashed lines indicate the time  $t_{\text{on}}$  at which growth control via the relative rate of change of the cellular Dpp concentration is initiated in our simulations.

If we decrease the time  $t_{\text{on}}$  even further, the position dependence of the growth rate increases further, and moreover the simulated growth of the tissue length starts to vary significantly from the fit of the measured data. The reason for the increasing position dependence of the growth rate is that the relative rate of change  $\gamma$  of the cellular Dpp concentration becomes more and more position dependent at larval ages before  $t = 100$  h, see Fig. 3.9, B. And since the relation between  $2k_x$  and  $\bar{\gamma}$  becomes ambiguous if we take larval ages before  $t = 100$  h into account (see Fig. 3.9, C), the experimentally measured

growth of the tissue length cannot be reproduced by our feedback simulations for the whole development.

## B.4 Measurements of P-Mad gradients in the wing disk

In immunostaining experiments performed by A. Kicheva [56], P-Mad molecules in the cell nuclei in the wing disk are labeled fluorescently. The fluorescence intensity is recorded with a confocal microscope and quantified, see Fig. 3.10, A. The experiments are done in “GFP-Dpp rescue disks”, in which only GFP-Dpp but no endogenous Dpp is produced [20]. The growth of these disks and the Dpp dynamics during development are in well agreement with the dynamics of GFP-Dpp disks.

Unfortunately, there is no straightforward way to calibrate the fluorescence intensity of immunostained proteins to concentration in molecules/ $\mu\text{m}^2$ . One such attempt has so far been reported in the literature [46], but in the case of P-Mad this would require having a P-Mad-GFP fusion, where the protein is fluorescent only when phosphorylated, which does not exist. Nevertheless, we are mainly interested in the relative rate of change  $\sigma$  of the cellular P-Mad concentration, and we have ensured that the fluorescence intensity is related linearly to the P-Mad concentration. Since we can only reliably compare fluorescence intensities in disks of the same immunostaining, we have used the biggest data set for our analysis of  $P_0$ , see Fig. 3.10, C. However, the decay length of the P-Mad gradients is independent of the absolute fluorescence intensity, so that we can compare the data of different stainings for  $\lambda_p$ , see Fig. 3.10, B.





## Appendix C

# Kinetics of cellular signaling

### C.1 Fit of the microscopic description to the FRAP curves

As explained in section 4.2, we fit the double exponential Eq. (4.5) to the FRAP curves (see Fig. 4.3), using  $A$ ,  $B$ ,  $k_{\text{out}}$  and  $k'_{\text{out}}$  as fit parameters and the constraint that the fit parameters  $k_{\text{out}}$  and  $k'_{\text{out}}$  are the same for all three experimental conditions (control,  $K^+$  and  $\text{Tkv}^{\text{QD}}$ ). In principle, this leads to three different values  $A_1, A_2, A_3$  and  $B_1, B_2, B_3$  of the fit parameters  $A$  and  $B$ , respectively, which correspond to the three different mutant conditions. Thus, if we include  $k_{\text{out}}$  and  $k'_{\text{out}}$ , there are in total eight fit parameters for the three recovery curves. Since we assume that the quantities  $X$ ,  $Y$  and  $Y'$  have the same values for all these mutant conditions and that only  $Z$  differs, additional constraints for the six values  $A_i$  and  $B_i$  are imposed. According to Eqs. (4.2), they can be expressed as

$$\begin{aligned} X &= \frac{1 - A_i - B_i}{B_i} \\ Y' &= \frac{Y B_i}{Y c_{\text{tot},i}^s / n_{\text{tot},i}^s - A_i}, \end{aligned} \tag{C.1}$$

where  $i = 1, 2$  or  $3$  corresponds to the three mutant conditions. The ratio  $c_{\text{tot},i}^s / n_{\text{tot},i}^s$  is measured independently in the steady state except for the  $K^+$  condition for which the measured value is unreliable and thus used as an additional fit parameter as discussed below. Considering these constraints, we effectively reduce the number of free fit parameters by replacing the six parameters  $A_i$  and  $B_i$  by the parameters  $X$ ,  $Y$  and  $Y'$ . From the fit of the experimental data, we hence obtain the values for  $k_{\text{out}}$  and  $k'_{\text{out}}$ ,  $X$ ,  $Y$  and  $Y'$ . Using the constraints given in Eqs. (C.1), we can determine all six corresponding values  $A_i$  and  $B_i$ . The values of the quantity  $Z = k_p / k_d$  for the three mutant conditions are determined according to the Eqs. (4.2)

$$Z_i = \frac{Y c_{\text{tot},i}^s}{A_i n_{\text{tot},i}^s} - 1. \tag{C.2}$$

Here, the three different values of  $Z_i$  correspond to changes in the phosphorylation rate  $k_p$  for the three different conditions.

From the fits of the single exponential Eq. (4.8), we determine the average nuclear mobile and thus immobile fractions and the effective nuclear export rates. From Eq. (4.6) it follows that

$$k_i = mk_e n_{\text{tot}}^s / c^s, \quad (\text{C.3})$$

where  $c^s$  is the cytosolic concentration in the steady state. Using the measured ratio  $n_{\text{tot}}^s / c^s$ , we can thus also calculate the effective nuclear import rates.

The effective import rates in the phenomenological model and some of the parameters (specific import rates, ratios of exchange rates, and pool sizes) in the specific microscopic description are calculated with the ratios  $c_{\text{tot}}^s / n_{\text{tot}}^s$  (see Eqs. (C.1), (C.2), and (C.3)). In the case of control and  $\text{TkV}^{\text{QD}}$  experiments, these concentrations can be determined experimentally and correspond to the average fluorescence in the cytosol and nucleus before the FRAP experiment. However, this is not true for the  $\text{K}^+$  stimulation experiment. In this case, before stimulation, the system is in the steady state corresponding to the control. The bleaching of the fluorescence occurs 2 minutes after initiation of the  $\text{K}^+$  stimulation, and therefore the system did not have enough time to relax from the control steady state to a new steady state caused by the stimulation. Thus, our experimental estimates of the steady-state values of the total nuclear and cytosolic Mad concentrations under this condition is unreliable. Therefore, we have used the value of  $c_{\text{tot}}^s / n_{\text{tot}}^s$  in the  $\text{K}^+$  condition as an additional fit parameter in the specific model that reflects the fact that its measured value might be incorrect. With this procedure, we find  $c_{\text{tot}}^s / n_{\text{tot}}^s = 0.22$  in the  $\text{K}^+$  condition, while the measured value is about 0.31. This difference confirms that for this condition, the measured value is unreliable. Indeed, this measured value does not lead to a reasonable fit of the fluorescence recovery to the experimental data. Taken together, the values for the rates obtained in the  $\text{K}^+$  condition should serve only as an indication that the signaling state during stimulation is different than in its absence, rather than as a quantitative assessment of the levels of signaling.

## C.2 The immobile nuclear Mad pool

The immobile fraction of the total nuclear Mad concentration in the FRAP experiments (see Fig. 4.3) reveals the existence of two different kinds of kinetics: fast kinetics between one part of the nuclear concentration (the mobile nuclear fraction) and the cytosol which recovers within the time scale of the experiment of about 1000 seconds, and slow kinetics of the other part of the nuclear concentration (the immobile nuclear fraction) which takes a much longer time to recover.

In order to address whether the immobile pool consists of Mad molecules bound to a static structure inside the nucleus like the DNA, FRAP experiments were performed in which the fluorescence of a small region within the nucleus was bleached and its recovery kinetics was followed for a short period of time (up to 200 seconds), see Fig. C.1. By the analysis of the fluorescence recovery of a smaller region with respect to the whole nucleus, we can distinguish between the flow of molecules into/out of the nucleus and the movement of fluorescent molecules within the nucleus. The experiment shows that

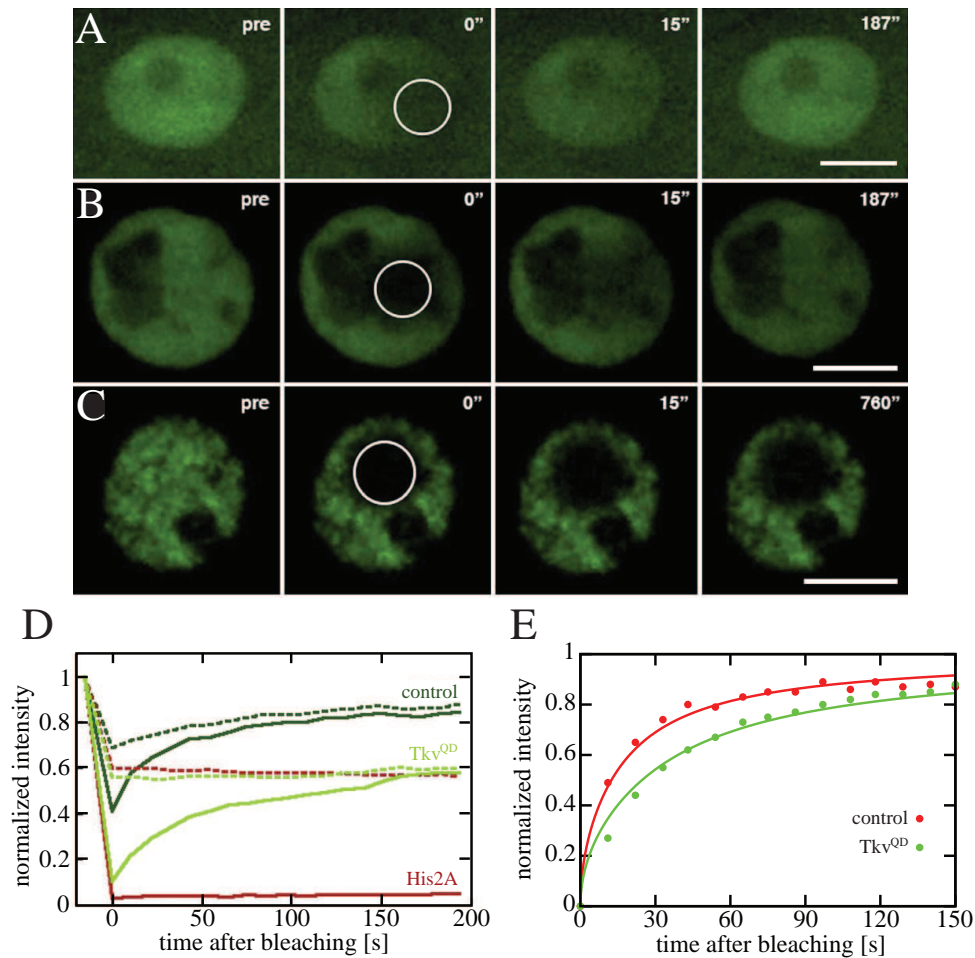


Figure C.1: FRAP experiments in a small region within the nucleus of a muscle cell. (A-C) Time-lapse images of the FRAP experiments. The images show the fluorescent signal of GFP-Mad in control (A) and  $Tkv^{QD}$  flies (B), and of GFP-Histone2A (C) with which the chromatin is marked. Images are displayed before (pre) bleaching the small spot within the nucleus (indicated by a circle), immediately after bleaching (0''), and during the recovery phase 15 and 187 respectively 760 seconds after the start of the experiment. The scale bar equals  $10 \mu\text{m}$ . (D) Averaged FRAP curves for control ( $n = 9$  experiments),  $Tkv^{QD}$  ( $n = 9$ ) and Histone2A animals ( $n = 2$ ). The solid and dashed lines represent the average fluorescence within the bleached region and of the whole nucleus, respectively, normalized to their values before bleaching as functions of time. (E) Averaged FRAP curves for control ( $n = 9$ ) and  $Tkv^{QD}$  flies ( $n = 9$ ). The measured average fluorescence within the bleached region normalized to changes in the total nuclear fluorescence, to the pre-bleach value, and to zero immediately after bleaching is plotted as a function of time after bleaching. The solid lines represent fits of the function  $f_s(t)$  to the data. Figures A-D modified from [33].

both the control (see Fig. C.1, A) and  $\text{TkV}^{\text{QD}}$  (see Fig. C.1, B) recover to the total nuclear concentration, see Fig. C.1, D. The fluorescence recovery in the bleached region could hence be explained either by the movement of the chromatin inside the nucleus together with the bound immobile pool of Mad molecules, or by the free movement of the immobile pool of Mad molecules inside the nucleus. In order to distinguish between these two possibilities, we performed the same FRAP experiment with a fluorescently labeled histone protein which associates to the chromosome, see Fig. C.1, C. In this experiment, the fluorescence does not recover within the bleached region (see Fig. C.1, C and D) which is consistent with the idea that the chromosomes are stationary in interphase nuclei. Therefore, the immobile pool of Mad molecules moves freely within the nucleus. To account for the immobile fraction of the FRAP experiments of bleaching the whole nucleus, these molecules are confined inside the nucleus, for example by binding to other proteins so that these complexes cannot leave the nucleus through the nuclear pores, and exchange with the mobile nuclear pool with slow kinetics.

Moreover the FRAP experiments of bleaching only a small area within the nucleus allowed us to determine the diffusion coefficient for the movement of Mad molecules inside the nucleus. For this purpose, the recovery curves for the spot data are first normalized to changes in the total nuclear fluorescence per unit volume after bleaching to exclude the effective import of molecules from the cytosol, and second the data is normalized to zero after bleaching and to one for the initial value of the total fluorescence per unit volume. The shape of the nucleus and of the bleached region is approximated by a cylinder. Moreover we assume that the bleached spot is positioned in the center of the nucleus so that the problem is invariant in the  $z$ -direction. Hence it can be simplified to the situation of bleaching a circle in a plane. For an infinitely large plane, the recovery of the normalized fluorescence in the small spot is described by [89]

$$f_s(t) = e^{-2\tau_D/t} (I_0(2\tau_D/t) + I_1(2\tau_D/t)), \quad (\text{C.4})$$

where  $I_0$  and  $I_1$  are modified Bessel functions [2],  $\tau_D = r_b^2/(4D)$ ,  $r_b$  is the radius of the bleached area, and  $D$  is the diffusion coefficient. We fit this function to the normalized data (see Fig. C.1, E), using  $r_b = 3.34 \mu\text{m}$  as an input and  $D$  as a fit parameter. For control flies, we determine the diffusion coefficient  $D = 0.20 \pm 0.01 \mu\text{m}^2/\text{s}$  for the nuclear Mad, whereas we find  $D = 0.11 \pm 0.01 \mu\text{m}^2/\text{s}$  in  $\text{TkV}^{\text{QD}}$  mutant flies.

How can we explain this difference in the diffusion coefficient in control and  $\text{TkV}^{\text{QD}}$  flies? In the scenario proposed above, we explained the free movement of the immobile pool inside the nucleus by P-Mad proteins binding to certain co-factors which traps them inside the nucleus. These more complex protein structures of the immobile Mad pool might have a smaller diffusion coefficient as compared to that of the unbound molecules of the mobile nuclear Mad pool. As the immobile fraction of  $\text{TkV}^{\text{QD}}$  is much larger than that of the control (see Fig. 4.3), this would lead to a smaller diffusion for  $\text{TkV}^{\text{QD}}$  than for control muscles, consistent with our findings.

# Bibliography

- [1] H. Aberle, A. P. Haghghi, R. D. Fetter, B. D. McCabe, T. R. Magalhaes, and C. S. Goodman. Wishful thinking encodes a BMP type II receptor that regulates synaptic growth in *Drosophila*. *Neuron* **33**, 545 (2002).
- [2] M. Abramovitz and I. A. Stegun. *Pocketbook of mathematical functions*. Verlag Harri Deutsch, Frankfurt am Main (1984).
- [3] M. Affolter and K. Basler. The Decapentaplegic morphogen gradient: from pattern formation to growth regulation. *Nature Reviews Genetics* **8**, 663 (2007).
- [4] B. Alberts, A. Johnson, J. Lewis, M. Raff, K. Roberts, and P. Walter. *Molecular Biology of the Cell*. Garland Publisher, New York (2002, 4th edition).
- [5] U. Alon. *An Introduction to Systems Biology: Design Principles of Biological Circuits*. Chapman & Hall/CRC, Boca Raton (2006).
- [6] D. Angeli, J. E. Ferrell, and E. D. Sontag. Detection of multistability, bifurcations, and hysteresis in a large class of biological positive-feedback systems. *Proceedings of the National Academy of Sciences of the United States of America* **101**, 1822 (2004).
- [7] F. Aurenhammer. Voronoi diagrams - a survey of a fundamental geometric data structure. *Computing Surveys* **23**, 345 (1991).
- [8] D. Axelrod, D. E. Koppel, J. Schlessinger, E. Elson, and W. W. Webb. Mobility measurement by analysis of fluorescence photobleaching recovery kinetics. *Biophysical Journal* **16**, 1055 (1976).
- [9] L. A. Baena-López, A. Baonza, and A. García-Bellido. The orientation of cell divisions determines the shape of *Drosophila* organs. *Current Biology* **15**, 1640 (2005).
- [10] N. Barkai and S. Leibler. Robustness in simple biochemical networks. *Nature* **387**, 913 (1997).
- [11] K. Basler and G. Struhl. Compartment boundaries and the control of *Drosophila* limb pattern by Hedgehog protein. *Nature* **368**, 208 (1994).

- 
- [12] T. Y. Belenkaya, C. Han, D. Yan, R. J. Opoka, M. Khodoun, H. Z. Liu, and X. H. Lin. Drosophila Dpp morphogen movement is independent of dynamin-mediated endocytosis but regulated by the glypican members of heparan sulfate proteoglycans. *Cell* **103**, 981 (2000).
- [13] U. S. Bhalla and R. Iyengar. Emergent properties of networks of biological signaling pathways. *Science* **283**, 5400 (1999).
- [14] T. Bittig, O. Wartlick, A. Kicheva, M. González-Gaitán, and F. Jülicher. Dynamics of anisotropic tissue growth. *New Journal of Physics* (in press, 2008).
- [15] C. Bökel, A. Schwabedissen, E. Entchev, O. Renaud, and M. González-Gaitán. Sara endosomes and the maintenance of Dpp signaling levels across mitosis. *Science* **314**, 1135 (2006).
- [16] R. A. Bolinger and G. Boekhoff-Falk. Distal-less functions in subdividing the Drosophila thoracic limb primordium. *Developmental Dynamics* **232**, 801 (2005).
- [17] T. Bollenbach, K. Kruse, P. Pantazis, M. González-Gaitán, and F. Jülicher. Robust formation of morphogen gradients. *Physical Review Letters* **94**, 018103 (2005).
- [18] T. Bollenbach. *Formation of morphogen gradients*. PhD thesis, Technische Universität Dresden (2005).
- [19] T. Bollenbach, K. Kruse, P. Pantazis, M. González-Gaitán, and F. Jülicher. Morphogen transport in epithelia. *Physical Review E* **75**, 01190 (2007).
- [20] T. Bollenbach, P. Pantazis, A. Kicheva, C. Bökel, M. González-Gaitán, and F. Jülicher. Precision of the Dpp gradient. *Development* **135**, 1137 (2008).
- [21] K. Broadie and M. Bate. Activity-dependent development of the neuromuscular synapse during Drosophila embryogenesis. *Neuron* **11**, 607 (1993).
- [22] I. N. Bronstein and K. A. Semendyayev. *Handbook of mathematics*. Springer-Verlag, Berlin, 1997 (3rd edition).
- [23] H. M. Byrne, J. R. King, D. L. S. McElwain, and L. Preziosi. A two-phase model of solid tumour growth. *Applied Mathematics Letters* **16**, 567 (2003).
- [24] G. Carrero, D. McDonald, E. Crawford, G. de Vries, and M. J. Hendzel. Using FRAP and mathematical modeling to determine the in vivo kinetics of nuclear proteins. *Methods* **29**, 14 (2003).
- [25] A. Charpilienne, M. Nejmeddine, M. Berois, N. Parez, E. Neumann, E. Hewat, G. Trugnan, and J. Cohen. Individual rotavirus-like particles containing 120 molecules of fluorescent protein are visible in living cells. *Journal of Biological Chemistry* **276**, 29361 (2001).

- [26] M. S. Chen, R. A. Obar, C. C. Schroeder, T. W. Austin, C. A. Poodry, S. C. Wadsworth, and R. B. Vallee. Multiple forms of dynamin are encoded by shibire, a *Drosophila* gene involved in endocytosis. *Nature* **351**, 583 (1991).
- [27] S. M. Cohen, in *The Development of Drosophila melanogaster*, Vol. II, edited by M. Bate and A. M. Arias, (Cold Spring Harbor Press, Cold Spring Harbor, New York, 1993).
- [28] F. Crick. Diffusion in embryogenesis. *Nature* **225**, 420 (1970).
- [29] M. C. Cross and P. C. Hohenberg. Pattern-formation outside of equilibrium. *Reviews of Modern Physics* **65**, 851, Pt. 2 (1993).
- [30] S. J. Day and P. A. Lawrence. Measuring dimensions: the regulation of size and shape. *Development* **127**, 2977 (2000).
- [31] D. Drasdo and S. Höhme. A single-cell-based model of tumor growth in vitro: monolayers and spheroids. *Physical Biology* **2**, 133 (2005).
- [32] D. Drasdo. Coarse graining in simulated cell populations. *Advances in Complex Systems* **8**, 319 (2005).
- [33] V. Dudu, T. Bittig, E. Entchev, A. Kicheva, F. Jülicher, and M. González-Gaitán. Postsynaptic Mad signaling at the *Drosophila* neuromuscular junction. *Current Biology* **16**, 625 (2006).
- [34] A. Eldar, R. Dorfman, D. Weiss, H. Ashe, B. Z. Shilo, and N. Barkai. Robustness of the BMP morphogen gradient in *Drosophila* embryonic patterning. *Nature* **419**, 304 (2002).
- [35] A. Eldar, D. Rosin, B. Z. Shilo, and N. Barkai. Self-enhanced ligand degradation underlies robustness of morphogen gradients. *Developmental Cell* **5**, 635 (2003).
- [36] E. V. Entchev, A. Schwabedissen, and M. González-Gaitán. Gradient formation of the TGF-beta homolog Dpp. *Cell* **103**, 981 (2000).
- [37] E. V. Entchev and M. González-Gaitán. Morphogen gradient formation and vesicular trafficking. *Traffic* **3**, 98 (2002).
- [38] R. Farhadifar, J. C. Röper, B. Algouy, S. Eaton, and F. Jülicher. The influence of cell mechanics, cell-cell interactions, and proliferation on epithelial packing. *Current Biology* **17**, 2095 (2007).
- [39] E. L. Ferguson and K. V. Anderson. Decapentaplegic acts as a morphogen to organize dorsal-ventral pattern in the *Drosophila* embryo. *Cell* **71**, 451 (1992).
- [40] G. Forgacs, R. A. Foty, Y. Shafrir, and M. S. Steinberg. Viscoelastic properties of living embryonic tissues: a quantitative study. *Biophysical Journal* **74**, 2227 (1998).

- 
- [41] D. Fristrom and J. W. Fristrom, in *The Development of Drosophila melanogaster*, Vol. II, edited by M. Bate and A. M. Arias, (Cold Spring Harbor Press, Cold Spring Harbor, New York, 1993).
- [42] A. Gierer and H. Meinhardt. Theory of biological pattern formation. *Kybernetik* **12**, 30 (1972).
- [43] J. A. Glazier and F. Graner. Simulation of the differential adhesion driven rearrangement of biological cells. *Physical Review E* **47**, 2128 (1993).
- [44] M. González-Gaitán, M. P. Capdevila, and A. García-Bellido. Cell proliferation patterns in the wing imaginal disc of Drosophila. *Mechanisms of Development* **46**, 183 (1994).
- [45] M. González-Gaitán. Endocytic trafficking during Drosophila development. *Mechanisms of Development* **120**, 1265 (2003).
- [46] T. Gregor, E. F. Wieschaus, A. P. McGregor, W. Bialek, and D. W. Tank. Stability and nuclear dynamics of the bicoid morphogen gradient. *Cell* **130**, 141 (2007).
- [47] T. Gregor, D. W. Tank, E. F. Wieschaus, and W. Bialek. Probing the limits to positional information. *Cell* **130**, 153 (2007).
- [48] J. B. Gurdon and P. Y. Bourillot. Morphogen gradient interpretation. *Nature* **413**, 797 (2001).
- [49] Y. Hatwalne, S. Ramaswamy, M. Rao, and R. A. Simha. Rheology of active-particle suspensions. *Physical Review Letters* **92**, 118101 (2004).
- [50] C. H. Heldin, K. Miyazono, and P. ten Dijke. TGF- $\beta$  signalling from cell membrane to nucleus through SMAD proteins. *Nature* **390**, 465 (1997).
- [51] B. Houchmandzadeh, E. Wieschaus, and S. Leibler. Establishment of developmental precision and proportions in the early Drosophila embryo. *Nature* **415**, 798 (2002).
- [52] L. Hufnagel, A. A. Teleman, H. Rouault, S. M. Cohen, and B. I. Shraiman. On the mechanism of wing size determination in fly development. *Proceedings of the National Academy of Sciences of the United States of America* **104**, 3835 (2007).
- [53] R. Keller. Shaping the vertebrate body plan by polarized embryonic cell movements. *Science* **298**, 1950 (2002).
- [54] M. Kerszberg and L. Wolpert. Mechanisms for positional signalling by morphogen transport: a theoretical study. *Journal of Theoretical Biology* **191**, 103 (1998).
- [55] A. Kicheva, P. Pantazis, T. Bollenbach, Y. Kalaidzidis, T. Bittig, F. Jülicher, and M. González-Gaitán. Kinetics of morphogen gradient formation. *Science* **315**, 521 (2007).



- [56] A. Kicheva. PhD thesis, Geneva University, in preparation.
- [57] J. Kim, K. Johnson, H. J. Chen, S. Carroll, and A. Laughon. Drosophila Mad binds to DNA and directly mediates activation of vestigial by Decapentaplegic. *Nature* **388**, 304 (1997).
- [58] A. J. Koch and H. Meinhardt. Biological pattern formation - from basic mechanisms to complex structures. *Reviews of Modern Physics* **66**, 1481 (1994).
- [59] Y. H. Koh, L. S. Gramates, and V. Budnik. Drosophila larval neuromuscular junction: Molecular components and mechanisms underlying synaptic plasticity. *Microscopy Research and Technique* **49**, 14 (2000).
- [60] K. Kruse, P. Pantazis, T. Bollenbach, F. Jülicher, and M. González-Gaitán. Dpp gradient formation by dynamin-dependent endocytosis: receptor trafficking and the diffusion model. *Development* **131**, 4843 (2004).
- [61] K. Kruse, J. F. Joanny, F. Jülicher, J. Prost, and K. Sekimoto. Generic theory of active polar gels: a paradigm for cytoskeletal dynamics. *European Physical Journal E* **16**, 5 (2005).
- [62] L. D. Landau and E. M. Lifshitz. *Course of Theoretical Physics, Volume 6: Fluid Mechanics*. Pergamon Press, Oxford (1987, 2nd edition).
- [63] A. D. Lander, Q. Nie, and F. Y. M. Wan. Do morphogen gradients arise by diffusion? *Developmental Cell* **2**, 785 (2002).
- [64] A. D. Lander. Morpheus Unbound: Reimagining the Morphogen Gradient. *Cell* **128**, 245 (2007).
- [65] T. Lecuit, W. J. Brook, M. Ng, M. Calleja, H. Sun, and S. M. Cohen. Two distinct mechanisms for long-range patterning by decapentaplegic in the Drosophila wing. *Nature* **381**, 387 (1996).
- [66] T. Lecuit and L. Le Goff. Orchestrating size and shape during morphogenesis. *Nature* **450**, 189 (2007).
- [67] B. D. MacArthur and C. P. Please. Residual stress generation and necrosis formation in multi-cell tumour spheroids. *Journal of Mathematical Biology* **49**, 537 (2004).
- [68] G. Marqués, H. Bao, T. E. Haerry, M. J. Shimell, P. Duchek, B. Zhang, and M. B. O'Connor. The Drosophila BMP type II receptor wishful thinking regulates neuromuscular synapse morphology and function. *Neuron* **33**, 529 (2002).
- [69] J. Massagué. TGF- $\beta$  signal transduction. *Annual Review of Biochemistry* **67**, 753 (1998).

- [70] B. D. McCabe, G. Marqués, A. P. Haghghi, R. D. Fetter, M. L. Crotty, T. E. Haerry, C. S. Goodman, and M. B. O'Connor. The BMP homolog Gbb provides a retrograde signal that regulates synaptic growth at the *Drosophila* neuromuscular junction. *Neuron* **39**, 241 (2003).
- [71] N. McDowell, A. M. Zorn, D. J. Crease, and J. B. Gurdon. Activin has direct long-range signalling activity and can form a concentration gradient by diffusion. *Current Biology* **7**, 671 (1997).
- [72] H. Meinhardt. *Models of biological pattern formation*. Academic Press, London (1982).
- [73] M. Milán, S. Campuzano, and A. García-Bellido. Cell cycling and patterned cell proliferation in the wing primordium of *Drosophila*. *Proceedings of the National Academy of Sciences of the United States of America* **93**, 640 (1996).
- [74] D. Nellen, R. Burke, G. Struhl, and K. Basler. Direct and long-range action of a DPP morphogen gradient. *Cell* **85**, 357 (1996).
- [75] K. J. Painter, P. K. Maini, and H. G. Othmer. Stripe formation in juvenile *Pomacanthus* explained by a generalized Turing mechanism with chemotaxis. *Proceedings of the National Academy of Sciences of the United States of America* **96**, 5549 (1999).
- [76] E. Palsson and H. G. Othmer. A model for individual and collective cell movement in *Dictyostelium discoideum*. *Proceedings of the National Academy of Sciences of the United States of America* **97**, 10448 (2000).
- [77] P. Pantazis. *Role of endocytic trafficking during Dpp gradient formation*. PhD thesis, Technische Universität Dresden (2005).
- [78] F. A. Ramirez-Weber and T. B. Kornberg. Cytonemes: Cellular processes that project to the principal signaling center in *Drosophila* imaginal discs. *Cell* **99**, 599 (1999).
- [79] J. Ranft. Diploma thesis, Technische Universität Dresden, in preparation.
- [80] J. M. Rawson, M. Lee, E. L. Kennedy, and S. B. Selleck. *Drosophila* neuromuscular synapse assembly and function require the TGF-beta type I receptor saxophone and the transcription factor mad. *Journal of Neurobiology* **55**, 134 (2003).
- [81] D. Rogulja and K. D. Irvine. Regulation of cell proliferation by a morphogen gradient. *Cell* **123**, 449 (2005).
- [82] C. M. Schuster, G. W. Davis, R. D. Fetter, and C. S. Goodman. Genetic dissection of structural and functional components of synaptic plasticity. 2. Fasciclin II controls presynaptic structural plasticity. *Neuron* **17**, 655 (1996).

- [83] J. J. Sekelsky, S. J. Newfeld, L. A. Raftery, E. H. Chartoff, and W. M. Gelbart. Genetic characterization and cloning of Mothers against dpp, a gene required for decapentaplegic function in *Drosophila melanogaster*. *Genetics* **139**, 1347 (1995).
- [84] N. Serrano and P. H. O'Farrell. Limb morphogenesis: Connections between patterning and growth. *Current Biology* **7**, R186 (1997).
- [85] B. Z. Shilo. Signaling by the *Drosophila* epidermal growth factor receptor pathway during development. *Experimental Cell Research* **284**, 140 (2003).
- [86] K. Shimizu and J. B. Gurdon. A quantitative analysis of signal transduction from activin receptor to nucleus and its relevance to morphogen gradient interpretation. *Proceedings of the National Academy of Sciences of the United States of America* **96**, 6791 (1999).
- [87] B. I. Shraiman. Mechanical feedback as a possible regulator of tissue growth. *Proceedings of the National Academy of Sciences of the United States of America* **102**, 3318 (2005).
- [88] J. M. W. Slack. *Essential Developmental Biology*. Blackwell, Oxford (2006).
- [89] D. M. Soumpasis. Theoretical analysis of fluorescence photobleaching recovery experiments. *Biophysical Journal* **41**, 95 (1983).
- [90] F. A. Spencer, F. M. Hoffmann, and W. M. Gelbart. Decapentaplegic - a gene-complex affecting morphogenesis in *Drosophila-melanogaster*. *Cell* **28**, 451 (1982).
- [91] T. Tabata and Y. Takei. Morphogens, their identification and regulation. *Development* **131**, 703 (2004).
- [92] A. A. Teleman and S. M. Cohen. Dpp Gradient Formation in the *Drosophila* Wing Imaginal Disc. *Cell* **103**, 971 (2000).
- [93] M. Théry, A. Jiménez-Dalmaroni, V. Racine, M. Bornens, and F. Jülicher. Experimental and theoretical study of mitotic spindle orientation. *Nature* **447**, 493 (2007).
- [94] A. M. Turing. The chemical basis of morphogenesis. *Philosophical Transactions of the Royal Society of London Series B - Biological Sciences* **237**, 37 (1952).
- [95] J. M. G. Vilar, R. Jansen, and C. Sander. Signal Processing in the TGF- $\beta$  Superfamily Ligand-Receptor Network. *PLoS Computational Biology* **2**, 36 (2006).
- [96] G. Weng, U. S. Bhalla, and R. Iyengar. Complexity in biological signaling systems. *Science* **284**, 92 (1999).
- [97] V. Wiersdorff, T. Lecuit, S. M. Cohen, and M. Mlodzik. Mad acts downstream of Dpp receptors, revealing a differential requirement for dpp signaling in initiation and propagation of morphogenesis in the *Drosophila* eye. *Development* **122**, 2153 (1996).

- [98] L. Wolpert. Positional information and spatial pattern of cellular differentiation. *Journal of Theoretical Biology* **25**, 1 (1969).
- [99] L. Wolpert, R. Beddington, T. Jessell, P. Lawrence, E. Meyerowitz, and J. Smith. *Principles of Development*. Oxford University Press, Oxford (2002, 2nd edition).
- [100] M. Zecca, K. Basler, and G. Struhl. Sequential organizing activities of engrailed, hedgehog and decapentaplegic in the *Drosophila* wing. *Development* **121**, 2265 (1995).
- [101] M. Zecca, K. Basler, and G. Struhl. Direct and long-range action of a wingless morphogen gradient. *Cell* **87**, 833 (1996).

# Versicherung

Hiermit versichere ich, dass ich die vorliegende Arbeit ohne unzulässige Hilfe Dritter und ohne Benutzung anderer als der angegebenen Hilfsmittel angefertigt habe; die aus fremden Quellen direkt oder indirekt übernommenen Gedanken sind als solche kenntlich gemacht. Die Arbeit wurde bisher weder im Inland noch im Ausland in gleicher oder ähnlicher Form einer anderen Prüfungsbehörde vorgelegt. Die vorliegende Arbeit wurde vom 15.3.2005 bis 13.5.2008 unter der Aufsicht von Prof. Dr. Frank Jülicher am Max-Planck-Institut für Physik komplexer Systeme in Dresden durchgeführt.

Ich versichere, dass ich bisher keine erfolglosen Promotionsverfahren unternommen habe. Ich erkenne die Promotionsordnung der Fakultät Mathematik und Naturwissenschaften der Technischen Universität Dresden an.

Dresden, den 13.5.2008, Thomas Bittig